universität wien

MASTERARBEIT / MASTER'S THESIS

Titel der Masterarbeit / Title of the Master's Thesis

„A low energy proton source for ASACUSA's matter studies “

verfasst von / submitted by

Alina Weiser, BSc

angestrebter akademischer Grad / in partial fulfilment of the requirements for the degree of

Master of Science (MSc)

Wien, 2020 / Vienna, 2020

Studienkennzahl lt. Studienblatt / degree programme code as it appears on the student record sheet:	UA 066 876
Studienrichtung lt. Studienblatt / degree programme as it appears on the student record sheet:	Masterstudium Physik
Betreut von / Supervisor:	Hon.-Prof. Dipl.-Phys. Dr. Eberhard Widmann

Abstract

The ASACUSA experiment aims to measure the ground-state hyperfine structure of antihydrogen in order to test CPT and possibly discover physics beyond the Standard Model. However, due to the currently ongoing Long Shutdown 2 at CERN no slow anti-protons, necessary for antihydrogen formation, can be produced. During this time the 'mixing scheme' used to produce antihydrogen by mixing e^+ and $\overline{p}$, can be improved by exchanging antiparticles with the corresponding particles in order to form hydrogen. Subsequently, a low energy proton source has been designed and developed. It consists of three modules, an electron gun, a gas cell–penning trap and an extraction module. Protons are produced inside the gas cell trap by electron impact ionisation of H_2-gas. The protons can then be radially confined by a magnetic field produced by rod magnets and axially confined by a quadrupolar electric field generated with electrodes. The extraction module is used to focus and steer the proton beam into the hydrogen mixing trap. The source was tested and characterised with a MCP-delay-line detector, which will later be used for both Rydberg-hydrogen and proton detection. The characterisation measurements showed that it produces a beam of H, H_2 and H_3 ions, which can be moved and focussed by the extraction module. As expected from the partial ionisation cross-sections of H_2-gas, without the application of cooling pulses, the number of generated protons is low in comparison to the number of H_2^+ and H_3^+ produced by the source. However, it was also found that, by applying rotating wall pulses with a frequency of 0.47 MHz on the gas cell trap, the number of protons can be increased while both H_2 and H_3 ions are driven out of the trap. It is estimated that in this mode, the source can generate approximately two million protons and half a million H_2^+ and H_3^+ each, per second.

Zusammenfassung

Die ASACUSA Kollaboration hat das Ziel die Hyperfeinstruktur von Antiwasserstoff im Grundzustand zu messen. Diese Messung kann das CPT-Theorem testen und möglicherweise zu einer Entdeckung von Physik jenseits des Standardmodells führen. Aber nachdem sich CERN derzeit im ‚Long Shutdown 2' befindet, können keine langsamen Antiprotonen hergestellt werden. Während dieser Zeit kann das Antiwasserstoffproduktionsschema verbessert werden indem die Antiteilchen mit ihren Materiepartnern ausgetauscht werden. Aus diesem Grund wurde eine Protonenquelle entwickelt. Dieses Gerät besteht aus drei verschiedenen Modulen, der Elektronenkanone, der Gaszelle und dem Extraktionsmodul. Die Protonen werden in der Gaszelle durch Elektronstoßionisation in H_2-Gas produziert. Nachdem die Gaszelle auch eine Penningfalle ist, werden die Protonen dann durch die elekrischen und magnetischen Felder gefangen. Das Extraktionsmodul kann den extrahierten Protonenstrahl fokussieren und in die gewünschte Richtung steuern. Mit der Quelle können sowohl kontinuierliche als auch gepulste Strahlen von Protonen herstellt werden. Wie von dem Ionisationsquerschnitt von H_2 erwartet, ist die Anzahl der produzierten Protonen klein im Gegenzug zu der Zahl der generierten H_2 und H_3-Ionen. Wenn aber ‚rotating wall' Pulse mit einer Frequenz von 0.47 MHz an die Gaszelle angelegt werden, kann die Nummer der Protonen erhöht werden. Zur gleichen Zeit werden aber H_2^+ und H_3^+ aus der Quelle verdrängt. Es wird geschätzt, dass die Quelle in diesem Modus zwei Millionen Protonen und jeweils eine halbe Million H_2^+ und H_3^+ pro Sekunde produzieren kann.

Acknowledgements

First, I want to express my deepest gratitude to Prof. Eberhard Widmann, for giving me the opportunity to be a part of an international collaboration and for all the support and supervision he provided to me during both my internship and the time spent working on my thesis.
I also want to express my appreciation to Dr. Daniel Murtagh and Dr. Martin Simon, two people who not only provided me with guidance in the Lab but also throughout my entire time at SMI. Thank you, for your patience, advice, encouragement and for all the time you invested in me!
I am also really grateful, for all my amazing colleges at SMI. I particularly want to thank Ing. Doris Pristauz-Telsnigg, Leopold Stohwasser and Mark Pruckner for their help in the design and construction process of the source. Thank you to Prof. Johann Zmeskal for always providing me with great advice in Lab. Furthermore, I want to express my appreciation towards Dr. Eric Hunter for helping me with everything from electronics to LabView.
Moreover, I want thank Andi, Amit, Babsi, Constanze, Marlene, Sigrid and Vici. Without you, my time at SMI would not have been this great and memorable!

I would also like to thank all my great friends at the University of Vienna, for the many laughs we shared and for always being able to rely on you.
Lastly and most importantly, I want to thank my family. Thank you, for always being there for me, for encouraging and believing in me, I would not be where I am without you!

Contents

1 Preface **1**

2 Introduction **4**

2.1 Electron Impact Ionisation 4

2.2 The Penning trap 7

2.2.1 The ideal Penning trap 7

2.2.2 Cylindrical Penning traps 12

2.3 Ion Detection - Microchannel Plate Detectors 14

2.3.1 Microchannel plates 14

2.3.2 Anodes 17

3 Experimental Setup **19**

3.1 Proton Source 19

3.1.1 Electron Gun Module 20

3.1.2 Gas Cell Module 23

3.1.3 Extraction Module 26

3.1.4 Assembly 31

3.2 MCP Delay Line Detector 33

3.3 Setup for characterisation measurements 37

4 Results **40**

4.1 Continuous Mode Measurements 40

4.2 Pulsed Mode Measurements 47

4.3 Trapping Mode Measurements 49

4.3.1 Sideband cooling 51

4.3.2 Rotating wall 55

5 Conclusion and Outlook **65**

A Acronyms **69**

B Electronic Connection Diagrams **71**

B.1 Proton Source 71

B.2 Detector 73

C Circuit Diagrams **76**

Chapter 1

Preface

The existence of antimatter was first predicted after Paul Dirac developed his quantum theory of an electron [1] in 1928. His famous equation resulted in two solutions, one with positive energy and the other one with negative energy. Initially he believed that the negative energy solution would give rise to a proton. However, upon finding it's mass should be equal to that of an electron, he predicted an entirely new particle, the positron. As mentioned, it has the same mass as an electron but is instead positively charged [2]. After this first antimatter particle was detected in 1932 by Carl D. Anderson [2], Dirac was awarded the Nobel prize in physics in 1933 and in his Nobel lecture he even said [3]:

> *"If we accept the view of complete symmetry between positive and negative electric charge so far as concerns the fundamental laws of Nature, we must regard it rather as an accident that the Earth (and presumably the whole solar system), contains a preponderance of negative electrons and positive protons. It is quite possible that for some of the stars it is the other way about, these stars being built up mainly of positrons and negative protons. In fact, there may be half the stars of each kind." [4]*

However, the 'antimatter stars' Dirac mentioned have not yet been observed [5, 6] and to this day the asymmetry of matter and antimatter in the universe still remains an unsolved problem in particle physics [7].
Today the standard model of particle physics is responsible for describing nature's fundamental forces, it also classifies the elementary particles and explains their interactions. According to it's fundamental CPT-theorem, antiparticles have the same masses and lifetimes (for unstable particles) as well as equal but opposite charges as their matter counterparts.
By measuring and comparing the properties of matter and antimatter it is possible to search for a violation of CPT symmetry, which in turn would reveal physics beyond the standard model [8].
One theory, the Standard Model Extension (SME) [9] allows for CPT symmetry breaking and can be tested by comparing the hyperfine structures of hydrogen and antihydro-

gen [10]. As the hyperfine structure of hydrogen has already been measured precisely [11], the Atomic Spectroscopy And Collisions Using Slow Antiprotons (ASACUSA) Cusp experiment aims to measure this splitting using a beam of antihydrogen [8].
$\overline{\mathrm{H}}$ can be produced by combining an anti-proton and a positron. In the ASACUSA experiment, the positrons are produced with a ^{22}Na source, accumulated and then captured in a double Cusp trap. The $\overline{\mathrm{p}}$ are supplied by the Antiproton Decelerator (AD), trapped in the MUSASHI-trap and then also injected into the Cusp trap, where they are mixed with the positron plasma. The mixing process is described in detail in [12]. Briefly, antihydrogen is mainly produced through three body recombination:

$$e^+ + e^+ + \overline{\mathrm{p}} \rightarrow e^+ + \overline{\mathrm{H}} \tag{1.1}$$

The production of an $\overline{\mathrm{H}}$ beam using this setup was successful for the first time in 2014 [13]. Once the antihydrogen is focussed and polarised by the cusped field, it leaves the trap, goes through a hyperfine-spectrometer line and is ultimately detected by a $\overline{\mathrm{H}}$-detector.
Currently however, the entire European Organisation for Nuclear Research (CERN) accelerator complex is in Long Shutdown 2 (LS2), a period in which the components of the accelerators and experiments are updated and improved. Due to this, no antiprotons are available and subsequently antihydrogen cannot be synthesised.
However, during this time, it is also possible to upgrade and test ASACUSA's apparatus. One part of these improvements comes in the form of characterizing the mixing regimes in the Cusp trap using matter [14].
While the electrons can be created using an existing electron gun, a proton source had to be developed. This thesis will describe the working principle, construction and characterisation of this device.
A schematic setup for the matter experiments can be found in figure 1.1. Once the protons and electrons are mixed in the Cusp-trap they form exited hydrogen and go through an external field ionizer (EFI) and are detected as protons by a position sensitive MCP- delay line detector.
This detector will also be described in this thesis as it was used to characterise the proton source.

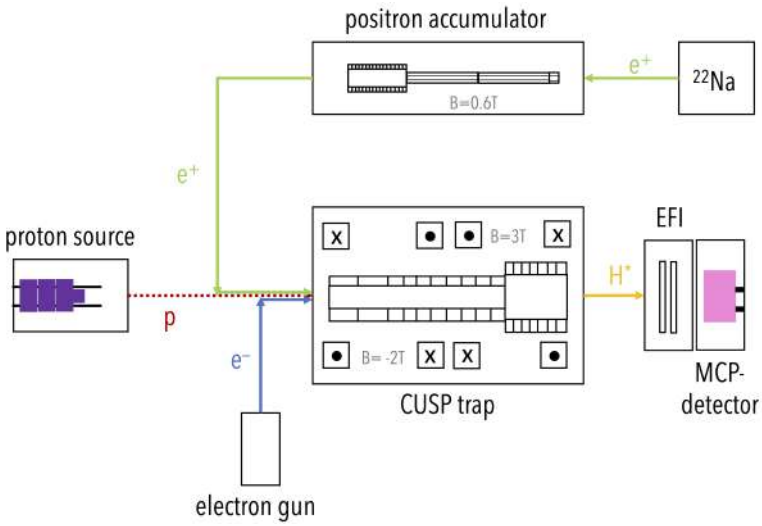

Figure 1.1: Schematic view of ASACUSA's setup for matter mixing experiments

Chapter 2

Introduction

This chapter will describe three important concepts necessary for the functionality of the proton source and it's characterisation - ion production, storage and detection.

2.1 Electron Impact Ionisation

Protons can be produced in various ways, one of which is colliding electrons with molecular hydrogen H_2 and subsequently ionizing it [15]. However, ionisation is just one of the possible outcomes following an atomic collision process. Other processes include elastic scattering and excitation [16].

$$\text{exitation: } e^- + H_2 \rightarrow e^- + H_2^* \rightarrow e^- + H_2 + h\nu \tag{2.1}$$

$$\text{elastic scattering: } e^- + H_2 \rightarrow e^- + H_2 \tag{2.2}$$

A simple scattering experiment can be described as follows [17, 18]: A mono-energetic beam of particles with a flux F, where F is the number of particles per unit time which cross a unit area placed perpendicular to the beam-direction, is scattered by a target. A detector measures the scattered particles N over an area $d\Omega$ in direction (θ, φ) from this target. A schematic diagram of such an experiment can be seen in figure 2.1.

The collision processes of this setup can now be characterized by the differential cross-section

$$\frac{d\sigma}{d\Omega} = \frac{N}{F} \tag{2.3}$$

The total cross-section σ_{tot} is obtained by the integration of $\frac{d\sigma}{d\Omega}$ over all solid angles:

$$\sigma_{tot} = \int_0^{2\pi} d\varphi \int_0^{\pi} d\theta \sin\theta \frac{d\sigma}{d\Omega} \tag{2.4}$$

Partial cross-sections can describe different types of a scattering event such as, e.g. elastic scattering $\sigma_{elastic}$, inelastic scattering $\sigma_{inelastic}$, or ionisation $\sigma_{ionisation}$. A complete theoretical description of ionisation processes is however still an unsolved problem in

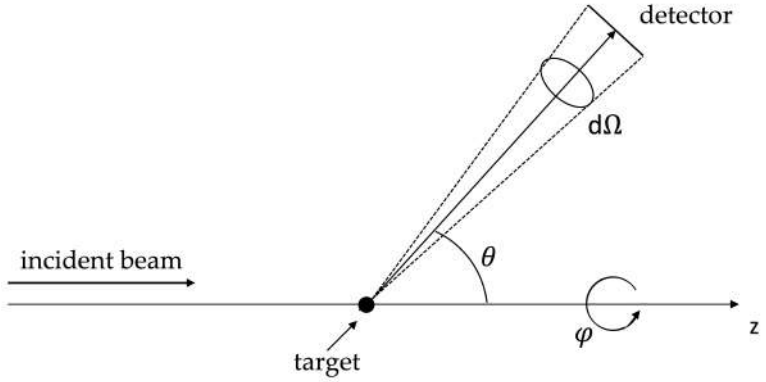

Figure 2.1: Schematic diagram of a scattering experiment

atomic physics. This is due to the fact that the long range coulomb force enables the interaction between the two electrons (incoming and emitted) and residual ion even after the collision process [19].

As H_2-gas is a molecular gas, two forms of ionisation are possible [16]. Firstly the electron impact can result in a single ionisation where the molecule looses one electron. In this process the molecule does not fall apart and therefore a H_2-ion rather than a proton is created.

$$\text{single ionisation: } e^- + H_2 \rightarrow H_2^+ + 2e^- \tag{2.5}$$

However, in a process called dissociative ionisation, the impact can also break the molecule apart. This can be the outcome of a single or multiple ionisation processes, resulting in different types of fragments.

$$\text{dissociative ionisation: } e^- + H_2 \rightarrow H + H^+ + 2e^- \tag{2.6}$$

In hydrogen gas this can lead to the production of a proton as shown in the reaction above. An alternative branch of dissociative ionisation for generating protons would be the following:

$$\text{dissociative ionisation: } e^- + H_2 \rightarrow H^+ + H^+ + 3e^- \tag{2.7}$$

In order to induce an electronic transition which leads to a dissociative process, a minimum energy of

$$E_{min} = E_A + E_B + D_{AB} + W_{min} \tag{2.8}$$

is necessary [16]. Here E_A and E_B are the excitation energies of the atoms A and B in the molecule AB. W_{min} is their minimum kinetic energy and D_{AB} is the molecule's dissociation energy.

H_2 has a dissociation energy of $\backsim 4.46\,\text{eV}$ [20] and the ionisation energy of hydrogen is $\backsim 13.6\,\text{eV}$. Assuming that W_{min} is zero, this results in a minimum electron energy of $\approx 18.06\,\text{eV}$ in order to create a proton.

The absolute partial cross-sections in figure 2.2 were obtained from the measurements of Straub *et al.* [21]. The H^+ cross-sections were multiplied by 5, so that the curve is more visible in the plot. Measurements show that the highest cross-section for proton production in electron impact ionisation of H_2 (channel 2.6) is $8.03 \times 10^{-18}\,\mathrm{cm}^2$ for an electron energy of 95 eV. At the same electron energy, H_2^+'s absolute partial production cross-section is a magnitude higher at a value of $8.81 \times 10^{-17}\,\mathrm{cm}^2$.
The cross-section for proton production through channel 2.7 is approximately two orders of magnitude lower than that of channel 2.6 [22].

The kinetic energy spectrum of protons generated by the reaction channel 2.6 was

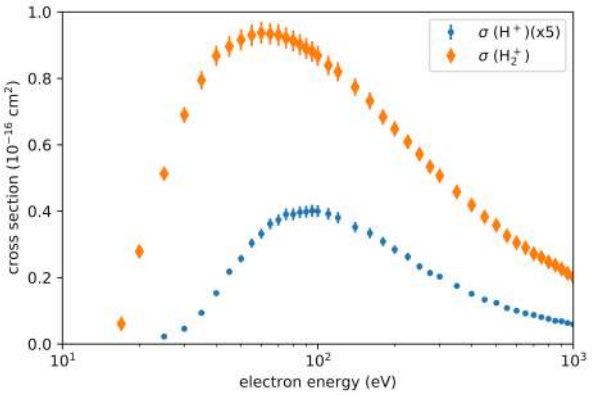

Figure 2.2: Absolute partial cross sections for electron-impact ionisation of H_2 obtained from Straub et al. [21].

measured by Kahkoo and Srivastava in 1985 [23]. Overall the kinetic energy of the protons increases with higher electron impact energies. The measured spectrum contains a peak at zero energy followed by a broad energy distribution. At 40 eV electron impact energy this distribution includes a second peak at approximately 4 eV. When the energy of the electrons is increased this peak shifts towards ≈ 5 eV.
Figure 2.3 shows this relative proton kinetic energy distribution at 50 eV electron impact energy. Another process which should be noted, is that after H_2^+ is created through electron impact, it can collide with H_2 and form H_3^+. The process is described by the following formula [24]:

$$H_2^+ + H_2 \rightarrow H_3^+ + H \tag{2.9}$$

Generally, collision processes of H^+, H_2^+, H_3^+ with H_2 can result in an array of reactions and therefore many different products including electrons, light and neutral H and H_2. Several of these reactions and their cross sections can be found in e.g. [25].
As the proton source will use electron impact ionisation to produce it's protons, reaction channels 2.6, 2.5 and 2.9 are important for it's operation. Due to it's aforementioned small cross-section, channel 2.7 does not play a significant role in the production of protons in the source.

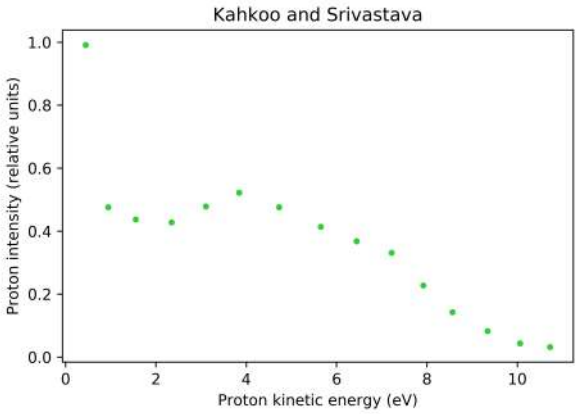

Figure 2.3: Kinetic energy distribution of protons produced by electron impact ionisation of H_2-gas. The data is obtained from Kahkoo and Srivastava [23]

2.2 The Penning trap

Charged particles can be trapped using several different devices, the most common ones being Penning and Paul traps as well as storage rings [26].
Generally, in order to confine ions, a three dimensional potential energy well is required. Earnshaw's theorem illustrates however, that this is impossible to produce using just static electric fields.
A quadrupolar electric field is given by

$$\Phi(x, y, z) = Ax^2 + By^2 + Bz^2 \tag{2.10}$$

where A, B and C are positive. The potential must fulfil Laplace's equation $\Delta\Phi = 0$, and subsequently the coefficients must satisfy

$$A + B + C = 0 \tag{2.11}$$

This relation is not fulfilled unless at least one of the coefficients is negative. Static electric fields therefore create a saddle potential rather than a well and consequently charged particles cannot be trapped in all directions.
This problem can be circumvented by either superimposing a magnetic field (Penning trap) or using an oscillating electric field (Paul trap) [26]. These two particle traps were developed in late 1950's and early 1960's, earning their creators, Wolfgang Paul and Hans Dehmelt, the Nobel Prize in Physics in 1989 [26, 27].

2.2.1 The ideal Penning trap

The ideal Penning trap consists of three hyperboloid electrodes (2 end-caps and a ring) which create a quadrupole potential and can be seen in figure 2.4. When a positive potential U is put on to the two end-caps with regard to the ring, the overall electric

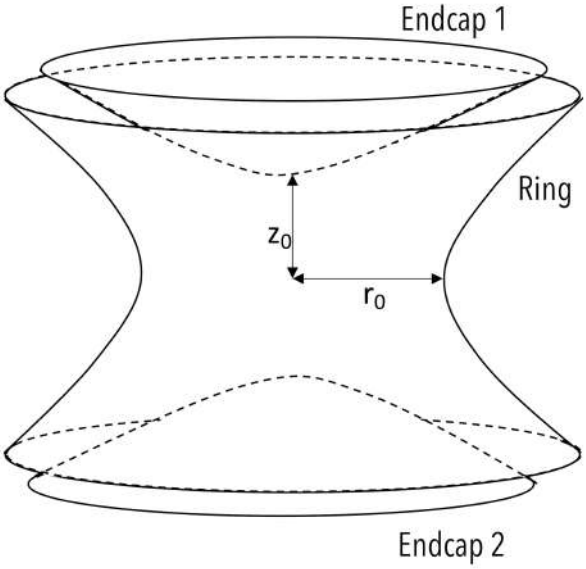

Figure 2.4: Electrodes of an ideal penning trap

potential which is created has the following shape [28]:

$$\Phi(r,z) = \frac{U(2z^2 - r^2)}{r_0^2 + 2z_0^2} = \frac{U}{d^2}(2z^2 - r^2) \tag{2.12}$$

where $d^2 = \frac{1}{2}(\frac{r_0^2}{2} + z_0^2)$ is a parameter given by the trap dimensions.

This quadratic electric potential traps a particle axially, however due to the fact that the potential in the radial plane has a maximum at x=y=0 and depends quadratically on x and y, it's radial motion is unstable. Radial confinement in a Penning trap is therefore generated by superimposing a strong homogeneous magnetic field $\vec{B} = (0, 0, B_z)$ along the z axis.

The motion of a charged particle in the trap is governed by the Lorentz force $\vec{F}$.

$$\vec{F} = e(\vec{E} + \vec{v} \times \vec{B}) \leftrightarrow m\ddot{\vec{r}} = q(\vec{E} + \vec{v} \times \vec{B}) \tag{2.13}$$

$\vec{E} = -\nabla\Phi(r,z)$ is the electric field, m the mass of the particle, q the charge and $\vec{v} = (v_x, v_y, v_z)$ it's velocity.
This results in the following equations of motion for a single particle:

$$\ddot{x} + \omega_c\dot{y} - \left(\frac{\omega_z^2}{2}\right)x = 0 \tag{2.14}$$

$$\ddot{y} - \omega_c\dot{x} - \left(\frac{\omega_z^2}{2}\right)y = 0 \tag{2.15}$$

$$\ddot{z} + \omega_z^2 z = 0 \tag{2.16}$$

One can see, that the motion of a particle in axial direction is completely independent from the motion in the x,y plane. Specifically it is a harmonic oscillation between the endcaps with an axial frequency ω_z.

$$\omega_z = \sqrt{\frac{4qU}{md^2}} \tag{2.17}$$

However in the radial (x,y) plane, the Lorentz force on the trapped particle is a combination between both the forces of the electric and the magnetic field. The latter is dominant and defined by the cyclotron frequency ω_c.

$$\omega_c = \frac{qB_z}{m} \tag{2.18}$$

The motion in this plane can be reduced to a single radial equation of motion by introducing the complex variable u = x +iy [29].

$$\ddot{u} + i\omega_c\dot{u} - \frac{\omega_z^2 u}{2} = 0 \tag{2.19}$$

This differential equation can be solved using

$$u(t) = re^{-i\omega t} \tag{2.20}$$

and results in two solutions with the frequencies

$$\omega_\pm = \frac{1}{2}\left(\omega_c \pm \sqrt{\omega_c^2 - 2\omega_z^2}\right) \tag{2.21}$$

ω_+ is the called the modified cyclotron and w_- the the magnetron frequency. Using the radii r_+ and r_- of these motions, the general solution is therefore the following:

$$u(t) = r_+e^{-i(\omega_+ t+\phi_+)} + r_-e^{-i(\omega_- t+\phi_-)} \tag{2.22}$$

ϕ_+, ϕ_- are additional phases which can be added to both of the motions.
Each of the individual motions (axial, modified cyclotron and magnetron) as well as the total trajectory of a charged particle can be seen schematically in figure 2.5
The modified cyclotron motion is an orbit around the magnetic field lines whereas the magnetron motion is a slow orbit around the trap centre. The sum of their eigenfrequencies gives the real cyclotron frequency.

$$\omega_c = \omega_+ + \omega_- = \frac{qB_z}{m} \tag{2.23}$$

Two further relations between the frequencies exist:

$$2\omega_+\omega_- = \omega_z^2, \tag{2.24}$$

$$\omega_z^2 + \omega_+^2 + \omega_-^2 = \omega_c^2. \tag{2.25}$$

In a real trap the electrostatic field mentioned above is not perfect. This can be caused by e.g faults in the shape of the trap electrodes. Additionally, the electrodes can be misaligned with respect to the magnetic field or other electrodes. These and other imperfections and their influence on the frequencies of the particles in the trap are mentioned in [29]. However it has to be noted the according to the invariance theorem by Brown and Gabrielse [30], these flaws do not play a role for equation 2.25 which holds even for real penning traps with its field imperfections.

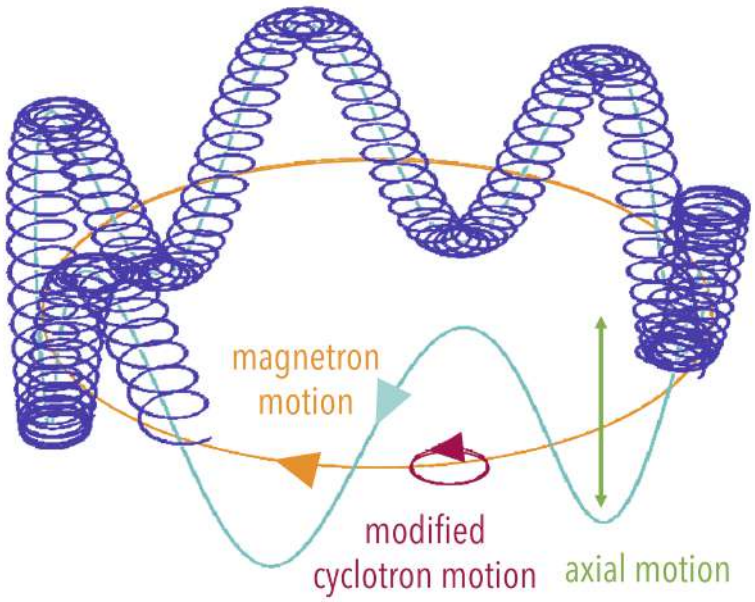

Figure 2.5: Schematic diagram of the trajectory of a charged particle in a penning trap (dark blue). It is a superposition, of the axial motion with frequency ω_z shown in green, the modified cyclotron motion with frequency ω_+ shown in red and the magnetron motion with frequency ω_- shown in orange. The turquoise trajectory is the superposition of axial and magnetron motion

Space Charge

The equations above were derived for a single trapped particle, however when a trap contains a high density of ions, this cloud of particles behaves like a non-neutral plasma. The ions result in an increase in space charge which in turn modifies the potentials generated by the trap. Such a cloud of ions is defined by its uniform density n and ellipsoidal shape. It generates an electric field $E \propto r$ which in turn through $\vec{E} \times \vec{B}$ causes a rotation of the cloud around the z axis with a frequency ω_r [31]. The number

density n of the ion cloud can be calculated using:

$$n = \frac{2\epsilon_0 m\omega_r(\omega_c - \omega_r)}{q^2} \tag{2.26}$$

where ϵ_0 is the dielectric constant, m the mass of a single ion and q the elementary charge. The plasma achieves it's maximum density $n = \frac{\epsilon_0 B^2}{2m}$ when $\omega_r = \frac{\omega_c}{2}$ [28]. This is referred to as Brillouin flow.
Space charge additionally alters both the reduced cyclotron and magnetron frequency [31].

$$\omega'_{\pm} = \frac{\omega_c}{2} \pm \sqrt{\left(\frac{\omega_c}{2}\right)^2 - \frac{\omega_z^2}{2} - \frac{\omega_p^2}{3}} \tag{2.27}$$

with

$$\omega_p^2 = \frac{\rho q}{m\epsilon_0} \tag{2.28}$$

where ρ is the ion cloud density.

Cooling

The energy of trapped particles can be reduced using various different techniques, several of which are described in [26].

Ions can be cooled by adding a low pressure buffer gas into the trap. In this cooling method, called buffer gas cooling, the ions transfer their energy to the gas molecule in collisions. Generally the effect of this can be described by a viscous drag force [32]:

$$\vec{F} = -m\kappa\vec{v} \tag{2.29}$$

where κ is a dampening factor which depends on the velocity of the particles in the trap. This dampening creates a new term in the equations of motion of the trapped particles. While the amplitude for both the axial and reduced cyclotron motion is damped, the radius magnetron motion becomes unstable and increases.
In order to keep the ions in the trap, it is therefore necessary to stabilize the magnetron motion, which can be done by coupling it to either the axial or reduced cyclotron motion. For this, radio-frequency pulses with a frequency of $\omega_{cool} = \omega_c = \omega_+ + \omega_-$ are applied to the trap electrodes [32].
To successfully couple the magnetron motion to ω_+ or ω_z, the amplitude V_{RF} of the radiofrequency (RF)-field has to be large enough:

$$\frac{V_{RF}}{2a^2} \geq B \cdot \kappa \tag{2.30}$$

In the case of a cylindrical penning trap, described in chapter 2.2.2, a can be approximated as the inner diameter of the segmented ring electrode [32].

One advantage of this technique, called sideband cooling, is the fact that the cyclotron frequency depends on the mass of a particle which in turn allows for mass selective cooling of ions. The lowest possible plasma temperature is achieved once the ions are in thermal equilibrium with the buffer gas.

A different stabilisation approach using a rotating wall field, is useful in combination with buffer gas cooling but also for plasmas with high ion densities. If the ion density in the trap is high, then the space charge mentioned above, starts to become apparent. Specifically the rotation of the cloud leads to an increase of its size. This can be suppressed by applying a rotating electric field which moves the ions around axis of the trap [32]. Even though this technique was initially only used for plasmas it has been shown that it also works in the single particle regime [34]. By changing the phases of the applied RF potentials on electrodes, the electric field can either rotate in the same direction as the $\vec{E} \times \vec{B}$ rotation, or in the opposite direction. In the first case the ions in the trap will be compressed, in the latter the electric field causes the particle cloud to expand [34]. The compression rate Γ of particles in an ideal penning trap using buffer gas and rotating wall cooling was found analytically in [35]:

$$\Gamma = \frac{m\kappa}{4}\left(1 - \sqrt{\frac{(\omega_r - \omega_z - \omega_-)^2}{\delta^2 + (\omega_r - \omega_z - \omega_-)^2}}\right) \tag{2.31}$$

where δ is dependent on the rotating wall's amplitude u_{rot}:

$$\delta = \frac{u_{rot}}{\sqrt{(\omega_+ + \omega_-)\omega_z}} \tag{2.32}$$

2.2.2 Cylindrical Penning traps

As traps with hyperbolic endcap and ring electrodes are difficult to construct and the structure makes access to the trapped ions hard, different simplifications of the design can be of benefit. Additionally it has been shown that the ratio between $2z_0$ (minimum distance between endcap electrodes) and $2r_0$ (minimum distance between ring electrodes) is more important than the hyperbolic shape itself [30].
Even though a hyperbolic penning trap are more ideal and can produce a quadrupole potential over a larger volume, cylindrical traps are especially useful for smaller trapping volumes as these electrodes can be manufactured faster and with better accuracy. These traps consist of one or more cylindrical ring electrodes and flat endcaps. The additional ring electrodes can be used to apply a compensation potential to improve the potential in the centre of the trap. Anharmonicities can also be reduced mechanically by optimizing the aforementioned ratio between z_0 and r_0.
The following derivation by Gabrielse and Mackintosh [36] uses that the particles are usually confined in the central region $r \ll d$ of the trap and therefore the potential V does not have to be known in the entire volume. For this area, the potential is expanded

using even order Legendre polynominals $P_k(\cos\theta)$ [36].

$$V = \frac{1}{2}V_0 \sum_{k_{even}=0}^{\infty} D_k \left(\frac{r}{d}\right)^k P_k(\cos\theta) \tag{2.33}$$

Here d is again the parameter given by the traps dimensions. As particles are trapped near the centre, such that $r \ll d$, the lower order coefficients are the most relevant. D_0 can not be physically observed whereas D_2 is given by the axial frequency of the trapped particle by:

$$\omega_z^2 = \frac{qV_0}{md^2} D_2 \tag{2.34}$$

Any higher order coefficients are a measure for trap anharmonicities, specifically D_4. These coefficients should therefore be reduced as much as possible to achieve a sufficient quadrupole potential. In an ideal quadrupole potential all expansion coefficients D_k would go to 0, with the exception of D_2 [36].
Figure 2.6 shows the simplest form of cylindrical penning traps, using two flat endcap electrodes shown in blue and one cylindrical ring electrode which is shown here in green. For this kind of Penning trap the solution for the potential inside the trap is

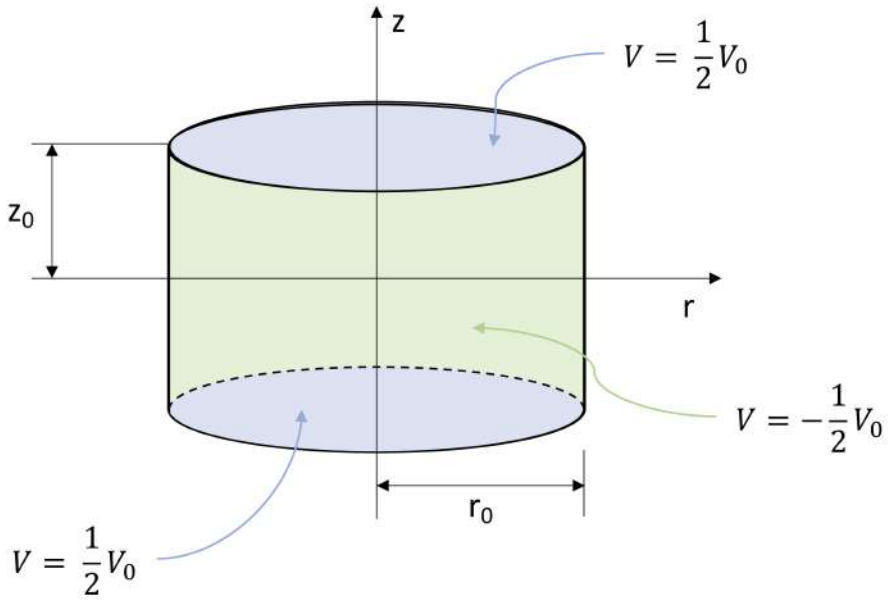

Figure 2.6: Penning trap with a cylindrical ring electrode (green) with potential $-\frac{V_0}{2}$ and radius $r = r_0$ and two flat endcap electrodes (blue) positioned at $z = \pm z_0$ with a potential $\frac{V_0}{2}$.

given by [36]:

$$V = V_0 \left[\frac{1}{2} + \sum_{n=0}^{\infty} A_n J_0(ik_n r)\cos(k_n z)\right]. \tag{2.35}$$

J_0 is the zero-order Bessel function

$$J_0(ix) = \sum_{j=0}^{\infty} \frac{1}{(j!)^2} \left(\frac{x}{2}\right)^{2j} \tag{2.36}$$

and k_n are constants

$$k_n = \frac{(n + \frac{1}{2})\pi}{z_0} \tag{2.37}$$

Coefficients D_k can be found by the analysis of expansions 2.33 and 2.35 along the z axis:

$$D_k = \frac{(-1)^{k/2}}{k!} \frac{\pi^{k-1}}{2^{k-3}} \left(\frac{d}{z_0}\right)^k \sum_{n=0}^{\infty} \frac{(-1)^{n+1}(2n+1)^{k-1}}{J_0(ik_n r_0)} \tag{2.38}$$

The D_k's are only dependent on r_0/z_0 and D_4 completely vanishes for [36]

$$r_0 \approx 1.203 z_0 \tag{2.39}$$

Anharmonicities can therefore reduced mechanically to a minimum if the trap is adjusted such r_0 and z_0 fulfil this ratio [36].
This mechanically compensated form of a penning trap is used in the proton source in combination with buffer gas and sideband cooling to directly trap the protons produced by electron impact ionisation.

2.3 Ion Detection - Microchannel Plate Detectors

Microchannel plate (MCP)-detectors can be used to detect and image several different types of particles and antiparticles, such as electrons, ions, photons [37–39], exited neutral particles [40], positrons [41] and antiprotons [42].
As such a detector was chosen to characterize the proton source and will also be used to detect the exited hydrogen produced in the Cusp trap, the detection principle and characteristics will be described in the following sections.
The main components of a MCP-detector, the microchannel plates, referred to as MCPs, and the anode will be described separately below.

2.3.1 Microchannel plates

A MCP can be thought of as a two dimensional array of electron-multiplier tubes, which for decades have been successfully used in experiments.
An electron multiplier is used as both a particle detector and signal-amplifier. When an incoming electron hits a dynode it ejects secondary electrons. These electrons are then accelerated towards several other dynodes where additional electrons are released, thus creating an electron avalanche, which is detected at an anode as a measurable current. Such electron multipliers can also be used as a part of a photomultiplier tube (PMT), a

device which can detect photons through the ejection of a photoelectron from a photocathode which is subsequently multiplied through a electron multiplier and detected.

The development of a continuous channel electron multiplier (CEM) was made possible by the advancements made in the production of high surface resistance glasses in the 1960s [43]. High voltage is put across the continuous dynode of a CEM which is operated in vacuum. Once a detectable particle hits the wall, the channel emits an electron which is then accelerated down the dynode, hitting the walls multiple times and consequently releasing an increasing number of electrons. The avalanche process ends with a up to 10^8 electrons at the output [43]. Figure 2.7 shows a schematic view of the working principle of a CEM.

The gain of a continuous channel electron multiplier is dependent on several quantities,

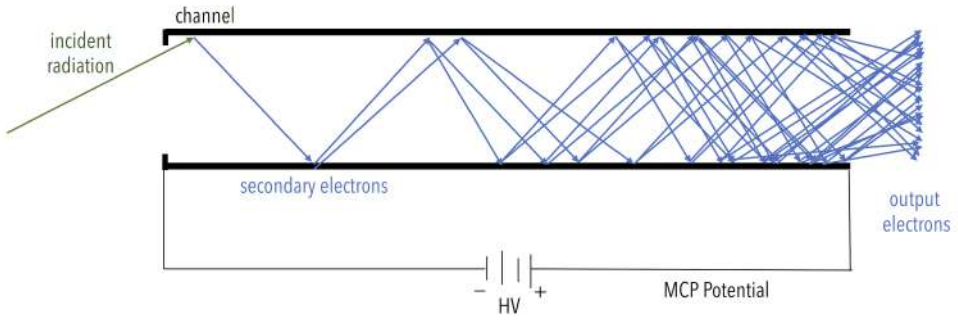

Figure 2.7: Schematic mode of operation of a channel electron multiplier; the incident radiation is shown in green; the from the CEM released secondary electrons are shown in blue

mainly the voltage applied across the channel and the energy with which the incident radiation hits the plate. Additionally it also depends on the length to diameter ratio of the channel as well as the secondary emission coefficient [44]. At high gains, the effect of ion-feedback needs to be taken into consideration as it not only lowers the channels capacity, but also decreases the lifetime of the CEM [44]. Ion feedback happens when the growing electron avalanche within the channel starts to ionize residual gas. The bias across the CEM then accelerates these ions back to the front side of the channel, where they subsequently hit the wall and produce further secondary electrons which can be seen as smaller pulses following the main output signal. By using curved channels these ion-feedback effects can be reduced, as the residual gas-ions hit the wall with lower energies which decreases the probability of secondary electron emission [45].

Since most of the electrical performance properties of CEMs are dependent on the aforementioned length to diameter ratio $\alpha = l/d$, the size of these channels can be reduced to a limit determined by manufacturing capabilities and thus several of these small CEMs can be assembled parallel to each other, and bound together to form a MCP [43].

Nowadays, modern microchannel plates are manufactured using fibre drawing techniques. The process [44] starts with two part glass fibres consisting of a non-etchable lead glass tube and a etchable glass core. After these single fibres are heated and drawn for the first time, they are assembled into a hexagonal rod. This array of fibres is drawn again. The resulting multi-fibres are stacked and fused together to a hexagonal 'boule'. This is then sliced to create the MCP wafers, which are then polished and treated with a chemical etchant to remove the glass cores of the fibres. Thereafter the wafers are heated and reduced in a hydrogen oven to convert the channel walls into semiconducting surfaces, assuring that secondary electrons can be emitted. In the last step, electrodes are deposited on each sides of the plate.
A schematic figure of a MCP can be seen 2.8a , showing it's several small CEM's assembled parallel to each other. Just like for individual CEMs the gain of a single straight

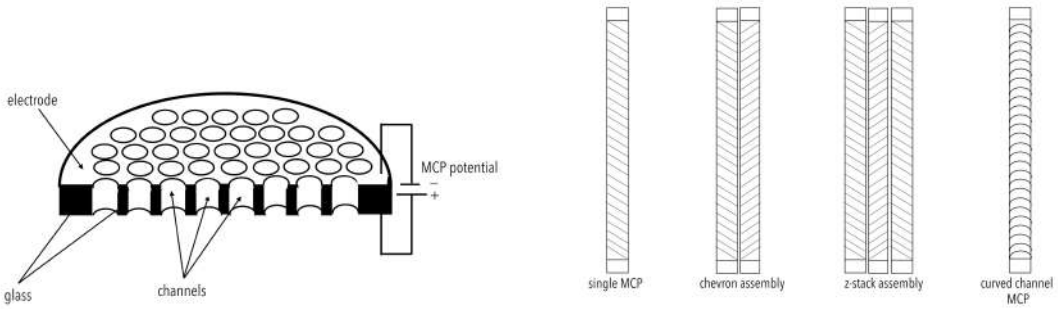

(a) Schematic view of a MCP *(b) Different MCP configurations*

Figure 2.8

channel MCP is limited by ion-feedback. To circumvent this problem and subsequently achieve higher gains, several other MCP configurations are possible [43]. A single microchannel plate with straight channels can achieve a gain of $\sim 10^3 - 10^4$ whereas a MCP with curved channels can reach $\sim 10^5 - 10^6$ [45]. However especially small sized curved channel MCPs are difficult to manufacture.
The second option is to stack two or three straight channel MCPs. In these, the channels are tilted by $8° - 15°$ against the input surface normal [43]. When using multiple plates they are oriented such that channel of neighbouring MCPs are tilted in opposite directions. This results in a chevron pattern for 2 and a z-pattern for 3 plates. The mentioned MCP configurations can be seen in figure 2.8b. These stacks significantly improve ion feedback as the produced ions are captured in between plates when travelling back towards the front plate and can therefore achieve higher gains than a single microchannel plate. MCPs stacked into a chevron pattern can reach gains of $\sim 10^7$ and z-stacks up to $\sim 10^8$ [43].
Ion-feedback does not only depend on the MCPs configuration, but also the amount of residual gas within the channels as well as the cleanliness of their surface [46].

2.3.2 Anodes

Once the generated electrons leave the backside of the microchannel plates, they are accelerated towards and collected by an anode, such that a current can be measured. The simplest type is a solid anode, which has the disadvantage that it can not be used to evaluate the position of the incoming particle hitting the front side of the MCP. However, several more intricate types of anodes exist, which are position sensitive. This includes a cross-strip anode, where each of the strips are read out individually and the position is calculated from the charge in each of them, or a quadrant anode where the relative charge in the quadrants is used to obtain the position [47, 48]. The wedge-and-strip anode consists of a periodic array of electrodes which vary in size and are shaped like wedges and strips. The position of the charge cloud can be determined from the ratio of charges in each of the electrodes [49, 50]. Another position sensitive anode is the delay-line anode which will be described in more detail below.
Even though the spatial resolution of a microchannel plate is limited by the dimensions of a single channel, the actual position sensitivity depends on how much of the spatial information is retained once the charge cloud arrives at the anode [51]. Therefore, depending on the necessary imaging and timing precision a suitable anode has to be chosen.
As an alternative to using an anode, it is also possible to position a phosphor screen behind the MCP stack. In this case the photons ejected by the screen are detected with either a charge-coupled device (CCD) or a complementary metal-oxide-semiconductor (CMOS)-sensor [52]. However, these cannot be used to analyse multi-hit events, as even for the fastest CCD's and CMOS-sensors, the read-out of the optical image produced by the phosphor screen is too slow [39, 53, 54].

Delay-Line-Anode

The delay-line anode utilizes the time a signal takes travelling through a helical or meander shaped wire. These specific shapes increase the propagation time of the signal into a specific direction [51]. A schematic view of a meander shaped delay line can be seen in figure 2.9 showing transmission lines in green and red.
Once a charge cloud from the MCP's, which is shown in black, hits the delay line, it induces a signal, which then travels in both directions towards the end of the wire. The time difference Δt between the signal arriving at one end of the line and the other end can be used calculate the position of the hit. By using a second delay-line which is aligned perpendicular to the first one, 2D imaging can be achieved [51]. Even if the charge cloud hits several sections of the meander or helical wire, the centre-of-mass of the cloud can be interpolated and therefore a continuous image can be created [39]. The position (X, Y) of the particle hit can be calculated from the arrival times at the end

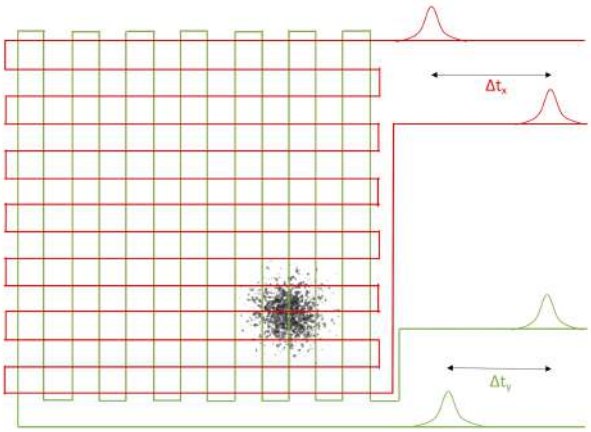

Figure 2.9: Schematic view of a delay line anode

of each wire $(t_{x,1}, t_{x,2}, t_{y,1}, t_{y,2})$.

$$\begin{aligned} X &= t_{x,1} - t_{x,2} + O_x \\ Y &= t_{y,1} - t_{y,2} + O_y \end{aligned} \tag{2.40}$$

where O_x and O_y are arbitrary offsets [55]. Additionally, it has to be noted that their sum $T_x = t_{x,1} + t_{x,2}$ and $T_y = t_{y,1} + t_{y,2}$ is the same no matter where the charge cloud hits the anode, as it is equal to the time needed to pass over the entire length of the wire [39].
In each layer (direction), the anode also contains a second wire. By applying a smaller potential to this reference wire, it can be assured that the electrons are collected and distributed equally between the signal wires of both layers [51, 54].
Once the signal is collected at the end of the wires it is amplified and fed to a Time-to-Digital-Converter (TDC) so that it can be further analysed. The readout electronics used in such a detector are described in section 3.2.
To characterize the proton source and later detect H^* in the ASACUSA experiment, a MCP delay-line detector, using two microchannel plates assembled in a chevron configuration, was chosen. It will be described in more detail in section 3.2.

Chapter 3

Experimental Setup

In this chapter, the design, construction and setup of the proton source is described. Furthermore, it covers the MCP delay-line detector used for the characterisation of the source. Additionally this section explains the vacuum system, electronics and programs necessary for the operation of both, source and detector.

3.1 Proton Source

As mentioned previously, the low energy protons necessary for ASACUSA's matter studies are produced using electron impact ionisation in H_2-gas.
For this purpose, the source consists of three separate modules (see figure 3.1), the electron gun, gas cell and the ion extraction, each described separately below. The

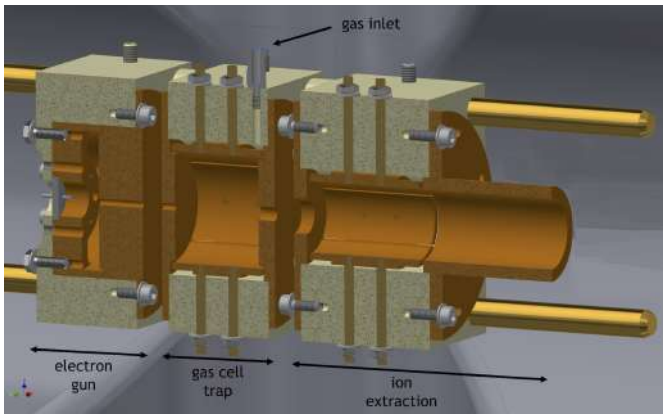

Figure 3.1: 3D rendering of the proton source with the electron gun, gas cell and extraction modules

first component, the electron gun, emits electrons which are then extracted and focused into the second module, the gas cell. Within the gas cell, a mechanically compensated penning trap, the electrons ionize H_2-gas, producing protons as well as several other ions, including H_2^+ and H_3^+. In the last step, the extraction module is used to focus and steer the beam into the Cusp trap.

The modules are mounted on metal rods, which are directly screwed into the vacuum flange.

3.1.1 Electron Gun Module

Within the electron gun module, the e^--beam is produced by a hairpin tungsten filament. The housing electrode both surrounds the filament and is used as it's ground. Mounted on the opposite side, the anode extracts and focuses the e^--beam into the gas cell. Electrons can leave the module through the 2 mm hole in the centre of the anode. Both electrodes are fabricated from oxygen-free high thermal conductivity (OFHC) copper.
Eight evenly distributed rod magnets are assembled around the electrodes at a radius of 25 mm. These magnets produce the magnetic field for the gas cell trap and will be further described in section 3.1.2.
To complete and hold the module together, all electrodes and magnets are supported by a Polyoxymethylene (POM) structure which is also used to slide the module onto the metal rods and fix it into the right position. Due to it's heat production during operation, the filament is mounted on an aluminium ring which is attached at the back of the module.
In addition to pumping holes, vented vacuum screws assure that the volume within the electron gun can be pumped sufficiently. For the operation of the filament, an adequate vacuum pressure of at least 10^{-5} mbar is necessary within this module. At higher pressures electrons emitted produce residual gas ions, which in return are attracted to the filament's negative potential. Over time this can lead to the destruction of the filament due to sputtering of its material [56, 57].

The drawing of the electron gun module with it's electrodes can be seen in figure 3.2. The trajectories of electrons from the filament were simulated in SIMION showing that they can, with the help of the anode, be focussed straight into the gas cell trap.
Figure 3.3 shows the trajectories of electrons emitted by the filament. In this simulation 100000 electrons are released at an energy of (1 ± 0.5) eV. The housing electrode is kept at 25 V, the anode voltage varied. The gas cell potentials are (113 V-110 V-113 V) for (gas cell entrance, gas cell ring electrode, gas cell exit), extractions entrance and exit electrodes are grounded and the steerer voltages are set to 100 V.
The simulation in sub-figure 3.3a shows the trajectories at 10 V applied on the anode. If no voltage is applied, the electrons are accelerated back to the housing electrode and do not enter the gas cell. This can be used to turn the proton source off. Sub-figure 3.3b shows the trajectories at 150 V applied on the anode. Here the electrons are focussed through the 2 mm hole into the gas cell were they can ionize the H_2-gas.
POM distancing plates separate the electron gun and the gas cell module. Maintaining an exact distance between these modules is vital, as the magnetic field depends on the

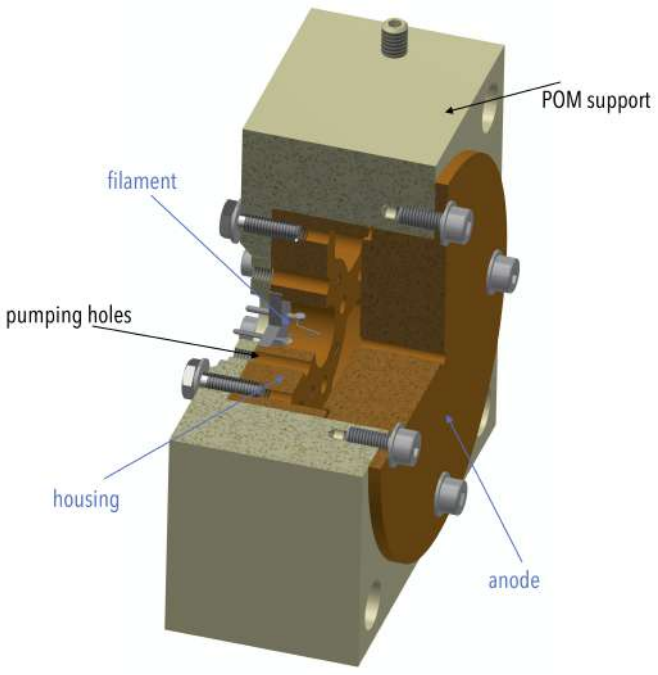

Figure 3.2: Drawing of the electron gun with the filament and it's two electrodes, housing and anode; the magnets are assembled inside the POM support

position of the rod magnets which produce it.

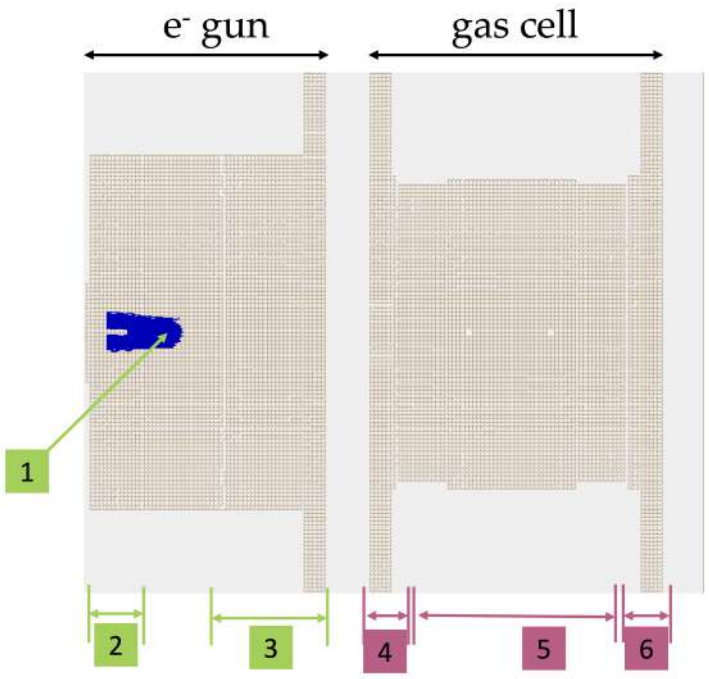

(a) Wehnelt = 10 V

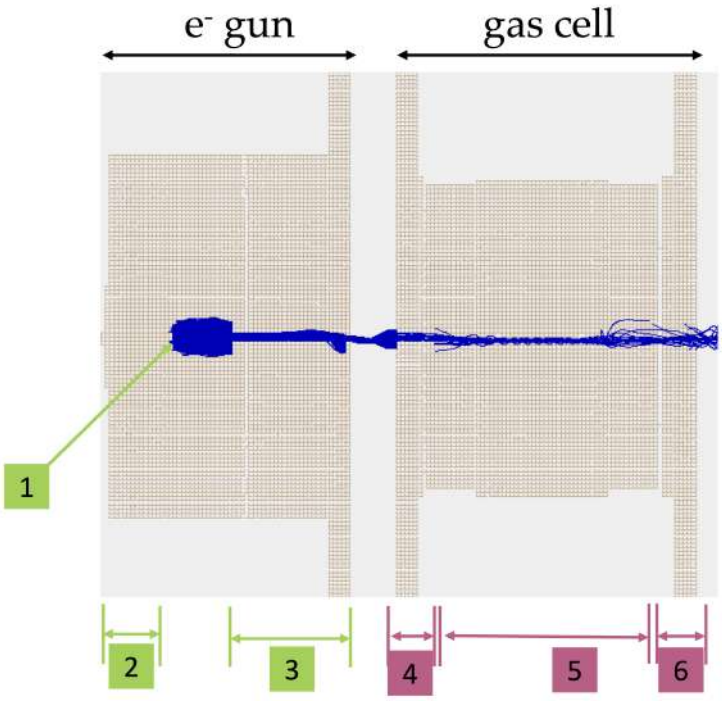

(b) Wehnelt = 150 V

Figure 3.3: Simulations of the electron trajectories at a anode voltage of (a) 10 V *and (b)* 150 V*; the electrodes of the electron gun module can be seen on the left side labelled in green: filament (1), housing (2), anode (3); the electrodes of the gas cell modules are visible to the right in pink: entrance (4), ring (5), exit (6)*

3.1.2 Gas Cell Module

The gas cell module is a mechanically compensated cylindrical penning trap. Once the electrons enter the gas cell, they ionise H_2-gas. After their production, protons, and other ions can either immediately be extracted or trapped by the module. Technical drawings of the module can be found in figure 3.4. Just like for the electron gun, the electrodes and magnets in this module are mounted on a POM-carrier. The H_2-gas is transported into the gas cell trough a gas inlet and plastic tube.

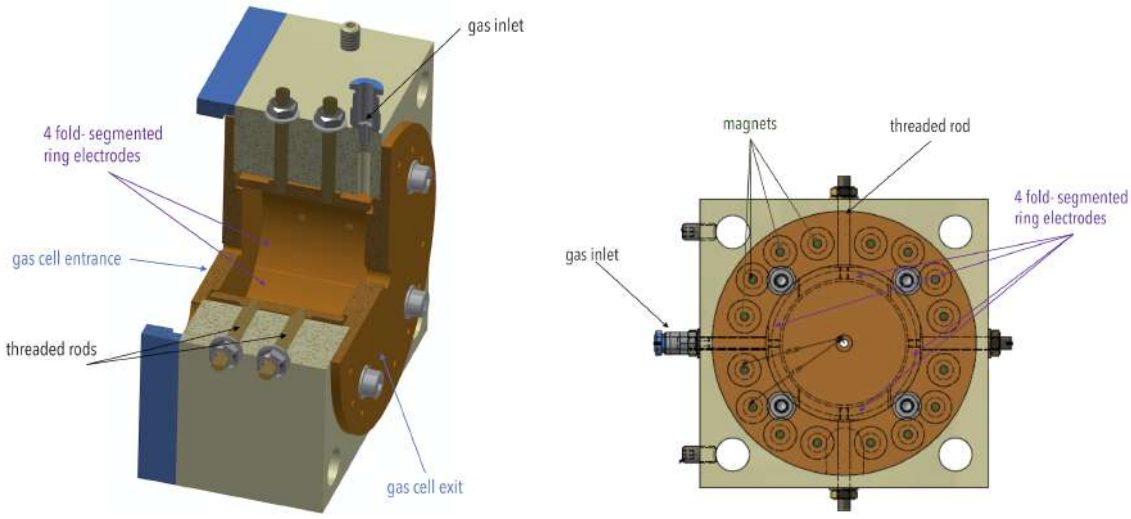

(a) Gas cell module; endcap electrodes are secured to either side of the 4-fold segmented ring electrodes, which are held in place and contacted with brass threaded rods; H_2-gas is inserted into the module via a plastic hose and gas inlet.

(b) Cross-section of the gas cell module; the magnet positions are shown with green dots; the ring electrodes are indicated with dashed lines.

Figure 3.4: Technical drawings of the gas cell module.

The magnetic field

The radial confinement of a penning trap is provided by a magnetic field B_z, which is often produced by solenoids. However in the case of this proton source, permanent neodymium (NdFeB) rod magnets are used instead. These magnets are 30 mm long cylinders with a diameter of 8 mm. With a remanence B_r of ≈ 1.3 T their main advantages are the low cost and simplicity, as they can be installed quickly and require no cooling.

Several simulations of the magnetic fields generated by different magnet assemblies and the behaviour of electrons and protons in them are conducted in COMSOL. Firstly the magnetic field a ring of 12 and 16 magnets positioned around the gas cell module electrodes is simulated. However, in both cases the reversal point of the magnetic field (point where B_z changes the sign) lies in between the gas cell and electron gun module. Therefore it is impossible to use this configuration, as the electrons cannot enter the

gas cell module.
In order to move the reversal point, two additional layers of magnets, one in the electron gun described in 3.1.1, the other in the extraction module (section 3.1.3) are added. Simulations are conducted for stacks of 6-12-6, 6-16-6 and 8-16-8 magnets with varying distances from $10-14\,\mathrm{mm}$ between each layer. Several of these options are able to move the reversal point beyond the electron gun.
For the final design other variables such as the magnetic field strength and the homogeneity of the magnetic field B_z in the centre of the trap have to be taken into account. Additionally the distance between the layers cannot be too small, as the endcap electrodes of the modules still have to fit between them. The largest magnetic field strength is generated by a 6-16-6 stack followed by 8-16-8 and then 6-12-6. However ultimately a stack of 8-16-8 with 12 mm between each layer magnets is chosen for the proton source design. This is due to the fact, that the layers can be placed further apart than in either of the other options, while still keeping the reversal point beyond the electron gun.
The magnetic field strength and homogeneity does not only depend on the number of magnets but also on their radial position. As the ring electrodes, which will be described later, are fixed in place and contacted by threaded rods, the magnets need to be assembled around them. For the electron gun and ion extraction module the 8 magnets can be evenly distributed on a circle with a radius of 25 mm, however this is not possible for the 16 magnets of the gas cell module, as the distance between the magnets is too small for a threaded rod to fit through. Therefore the magnets in this module are assembled in four groups of 4 with a longer distance between each group.

Simulations show that the field is more homogeneous when the inner two magnets of each group of 4 in the gas cell module are positioned at a slightly larger radius of $r = 27\,\mathrm{mm}$ than the outer magnets.
The final layout of the gas cell's magnets can be found in figure 3.4b. It shows the position of the threaded rods and the four groups of 4 magnets each. The outer ones of each group are positioned at a radius of $r = 27\,\mathrm{mm}$ while the inner ones, are at $r = 25\,\mathrm{mm}$.
The simulation of the z-component of the resulting magnetic field as well as the positions of each of the modules are shown in figure 3.5. The magnetic field strength in the very centre of the trap, created by this assembly is $0.072\,\mathrm{T}$.

The electric field

The axial confinement of ions is provided by a quadrupole electrostatic potential. It is produced by two flat endcap electrodes (called gas-cell entrance and gas-cell exit) and a 4-fold-segmented ring electrode, which are, as is the case for the electron gun, made from OFHC-copper.
Electrons can enter this module through the 2 mm hole in the entrance electrode and

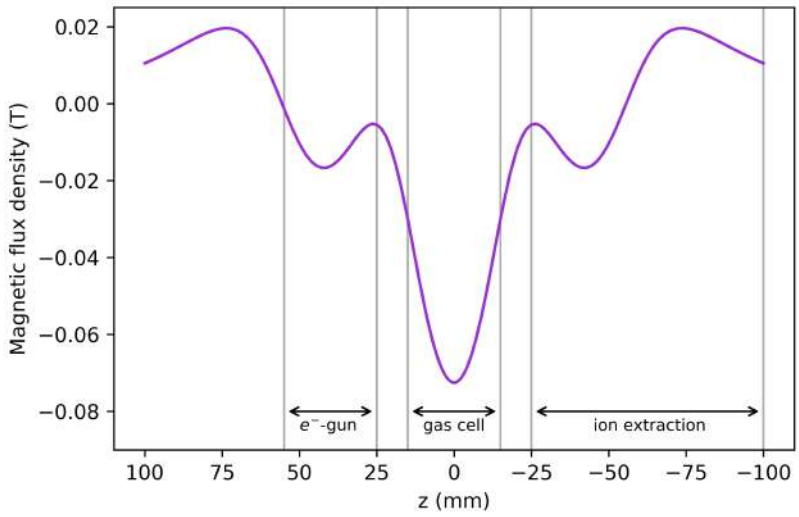

Figure 3.5: z- component of the magnetic flux density throughout the proton source

ions can leave through the 4 mm hole in the exit electrode.
This module can be operated in several modes depending on the voltages applied to the electrodes.
In **continuous mode**, the potential of gas-cell entrance is set higher than the ring and the potential of the exit electrode is set lower. In this case the gas cell does not act as a penning trap, instead the protons are created and immediately extracted thereafter, and sent towards the detector.

In **trapping mode**, initially both gas-cell entrance and exit are set higher than the ring electrode. Once an electron bunch is inserted into the module, the protons are generated and then trapped inside. In this case the H_2-gas also additionally acts like a buffer gas cooling the protons. As mentioned in section 2.2.1 when buffer gas cooling is used, the magnetron motion of the particle becomes unstable and it's radius increases over time. To counteract this process RF-pulses can be applied to the ring electrodes. The main advantage of using sideband cooling is that the application of the mass-dependent cyclotron frequency allows for selective centring of the protons. Subsequently, other ions produced during the ionisation process (mainly H_2^+ and H_3^+) can be removed once the RF-pulses are applied.
The cyclotron-frequency for protons in the simulated magnetic field of the trap is:

$$\omega_c = \frac{q}{m} B = 6.91\,\text{MHz} \tag{3.1}$$

The applied RF-frequency for centring of protons is:

$$f = \frac{\omega_c}{2\pi} = 1.10\,\text{MHz} \tag{3.2}$$

The RF-pulses necessary for sideband cooling have sinusoidal shape, and are applied to the 4-fold-ring electrode such that the two electrodes opposite of each other receive RF-pulses that are in phase, whereas the other two receive a pulse shifted by 180°.
It is also possible to apply rotating wall RF-pulses. Again these pulses have a sinusoidal shape, but this time the pulses of neighbouring ring electrodes are each shifted by 90° creating a rotating electric field.
Finally, protons can be extracted from this module by lowering the potential of the exit electrode.
Figure 3.6 shows the simulated trajectories of two protons captured in the trap with an initial energy of 100 meV. The potentials on the endcaps are set to 10 V and the ring electrode to 0 V. The protons behave as expected for an ion confined in a penning trap, as elaborated on in section 2.2.1. Figure 3.6a shows the radial motion of the two protons, which is a superposition of reduced cyclotron and magnetron motion. In figure 3.6b the time dependent axial motion is plotted. Here, the two protons oscillate harmonically between the endcaps of the gas cell module.

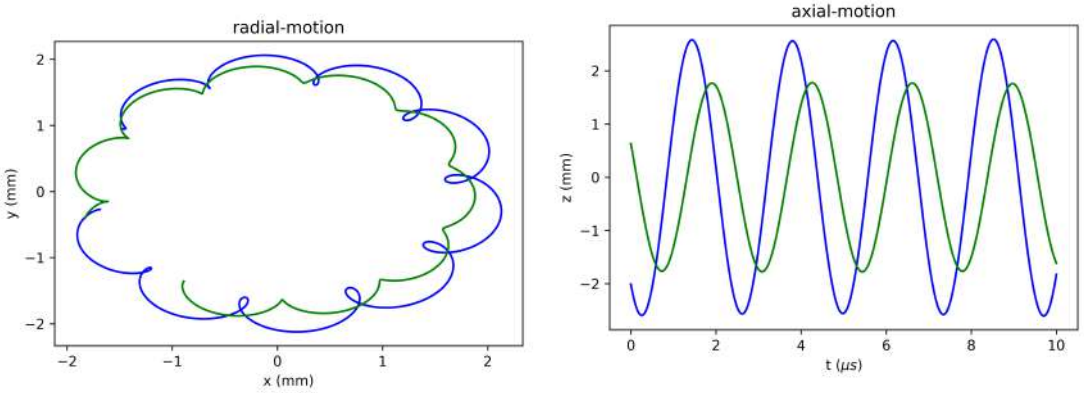

(a) The radial motion is a superposition of the reduced cyclotron and magnetron motion

(b) The axial motion of the protons is a harmonic oscillation between the endcaps; $\omega_z \approx 4.24 \times 10^5$ Hz

Figure 3.6: Trajectories of two protons trapped in the gas cell

3.1.3 Extraction Module

The extraction module is the third and final part of the source. It is used to both focus the beam of protons as well as steer it into a desired direction.
It contains the eight evenly distributed magnets for the penning trap magnetic field. It additionally consists of a flat entrance electrode with a 10 mm hole through which the protons enter.
The 4-fold segmented ring electrode is used to steer the protons. Each of the four electrodes is used as a deflection plate and by applying different voltages to each the ions can be moved into a desired direction.

A cylinder shaped exit electrode with an inner radius of 20 mm is used to bring the electric potential back to ground. The technical drawing of this module is shown in

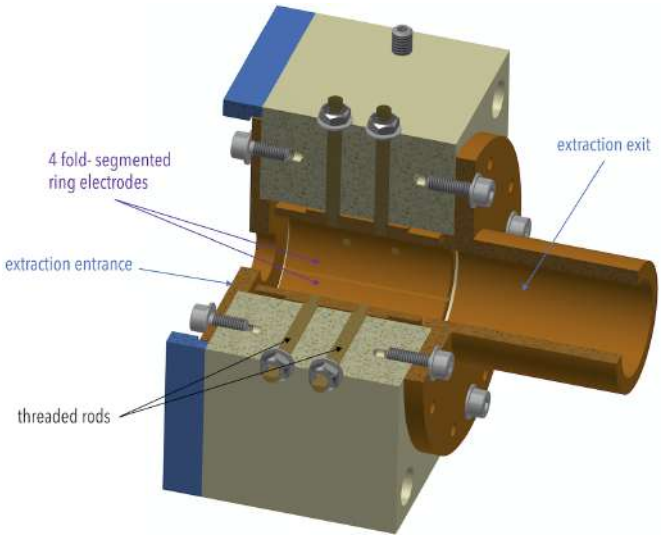

Figure 3.7: Technical drawing of the extraction module; the 4-fold segmented ring electrode is indicated with purple arrows and is contacted through threaded rods. The flat entrance electrode and cylindrical exit electrode are needed for focussing the beam; the POM-carrier is shown in beige

figure 3.7. Again, a POM-support carries both the electrodes and magnets. Vacuum screws are used to prevent virtual leaks by assuring sufficient pumping throughout the module.

Several SIMION simulations are conducted to assure that the protons can be both focused and steered.

Figure 3.8 shows the trajectories of protons through the gas cell and extraction modules. The following voltages are applied to: gas cell entrance: 123 V, ring electrodes: 110 V, gas cell exit: 103 V. Both extraction entrance and exit electrodes are put to 0 V and the potential of the deflection ring electrodes is varied. (0.5 ± 0.4) eV protons are started from the centre of the gas cell trap.

The simulations show that if the steerer electrodes are grounded, the protons diverge after they enter the extraction module. Starting at 80 V applied to the extraction ring electrode, the beam divergence is visibly reduced. For 100 V a soft focus point can be seen at the very end of the module.

These simulations show that the module can indeed be used to focus the proton beam to different points along the beam axis by applying different voltages to the steerer plates. Additionally, by lowering or increasing the potential of one or two ring electrodes, with the respect to the others, the beam can be moved into a specific direction. This steering of the proton beam is shown in the simulations in figure 3.9.

Just like in the focussing simulations, protons are released with an energy of (0.5 ± 0.4) eV in the centre of the gas cell trap.

The gas cell and extraction entrance and exit voltages are also the same as mentioned above.
The four deflection plates are set to 100 V and one of the four ring electrodes is raised by a varied voltage, the opposite electrode is lowered by the same value.
The remaining 2 ring electrodes are kept at 100 V.
Figure 3.9 shows the beam position moving in the direction of the electrode with the lowest potential, demonstrating that the module can also steer protons.

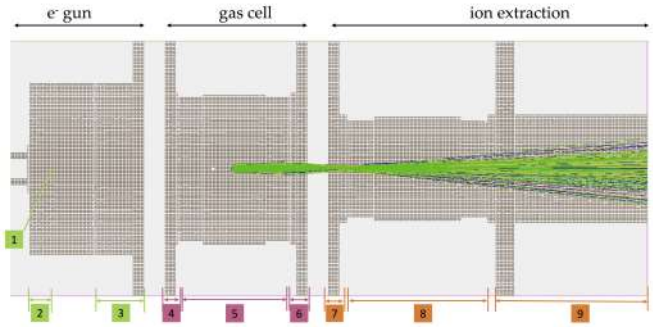

(a) Steerer ring electrodes: 0 V

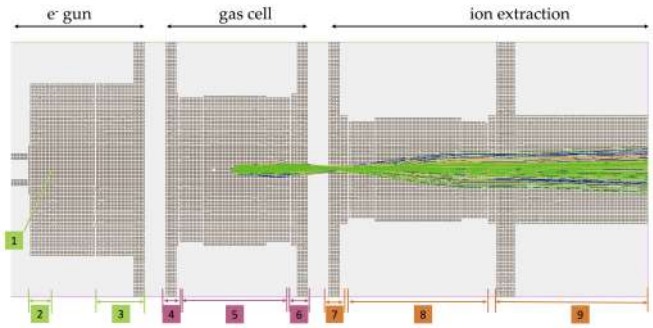

(b) Steerer ring electrodes: 80 V

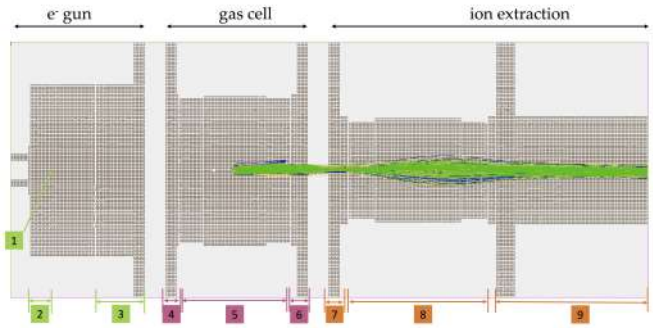

(c) Steerer ring electrodes: 100 V

Figure 3.8: Simulated proton trajectories; Electrodes of the source are labelled using numbers; The voltages in the gas cell module are, entrance (4): 123 V*, ring (5):* 110 V*, exit (6):* 103 V*; extraction entrance (7) and exit (9) electrodes are both at* 0 V *while the deflection plate electrode's (8) potential is varied; These figures show the focussing of the proton beam depending on different ring electrode voltages*

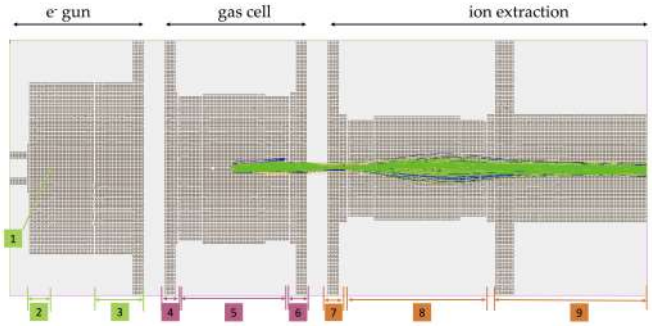

(a) Steerer ring electrodes: 100 V, *ring electrodes 1,3:* 100 V ± 0 V

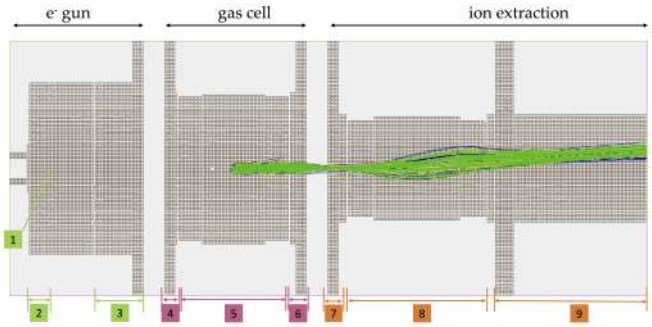

(b) Steerer ring electrodes: 100 V, *ring electrodes 1,3:* 100 V ± 3 V

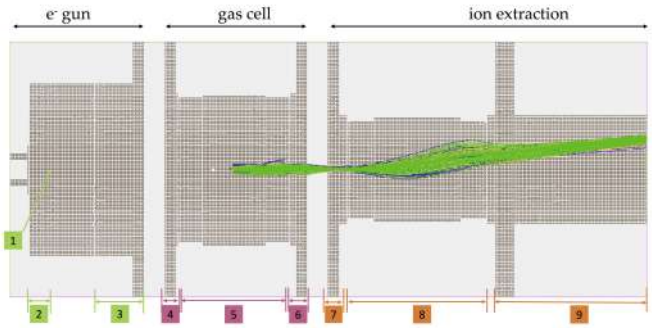

(c) Steerer ring electrodes: 100 V, *ring electrodes 1,3:* 100 V ± 5 V

Figure 3.9: Simulated proton trajectories; Electrodes of the source are labelled using numbers; The voltages in the gas cell module are, entrance (4): 123 V, *ring (5):* 100 V, *exit (6):* 103 V*; extraction entrance (7) and exit (9) electrodes are both at 0V while the deflection plates (8) are set at* 100 V, *two of the plates (positioned opposite of each other) are increased/decreased by a varied voltage*

Lastly, time-of-flight simulations for protons as well as H_2 and H_3-ions were performed. For this the gas cell potentials are set as mentioned in the beam focussing and moving simulations. The steerer electrodes are kept at 100 V. The flight-time of extracted ions depends on the location, energy and relative propagation direction of the ions. Therefore each 10000 H^+, H_2^+,H_3^+, are started from a sphere with a 1 mm radius in the centre of the trap, with energies ranging from 0 eV-5 eV. The respective starting propagation direction is simulated such that the particles initially fly into all 360 °, from their starting position.
Figure 3.10 shows the flight times for the aforementioned initial conditions. Protons are indicated in blue, H_2^+ in orange and H_3^+ in green. It is visible that the flight time

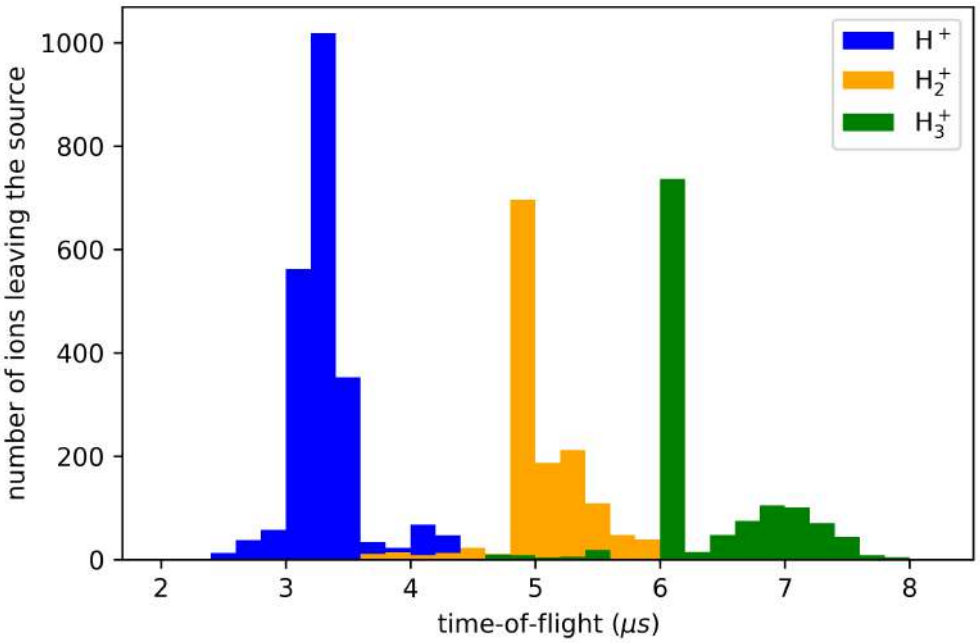

Figure 3.10: Simulation of the time of flight of protons H_2^+ and H_3^+ from the centre of the gas cell to the end of the extraction module; Protons are indicated in blue, H_2^+ in orange and H_3^+ in green.

of protons is lower than that of the other ions, which is due to their smaller mass, but the extraction module itself is too short to fully separate the beam into proton and H_2^+ and H_3^+-bunches.
However, as the detector for characterisation measurements is placed further away, the different particle species are separated even more and can be identified through their time-of-flight.

3.1.4 Assembly

Each of the different modules is assembled separately and then mounted onto the vacuum flange using metal rods. As the source is operated in high vacuum, each of the

components is cleaned by hand followed by soap and alcohol ultrasound baths. To assure the parts are kept clean, only sterilised tools are used during the construction process.
Firstly, the ring electrodes for gas cell and ion extraction modules are attached to the POM support. This is achieved by putting the electrodes into their respective places inside the module and then attaching threaded rods from the outside and securing them into place using nuts.
In order for the positioned magnets not to move out of place in the assembly process, one of the flat electrodes of each module (anode, gas-cell back, extraction front) has a special opening used just for positioning the magnets. These electrodes are put onto the respective modules and held in place by a 3D printed assembly mount. They are then rotated and each magnet is put into place one by one. As these electrodes only have one opening which is rotated, none of the already placed magnets can shift out of position during assembly. Once all magnets are in the correct place, the opening can be rotated to a spot in-between two magnets and the electrode is tightened.
Afterwards the housing electrode and filament are attached to the electron gun and gas cell entrance and extraction exit electrodes are secured to their respective modules.
Next, kapton insulated wires are connected to the copper electrodes using ring terminals.
Once the four metal rods are screwed into place on the vacuum flange, the modules can be pushed on and fixed into place using nylon screws. Between each module POM distancing plates are slid onto the rods to assure the correct distance between the magnets. Once all modules are mounted onto the vacuum flange, the wires are connected to their respective SHV/BNC feed-throughs. Next a plastic tube is affixed to the gas

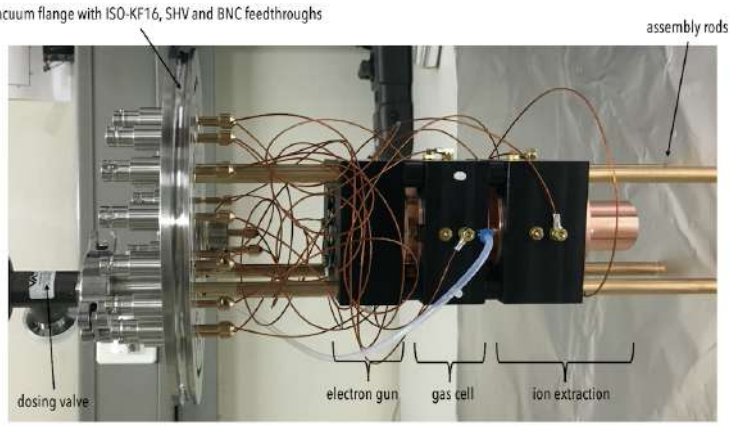

Figure 3.11: Assembled proton source mounted on to the vacuum flange

cell using a push to connect tube fitting. Lastly, the flange is turned around and the other side of the plastic tube is attached to a dosing valve.
The complete proton source can now be installed by mounting the flange onto the vacuum chamber. Figure 3.11 shows the assembled proton source mounted on to the

vacuum flange.

3.2 MCP Delay Line Detector

The detector used for the characterisation measurements and later the exited hydrogen detection in the ASACUSA experiment is a MCP-delay line detector (DLD) with a linear active diameter of 40 mm, produced by RoentDek.

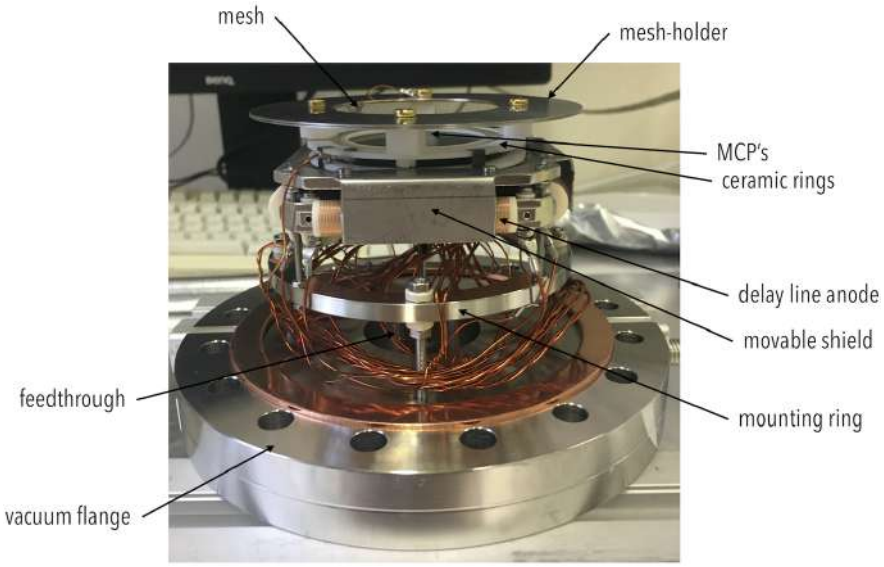

Figure 3.12: Assembled MCP delay line detector

In this setup, two MCP's are used, which are contacted by ceramic rings with metallisation pads and held together using spring clamps. They are assembled such that pores of the MCP's form a chevron pattern. This stack is mounted onto the delay line anode and held in place with the anode's movable shields.
The anode itself is secured to the vacuum flange with the help of a metal mounting ring and threaded rods.
A mesh is attached in the front of the MCP's, using an aluminium mesh holder which is secured to the ceramic rings using nylon screws and distancing cubes. The entire assembled MCP-detector can be seen in figure 3.12.
Two meshes are utilized during the experiments. Firstly, a testing mesh, with holes in the shape of an L, is used to assure the position readout functions properly.
This is then replaced by a second mesh for the characterisation measurements of the source and later also for H^*-detection. It was produced at CERN and is a grid made of copper-beryllium. With it's thickness of less than 0.05 mm and grid pitch of 2.965 mm, it has a transparency of 97.7%.
The MCP's, delay line and mesh are contacted with kapton insulated copper wires, which are connected to a RoentDek FT12 feedthrough on the other side.
Figure 3.13 shows both the testing mesh and the mesh used for characterisation mea-

surements. Just like for the proton source, the parts are cleaned using alcohol ultrasound baths and the detector is assembled using sterilised tools. Before installing the detec-

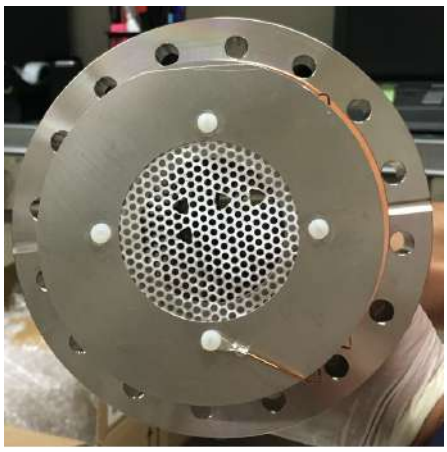

(a) mesh for testing the functionality and position readout the detector

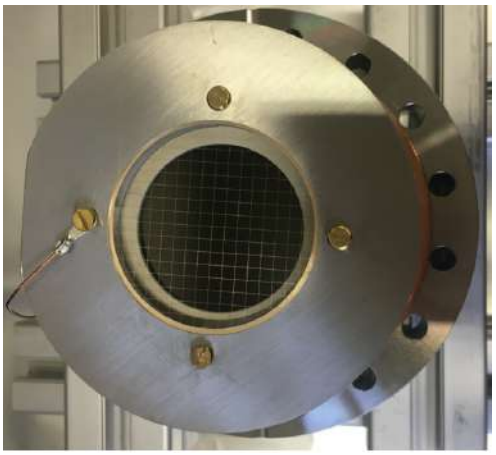

(b) mesh for characterisation and H^* measurements

Figure 3.13: the two used meshes held by the mesh-holder and installed on the detector

tor into the setup for characterisation measurements described in section 3.3, it is first tested and calibrated using a Bayard-Alpert ionisation gauge.
In a CF-100 cross the detector is placed on the opposite side of the ion gauge. Two pumps, a Leybold Scrollvac 15plus and a Turbovac350iX create the high vacuum necessary for the operation of the detector.
Once the detector is mounted onto the vacuum flange, an ohmmeter is used to check for shorts and if the cables are connected correctly. If this is the case, the chamber can be evacuated and a FT12TP signal decoupling plug is connected to the feed-through.
Several voltages are necessary to operate the MCP detector. The power supplies and connections are shown in the appendix in diagram B.6. Firstly, the high voltage supplied to the front side of the MCP stack is delivered by an iseg high voltage power supply (T3 CP300n DP030 DP060). This power supply also delivers the potential for the anode wires. As the signal wires require a higher voltage than the reference wires the supply's 250 V output is split in two and by using three 12 V-batteries an additional 36 V is added to the signal wires.
The mesh potential is delivered by a Keithley Electrometer/High Resistance System, and both the anode holder as well as the backside of the MCP stack are kept grounded.
To make sure all the pores of the MCP are pumped free of residual gas, the detector chamber is kept $< 10^{-6}$ mbar for 24 hours before taking it into operation for the first time. Next it is verified that the continuous noise level is below 1 mV peak-to-peak.
Thereafter the potential on the MCP front can be applied slowly, in 100 V steps. During this procedure, the current drawn from the MCP is monitored and the resistance of the stack $R = U_{front}/I$ is calculated. This resistance value should stay constant. Additionally once the operation voltage of ≈ -2000 V is approached, MCP front and

back signals are checked for dark counts. This can be done by amplifying the signal and then monitoring it using an oscilloscope. The MCP operates normally if a randomly distributed dark count rate of ≈ 100 counts is observed.
The four signals from the delay-line anode are also amplified and observed with an oscilloscope.
To achieve position-readout during normal operation of the detector, the signals are processed further. All devices for this purpose are produced by RoentDek.
The signal from the MCP backside is $50\,\Omega$ terminated, whereas the signal from the front is amplified by a FAMP1+ amplifier and is lead to a constant fraction discriminator (CFD1c) which creates a NIM signal output. This signal is then processed by a TDC (TDC8HP). Signals from all four signal and reference wires are amplified and discriminated by two ATR19-2b modules, and the NIM pulses are also led to the TDC. Signal processing connections are depicted in figures B.7 and B.8.
Measurements are conducted using the CoboldPC program by RoentDek.
During several measurements using the ion gauge, the amplifier settings, MCP and mesh potentials are optimised.
Figure 3.14 shows the measured hits on the detector for different MCP-front potentials. The measurement time is 120 s, and the voltage supplied to the mesh is $-5\,\mathrm{V}$. It can be seen that 1800 V (figure 3.14a) is a too weak potential for the operation the detector, as it is not sensitive over the entire area. For 2200 V (figure 3.14b) the detector can resolve hits over the entire active area. As mentioned in section 2.3.2, the sums T_x,

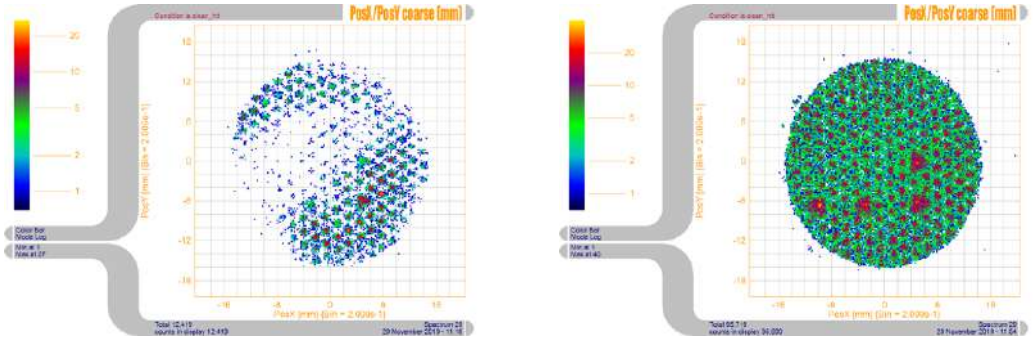

(a) MCP-front potential $= -1800\,\mathrm{V}$ *(b) MCP-front potential* $= -2200\,\mathrm{V}$

Figure 3.14: Detected hits from the ion gauge for different MCP-front potentials; measurement time $= 120\,\mathrm{s}$*; mesh* $= 5\,\mathrm{V}$

T_y of the arrival times $t_{x,1}$,$t_{x,2}$ and $t_{y,1}$,$t_{y,2}$ are constant for all positions. Setting the thresholds too low in the discriminator modules can lead to 'pre-trigger' events. These events can be seen in the timesum spectrum next to the narrow peak for the correctly discriminated events. Therefore the timesum spectrum can be used to optimize the amplification and threshold settings.
Figure 3.15 shows the timesum spectrum in x direction before and after optimisation. Adjusting the threshold settings results in a reduction of events that are not in the correct peak. The corresponding events in a 2D-plot before and after optimization are

depicted in figure 3.16. It is visible that the wrong events don't occur randomly distributed on the entire detector. It is therefore important to reduce them as much as possible. Even after optimisation process a few wrong events are left over. They can

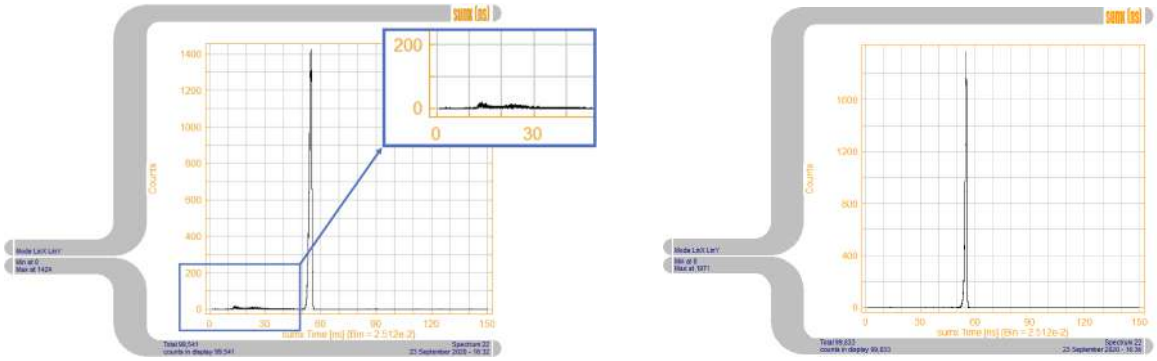

(a) Before optimisation *(b) After optimisation*

Figure 3.15: Timesum spectra of the x-direction

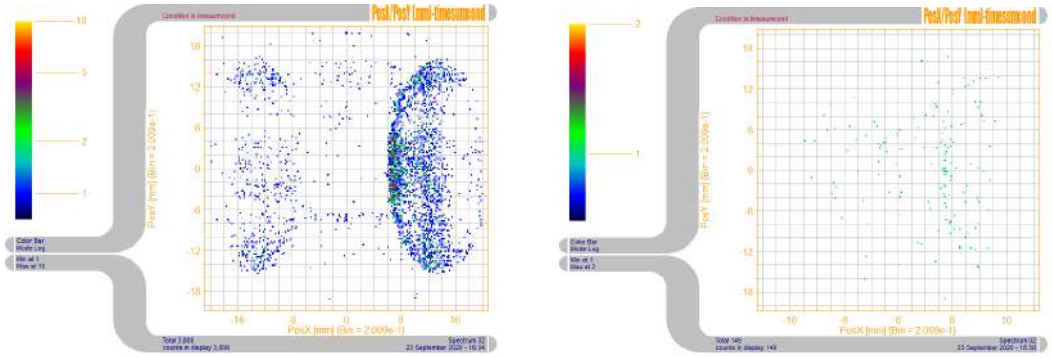

(a) Before optimisation *(b) After optimisation*

Figure 3.16: Events with the wrong time-sum

be seen in figure 3.16b. Therefore a timesum-cut is implemented in the measurement analysis. Using this cut, the remaining pre-tigger events are removed and only the events that have the correct timesum are analysed. An additional cut, called clean-hit, is implemented. As the different anode wires are assembled on top of each other, the wire closest to the backside of the MCPs should register a hit first. Followed by the next wire and so on. Any events that do not fulfil this order are cut by the analysis.
Additionally several tests varying the base-voltage applied to the signal and reference wires from $240 - 300\,\mathrm{V}$ and the mesh potential from $-30\,\mathrm{V}$ to $30\,\mathrm{V}$ are conducted. However, no significant changes in the detector readout are observed. Therefore, the voltage supplied to signal and reference wires is set to $250\,\mathrm{V}$ and the mesh potential to $0\,\mathrm{V}$ for all further measurements.

3.3 Setup for characterisation measurements

In order to properly characterise the source before installation into the ASACUSA-experiment, a test-setup was built. In this setup, the MCP delay line detector was placed opposite of the source enabling the measurement of the number, and position of the ions produced by the source.

For their operation, both the filament as well as the MCP detector need a sufficiently good vacuum of $< 10^{-5}$ mbar and $< 10^{-6}$ mbar respectively. Later on the proton source will be installed directly in front of the Cusp trap. To achieve it's entrance pressure of 10^{-11} mbar additional differential pumping will be necessary.
Figure 3.17 shows the entire vacuum system of the characterisation setup. The proton source (purple) is installed horizontally into an ISO-160 cross. At the bottom of this chamber an additional 6 way cross reducing ISO-160 to KF is placed. Attached to this cross is the pressure gauge (PG1) for the proton source chamber. Finally, at the very bottom an Agilent Technologies TwisTorr 304 FS turbo-molecular pump (turbomolecular pump 1 in the figure) is connected. This pump is backed by a scroll pump (Leybold Scrollvac 15plus) necessary for the producing initial rough vacuum.

The detector (pink), with the mesh for characterisation measurements, is placed horizontally into a CF-100 cross which is connected to the source chamber via an ISO-CF adapter. To improve the vacuum even more, a second turbo-molecular pump (Leybold Turbovac 350iX - named turbo-molecular pump 2 in the figure) is attached to the bottom of the detector cross.
This pump is attached to the 6 way cross via a hose so that it can also be backed by the scroll pump.
The ion pressure gauge (PG2) for the detector chamber is located at the top of the cross. It is only used in-between measurements, as it produces ions which generate signals in the detector.
Both turbo-molecular pumps have valves placed at the back such that de-pressurisation and pressurisation processes can be controlled. Both these valves are shown as red rectangles in figure 3.17.

As the proton source uses H_2-gas for it's operation, the specially designed ISO-flange has a KF-16 feed-through to which a dosing valve is connected. As explained in section 3.1.1, inside the vacuum chamber, the H_2-gas is led directly into the gas cell module via a plastic tube. This assures that the gas enters the gas cell module and doesn't just fill the entire vacuum chamber.
On the outside the dosing valve is connected to a Mars H_2-generator via a hose. A regulate valve is placed in-between to assure that the H_2-pressure produced by the generator is in a range that the dosing valve can handle.

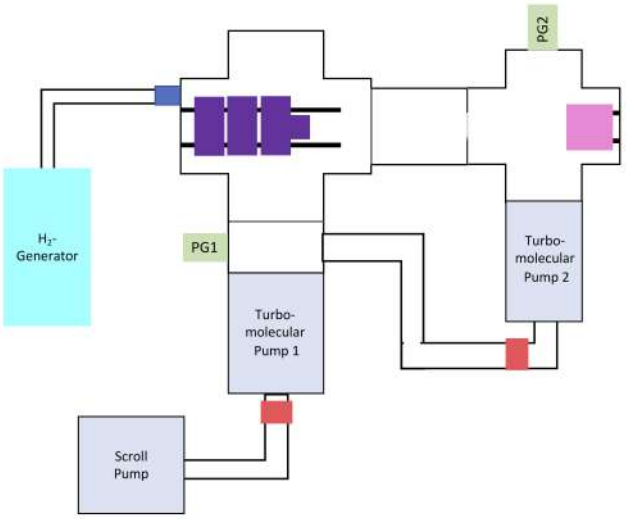

Figure 3.17: Schematic vacuum-setup for proton source (purple) and detector (pink); The proton source is put into an ISO-160 chamber connected via an adapter to the CF-100 detector chamber, PG1 and PG2 are pressure gauges; vacuum pumps are shown in light blue, valves in red. The dark blue valve is the dosing valve connected to a H_2-generator

The source-flange also includes 12 SHV connectors for voltages necessary to operate the gas cell and ion extraction modules. 2 ground-shield BNC feed-troughs are used to apply potentials to the anode and housing in the electron gun. The filaments voltage is supplied via a floating shield BNC connector.
Filament and housing are operated with a Rohde& Schwarz HMP2020 programmable power supply. Voltages for extraction entrance and exit a supplied from a Intertechnique 4-channel bias supply, and the rest of the source's voltages are delivered by a programmable CAEN eight channel High Voltage (HV)-power supply.
The voltages for all segments of the gas cell's ring electrode are supplied by only one of the outputs of the CAEN power supply. A RF-coupling box is used to split this voltage into four and additionally add the radio-frequency pulses used for sideband cooling or the rotating wall method. The circuit diagram can be found in the appendix in figure C.1.
This box also enables the application of extraction pulses on gas cell entrance and exit plates. Bunches of ions are extracted by raising the potential of gas-cell entrance while lowering the potential of the gas cell exit electrode.
Two BK Precision 30 MHz Dual Channel Function/Arbitrary Waveform Generators are used to supply the rectangular extraction and sinusoidal cooling pulses to the RF-coupling box. The two outputs from the frequency generator delivering the cooling pules are divided by two Mini-Circuits power splitters creating the four necessary RF-pulses for the gas cell ring electrodes. Figure 3.18 shows the measured output voltage of the Mini-Circuits power splitters at a frequency of 1 MHz. They shift one the outputs by 180° and also reduce the hight of the pulses to $(65.64274 \pm 0.00008)\%$ of the applied value. This value stays the same for different frequencies.

The CAEN power supply and both frequency generators are controlled remotely with

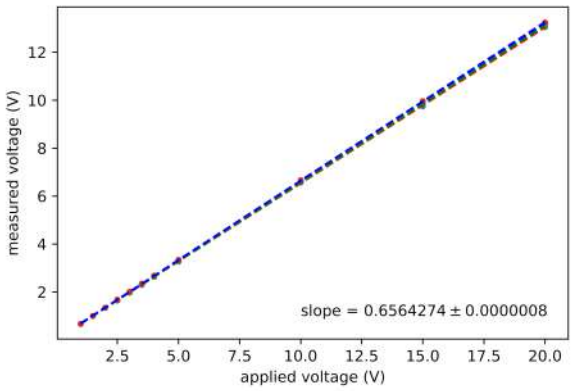

Figure 3.18: Measurement of the output voltage of the Mini-Circuits power splitters depended on the voltage supplied to them by a frequency generator

LabVIEW programs. The electronic connection diagrams for the operation of the proton source can be found in the appendix in figures B.1,B.3,B.4,B.2 and B.5.
The detector is set up as discussed in the test measurements above. However at some point during the measurements, the detector developed an area of lower sensitivity. This is thought to be due to the age and improper storage of the MCP. The signal is improved by raising the voltage applied to the MCP-front to $-2250\,\mathrm{V}$ and adjusting the thresholds in the FAMP1+, CFD1c and ATR19-2b modules. During this process, the signals are monitored on an oscilloscope. As this area is not completely removable, even with the increased potential, most measurements are conducted with the proton beam steered to the sensitive area of the detector.
In order to enable time-of-flight spectroscopy, the extraction pulse signal from the gas cell exit electrode is discriminated by a LeCroy Quad Discriminator and fed into the TDC.
Measurements are recorded using RoentDek's CoboldPC program and controlled using LabVIEW.

Chapter 4

Results

In order to test the working principle of the proton source, it was evaluated using the characterisation setup described in section 3.3.

4.1 Continuous Mode Measurements

For the initial measurements, the source is set into continuous mode. Housing and anode electrodes are set to 25 V and 150 V, respectively. The housing potential is used as the filament's ground and even though the operational current of the filament is specified as 2.1 A, it is only operated at 1.725 A. This is a precautionary step to limit the ion production and to ensure that the MCP-detector is not destroyed via ionic feedback (see section 2.3.1). Using these voltages the electrons can be focussed into a beam emitted from the electron gun module.

The gas cell ring electrode has 110 V applied. The electrons produced by the electron

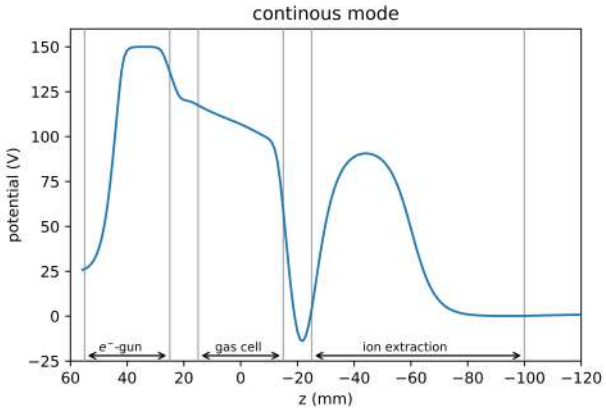

Figure 4.1: Potential inside the proton source during operation in continuous mode

gun have an energy of 85 eV inside the gas cell. At this value, the cross section for proton production in an electron impact ionisation process in H_2-gas is $7.94 \times 10^{-22}\,\mathrm{m}^2$ whereas the cross section for H_2^+ is $9.02 \times 10^{-21}\,\mathrm{m}^2$. This value is not the optimal value

which is found at 95 eV, however this can be changed in the final operational mode of the proton source by either lowering the housing potential by 10 V or increasing all other potentials by 10 V.
Next, 120 V are applied to the gas cell entrance electrode and the exit electrode is set to 100 V. This results in a ramp potential within the gas cell, which continuously extracts the ions that are produced within it.
The extraction entrance and exit electrodes are grounded and 90 V are supplied to the ring electrodes, mimicking the values used in the focussing simulations which achieved a soft focus point (for the focussing simulations see figure 3.8).
The resulting potential inside the source in this mode is shown in figure 4.1. For all further measurements, unless otherwise explicitly stated, the H_2-valve is opened such that the pressure inside the proton source chamber is 1×10^{-6} mbar.
Using these initial values an ion signal can be produced on the detector. However, as mentioned above, the detector has an area of lower sensitivity and subsequently some of the signal is lost. Therefore the ring electrodes are varied such that the beam is moved to the sensitive area of the detector. Figure 4.2 shows the 2D spectrum of all ions observed by the detector. In this spectrum, the beam spot is visible in the bottom

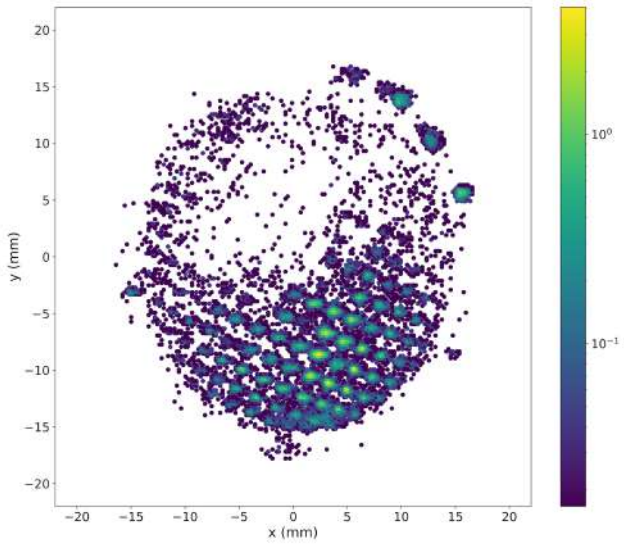

Figure 4.2: 2D spectrum of the MCP-detector; measurement time = 60 seconds, extraction ring electrodes are set to S1: 90 V, S2: 88 V, S3: 88 V, S4: 91 V; the colour marks the number of hits per second.

right of the image. The region of low sensitivity is the circular area within the round perimeter of the detector where no or very few counts are observed. Furthermore, four hotspots can be seen on the top right edge of the detector. These signals are also visible in background measurements that are conducted with the source turned off. They are therefore not generated by the proton source itself but rather the detector. The background is removed from the signal data before any further analysis.
Lastly, the micro-lensing effect created by the 2250 V difference between the mesh and

MCP-front is also visible in this figure.

The full width at half maximum (FWHM) and mean position of the beam can be determined by integrating over both the x and y direction and then fitting this data with a gaussian curve (red dashed line). This is shown in figure 4.3. According to sim-

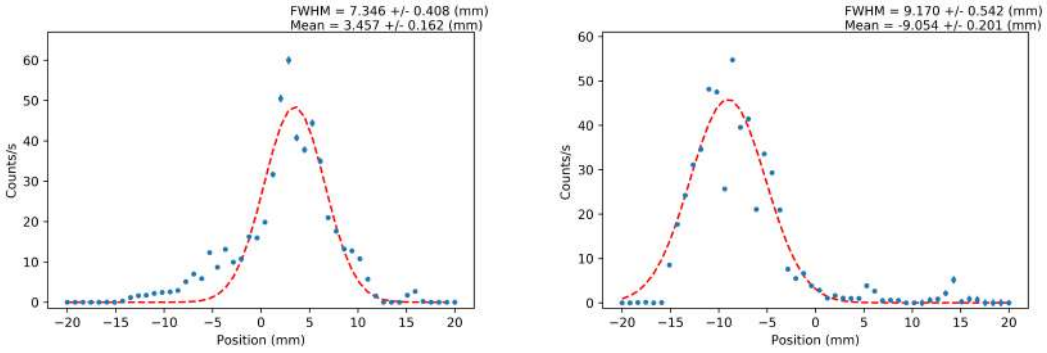

(a) X-direction *(b) Y-direction*

Figure 4.3: Integration over the 2D spectrum in a) x-direction and b) y-direction; the gaussian fit is shown in red

ulation, the ion-beam can be focussed or defocussed by varying the overall extraction ring potential in comparison to the gas cell potential. With the beam steered to the sensitive area of the detector, all of the extraction ring electrode voltages are increased and decreased by the same value. The FWHM of the beamspot for different voltages is shown in figure 4.4a in the x-direction and in 4.4b in the y-direction. They show that with increasing steerer voltages the beam reduces in size. The corresponding counts on the entire detector are depicted in figure 4.5. If the steerer voltage is increased

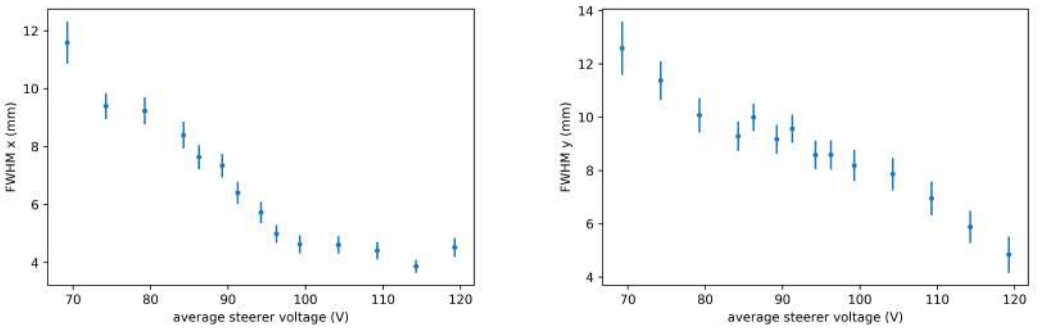

(a) X-direction *(b) Y-direction*

Figure 4.4: FWHM dependent on the average extraction ring potential (e.g. steerer voltages of S1: 90 V*, S2:* 88 V*, S3:* 88 V*, S4:* 91 V *are depicted as* 89.25 V*) in a) x-direction and b) y-direction*

to a value higher than 110 V, the number of ions at the detector start to decrease significantly. This is due to the fact that for this electrical potential, (see figure 4.1) the extraction module is at a higher potential than the gas cell module and the ions are

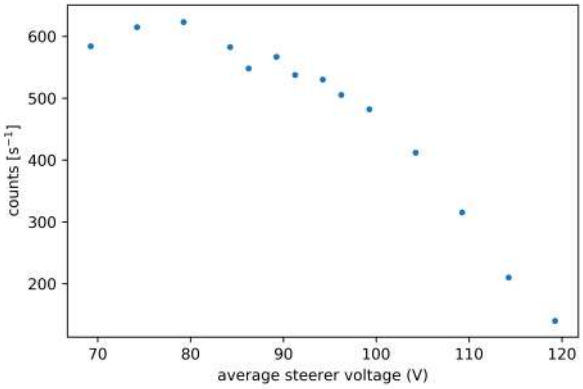

Figure 4.5: Counts per second on the entire detector depended on the average steerer voltages

subsequently 'biased off'.
Additional measurements are performed, examining the effect of the extraction module's entrance and exit electrodes potential. For all of these measurements the steerer voltages are fixed to the same values of: S1: 95 V, S2: 93 V, S3: 93 V, S4: 96 V.
In the first measurement, the extraction entrance potential is varied from −350 V to 0 V. The exit electrode is kept at 0 V. The resulting FWHM of the beam-spot and corresponding ion hits on the detector are shown in figure 4.6. What can be seen in figure 4.6 is, not only that the beam size increases with decreasing extraction entrance voltage, but additionally less ions leave the proton source.
In the measurement where the extraction back electrode is varied from −100 V to 0 V, the exaction front voltage is set to −100 V. Again as is the case for the extraction front electrode, a decrease of the voltage applied to the back electrode also leads to a decreasing number of ions hitting the detector. The corresponding FWHM and counts can be seen in figure 4.7.
Furthermore, it has to be noted that, for both a decreasing extraction front and back voltage, a slight shift of the beam spot towards the centre of the detector can be observed.

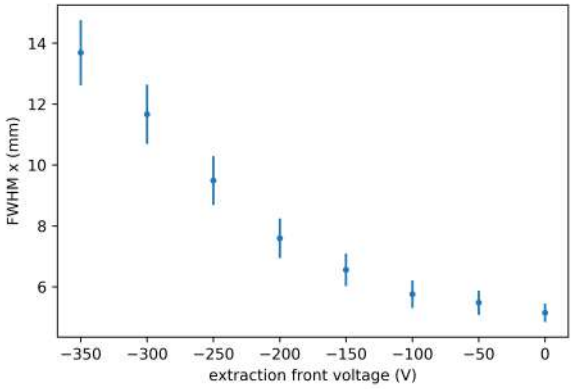

(a) FWHM x-direction

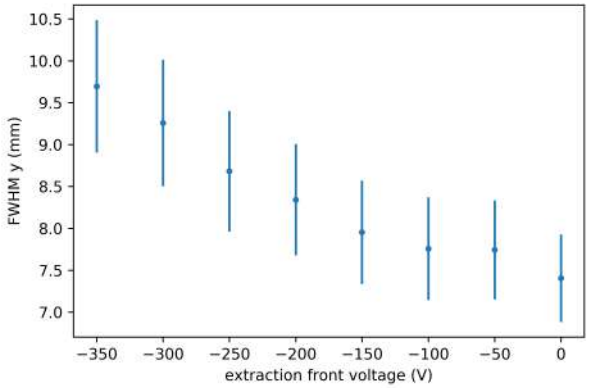

(b) FWHM y-direction

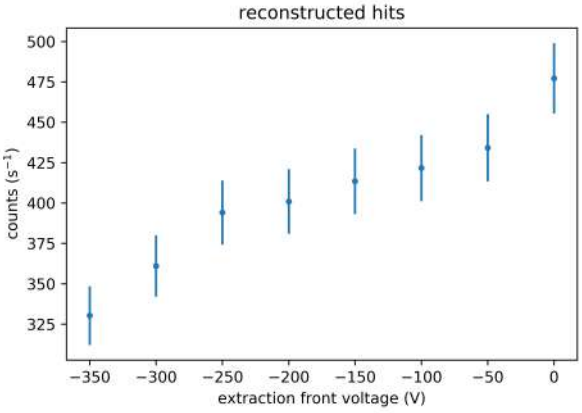

(c) hits per second

Figure 4.6: FWHM of the beam-spot in x and y direction and corresponding hits over the entire detector for a varying extraction front voltage

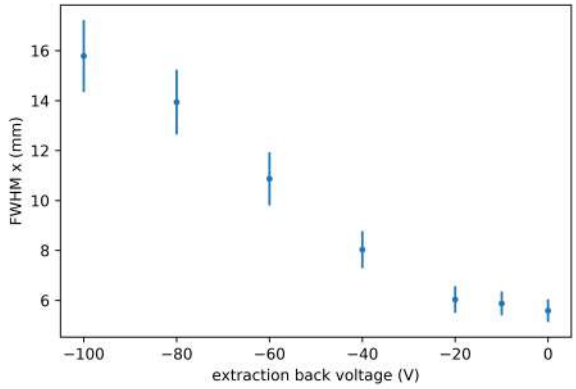

(a) FWHM x-direction

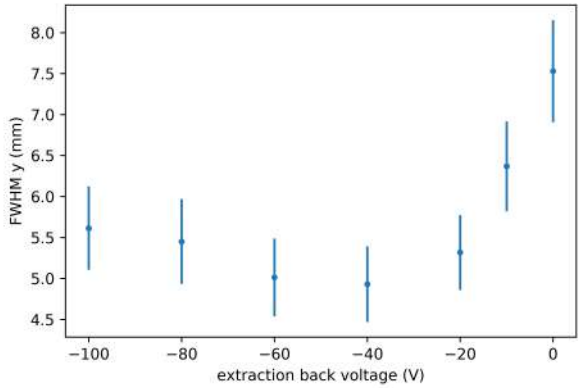

(b) FWHM y-direction

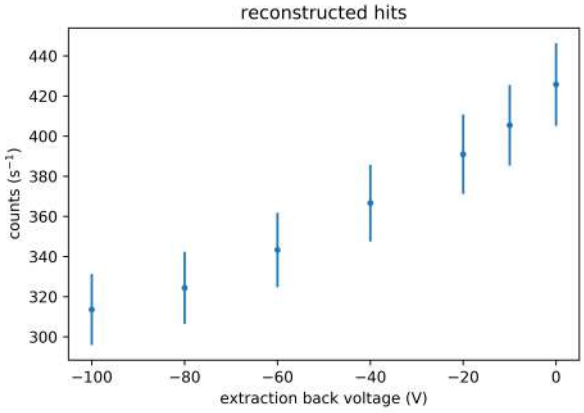

(c) hits per second

Figure 4.7: FWHM of the beam-spot in x and y direction and corresponding reconstructed hits over the entire detector for a varying extraction back voltage

Next, the proton source's capability to move the ion beam, as shown in the simulations in section 3.1.3, was tested. Figure 4.8 shows the ring electrodes of this module and their corresponding numbers. In order to move the ion beam in any direction the

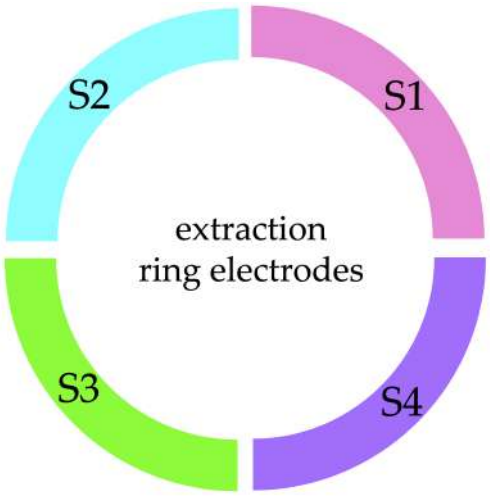

Figure 4.8: Downstream view of the ring electrodes of the extraction module and their corresponding numbers

potentials of the individual electrodes have to be changed. To begin with, the values are set to: S1: 95 V, S2: 93 V, S3: 93 V, S4: 96 V. In order to move the beam on the diagonal from the bottom right of the detector to the top left, the potential of electrodes number S2 and S4 are varied. To move the beam to the top left, the voltage of electrode S2 is decreased by a varying value while the potential of electrode S4 is increased by the same amount. The beam can be steered in the opposite direction by increasing the potential on electrode S2 and decreasing number S4. In figure 4.9 the mean position of the beam in x and y direction is plotted vs. the voltage change. The voltage change is defined as the following: if steerer S2 is reduced by 1 V and steerer S4 is increased by the same value this is plotted as $\Delta V = -2\,\mathrm{V}$ where ΔV is the voltage difference. On the other hand if S2 is increased and S4 reduced by 1 V, this is shown as $\Delta V = 2\,\mathrm{V}$. As can be seen in figure 4.9, the beam does not move in a perfect diagonal line, this is due to the area of low gain on the detector were the beam cannot be measured.

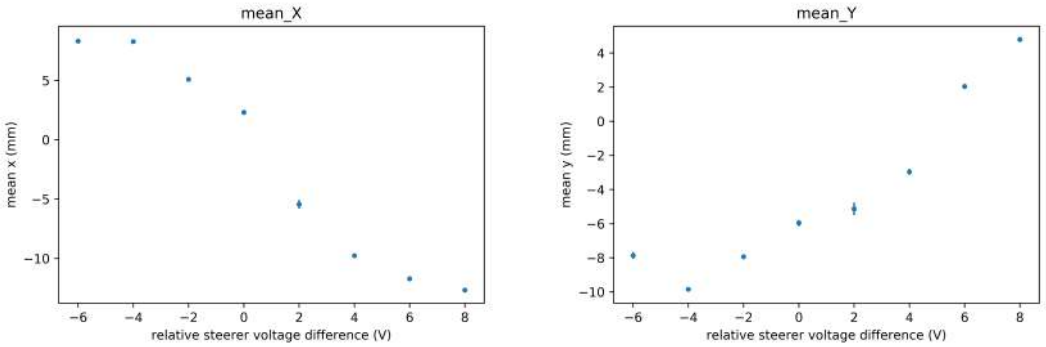

(a) X-direction *(b) Y-direction*

Figure 4.9: Moving of the beam by changing the steerer voltages S2 and S4 relative to the start values of S1: 95 V, *S2:* 93 V, *S3:* 93 V, *S4:* 96 V.

4.2 Pulsed Mode Measurements

To gain further insight into what species of ions are produced in the electron impact ionisation process, the source can be operated in pulsed mode. The potentials used in this mode are shown in figure 4.10. Instead of a continuous potential ramp in the gas

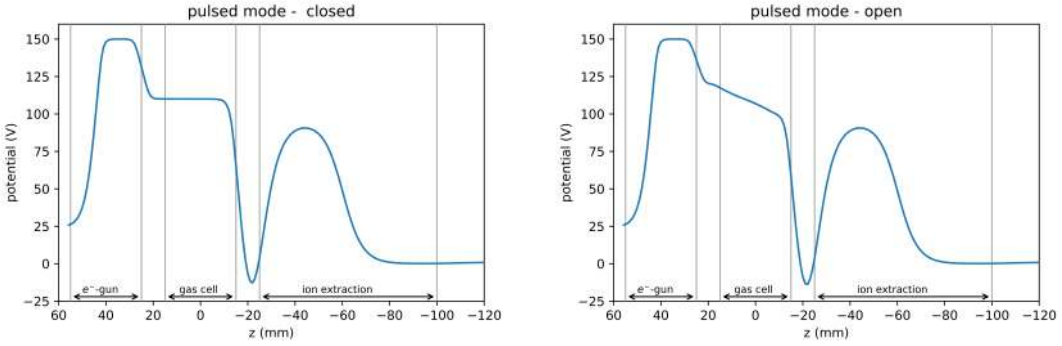

(a) Potential during normal operation *(b) Potential during extraction pulse*

Figure 4.10: Potentials of the protons source in pulsed operation

cell, here the typical potential is flat. (Shown in figure 4.10a: gas cell entrance, ring and exit are all supplied with the same voltage.)
With an adjustable extraction frequency, 10 V is added to the entrance electrode and 10 V is subtracted on the exit electrode. This creates a ramp potential (visible in figure 4.10b) which then pushes the ions out of the gas cell module. Using the timing information from the extraction pulse, a time-of-flight spectrum can be produced. As the different ion-species have different masses, they can be identified as peaks in this spectrum.
Figure 4.11 shows the time-of-flight spectrum of such a measurement. The gas cell is pulsed with a frequency of 1 kHz, the ramp potential is applied for 10 µs. It shows six seperate peaks. Using the energy of the ions and the distance between the centre of the

gas cell electrode and the front side of the detector, these peaks can be assigned masses and therefore ion species using:

$$E = \frac{1}{2}mv^2 \leftrightarrow m = \frac{2Et^2}{d^2} \tag{4.1}$$

where E is the kinetic energy of the ions, m their mass, t the location of the peaks in the time-of-flight spectrum and d the distance between detector and the centre of the gas cell module.
The first peak at $\approx 4.1\,\mu s$ is the proton peak, followed by the expected H_2^+ and H_3^+ peaks at $\approx 5.75\,\mu s$ and $\approx 7.05\,\mu s$. Additionally, peaks for residual gas ions H_2O^+, N_2^+ and O_2^+ can be found at $\approx 17.5\,\mu s$, $\approx 21.6\,\mu s$ and $\approx 22.8\,\mu s$ respectively. This mode is used

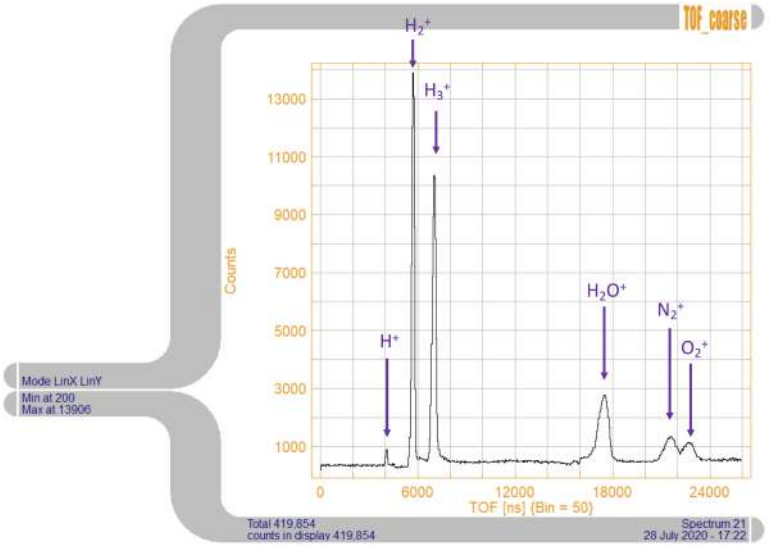

Figure 4.11: Time of flight spectrum for pulsed operation

to optimize the length of the extraction pulse (i.e. the time there is a ramped potential in the gas cell). For this measurement, the pulse length is changed and the number of ions arriving at the detector is monitored. Figure 4.12 shows the corresponding data for protons. The highest H^+ count rate is found at a pulse length of $25\,\mu s$. This value is therefore used in all further measurements.

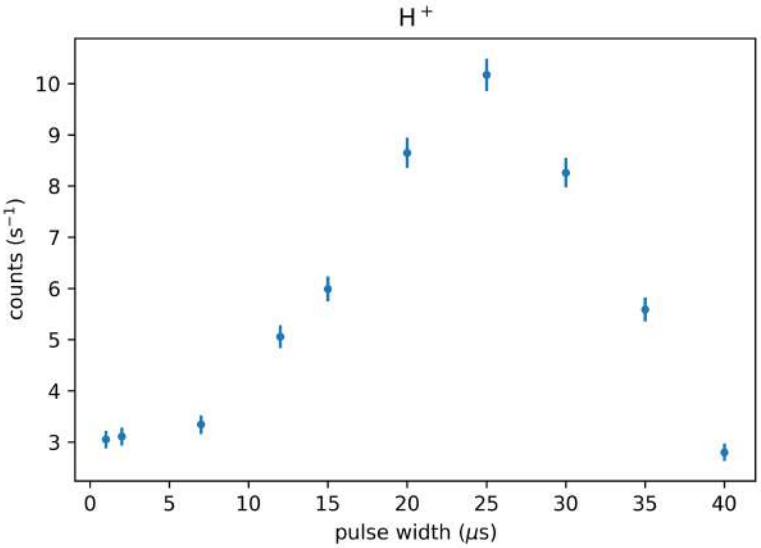

Figure 4.12: Number of protons per second depended on the pulse width of the extraction pulse

4.3 Trapping Mode Measurements

As the potential in pulsed mode operation is either flat, or an extraction ramp, it does not trap ions. In order to do so, a potential well is created. For this, both extraction entrance and exit electrodes of the gas cell are set to a higher potential than the gas cell ring electrode. In figure 4.13a, the ring electrode is supplied with to 110 V whereas entrance and exit electrodes are set to 113 V. The higher the potential difference, the deeper the potential well is.
The extraction pulse in this mode is the same as in the pulsed mode. It increases the gas cell front electrode by 10 V to 123 V and decreases the exit electrode by 10 V to 103 V. Again, a potential ramp is created in the gas cell and the trapped ions can be extracted. The potentials set during the extraction pulse can be found in figure 4.13b. Just like in pulsed operation, the timing of the extraction pulse provides the start time

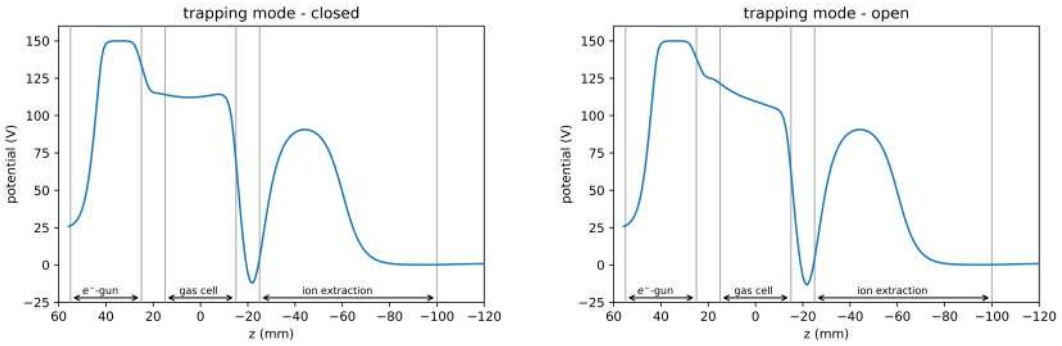

(a) Potential when trap is closed

(b) Potential during extraction pulse

Figure 4.13: Potentials of the protons source in trapping mode operation

for the time of flight spectrum.
Figure 4.14a shows the time-of-flight spectrum for the setting mentioned above. (gas cell (entrance-ring-exit) = (113 V-110 V-113 V)) The ions are extracted with a frequency of 1.25 kHz and the measurement time is 600 s. Figures 4.14b and 4.14c show the spectrum for increased potential well depths generated by 115 V-110 V-115 V and 117 V-110 V-117 V respectively.

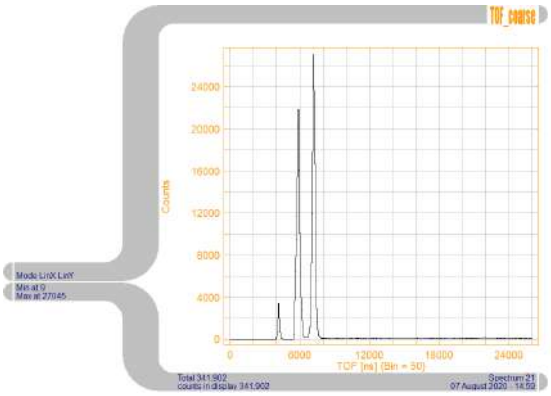

(a) gas cell electrodes: 113 V-110 V-113 V

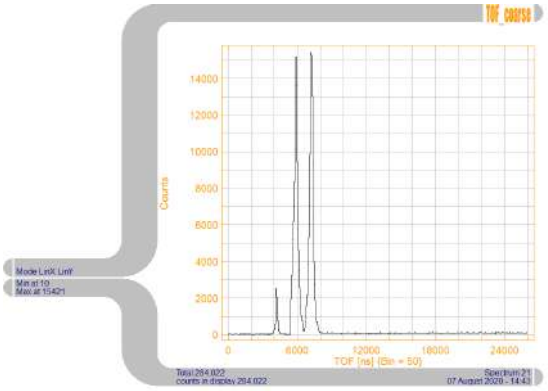

(b) gas cell electrodes: 115 V-110 V-115 V

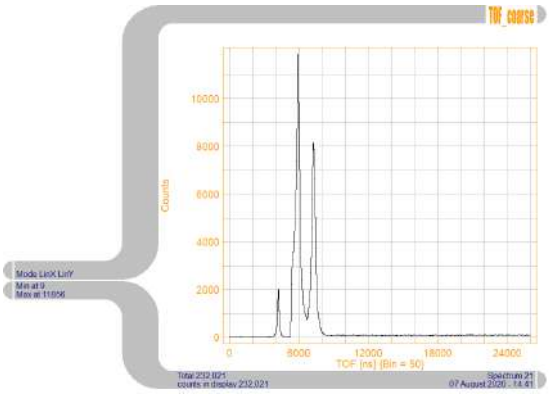

(c) gas cell electrodes: 117 V-110 V-117 V

Figure 4.14: Time of flight spectra for different potential well depths

In this mode, the water, nitrogen and oxygen peaks disappear. This is can be explained by the fact that the magnetic field is not strong enough to trap these heavy

ions. The spectra also show, that with increasing well-depths the ion-peaks get broader. This can be attributed to the fact, that for deeper wells, the energy range of the ions which can be trapped is larger. The energy range contributes to the width of the time-of-flight peaks, as a higher energy ions will travel faster than ones with lower energy.

	3V	5V	7V
H^+	7946 ± 89	6914 ± 83	6113 ± 78
H_2^+	112778 ± 336	97670 ± 313	94611 ± 308
H_3^+	112182 ± 335	86967 ± 295	54562 ± 234

Table 4.1: Number of ion hits per 600 s *on the detector depending on the voltage difference between entrance/exit electrode and the ring electrode of the gas cell*

The corresponding number of detected ions per 600 s are listed in table 4.1. As the proton count is the highest for a voltage difference of 3 V, for all further measurements, unless indicated otherwise, the trapping potential is set to 113 V-110 V-113 V. This setting is additionally useful as the peaks of H_2^+ and H_3^+ don't overlap, and therefore the exact count-rate of these ions can be extracted from the spectrum.

4.3.1 Sideband cooling

As expected, the number of protons extracted from the gas cell trap is lower than both H_2^+ and H_3^+. In order to increase their number, it was predicted that sideband cooling RF could be used.
The sideband cooling pulses are applied as explained in section 3.1.2. Figure 4.15 shows these pulses on an oscilloscope. The different channels, depicted in this figure, supply to the following gas cell ring electrodes:

- Channel 1 (yellow): ring-electrode 1 (0°)
- Channel 2 (green): ring-electrode 2 (180°)
- Channel 3 (orange): ring-electrode 3 (0°)
- Channel 4 (blue): ring-electrode 4 (180°)

First a sideband frequency scan is conducted from 0.1 MHz to 8 MHz in 10000 Hz steps. It is shown in figure 4.16a. The measurement time for each step is 60 s. The amplitude of the applied sideband frequency is 9 V.

A peak of protons can be identified at ≈ 1.07 MHz. Figure 4.16b shows the counts for H^+, H_2^+ and H_3^+ together. Even though the number of protons increases at this frequency, more H_2^+ and H_3^+ are also detected. Dips in the count rate are located at: H^+: ≈ 2.03 MHz, H_2^+: ≈ 0.98 MHz and H_3^+ at ≈ 0.64 MHz.
For more details on the peaks and dips, a second scan is conducted from 0.5 MHz-1.5 MHz in 1000 Hz steps, this time measuring 45 s each step. The extraction frequency

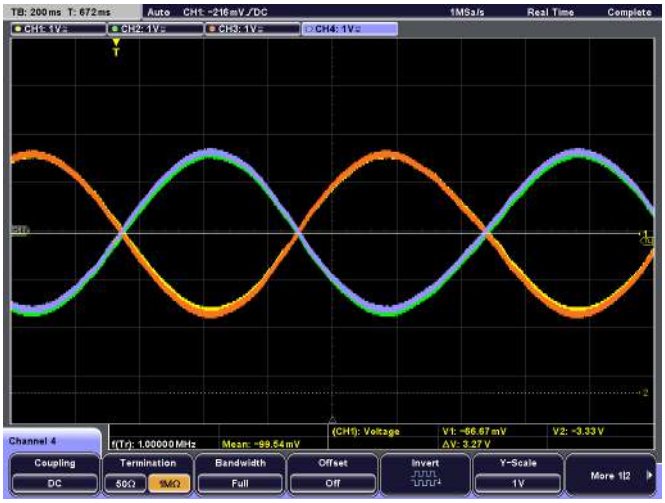

Figure 4.15: Sideband cooling pulses applied to the 4-fold segmented ring electrodes of the gas cell module.

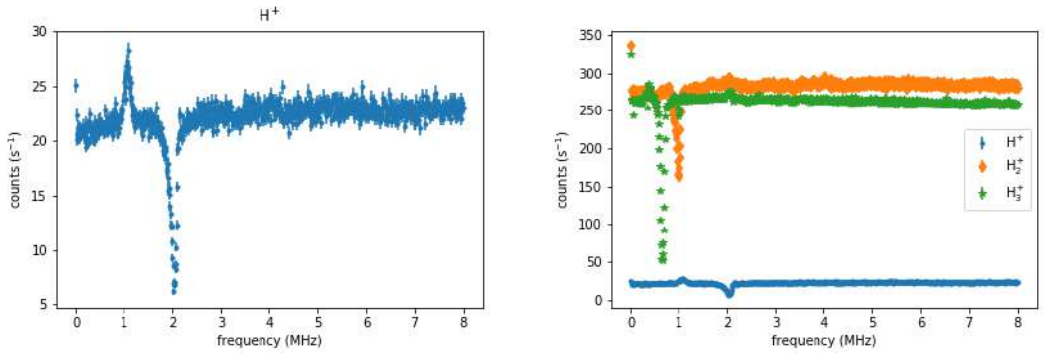

(a) H^+ *(b)* H^+,H_2^+ *and* H_3^+

Figure 4.16: Number of ions detected depended on the sideband frequency at an amplitude of 9 V.

in this scan is set to 1250 Hz. H^+ is shown in figure 4.17a and together with H_2^+ and H_3^+ in 4.17b. It is visible that the proton peak is actually a double peak structure. The frequency of the highest proton count rate is $\approx$ 1.081 MHz and the frequency of the dip in the middle is $\approx$ 1.037 MHz. This feature in the frequency scans can not yet be explained, but also appears at both higher and lower amplitudes. The lowest count rates of H_2^+ and H_3^+ are located at the frequencies $\approx$ 0.98 MHz and $\approx$ 0.636 MHz respectively. Amplitude scans at both 1.037 MHz and 1.081 MHz sideband frequency are conducted from $0 - 20$ V. These can be found in figure 4.18 and 4.19. The number of ions hitting the detector is measured for 60 s each step. The extraction frequency is set to 1250 Hz. At the frequency of the dip (1.037 MHz), it is visible that the H^+ counts increase up to a voltage of 7.5 V and then level of. At the same time the H_2^+ counts steadily decrease whereas the number of H_3^+ stays the same. The same scan at 1.081 MHz shows the same H^+-behaviour, which however is of a lower magnitude. However, in this case both H_2^+, H_3^+ ions decrease with an increasing amplitude. For neither of these settings, is the

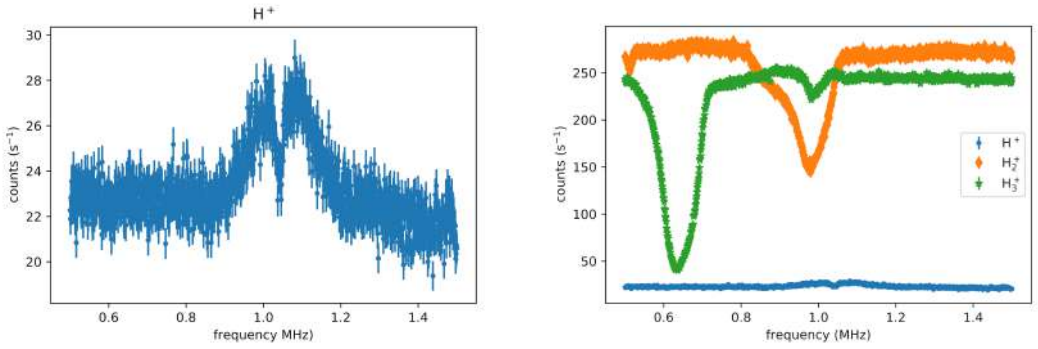

(a) H^+ *(b) H^+,H_2^+ and H_3^+*

Figure 4.17: Number of ions detected depended on the sideband frequency at an amplitude of 9 V.

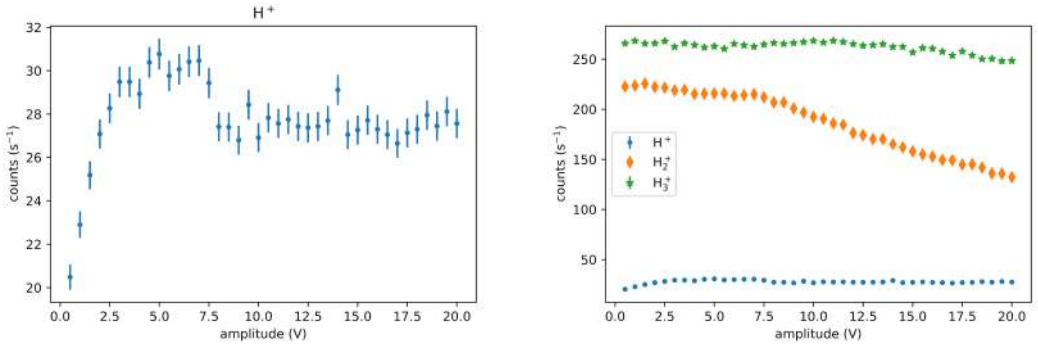

(a) Protons *(b) H^+,H_2^+ and H_3^+*

Figure 4.18: Number of ions detected depended on the sideband amplitude scan at 1.037 MHz.

number of protons delivered by the source higher than either H_2^+ or H_3^+.
Next, the lifetime of the protons in the trap was measured. This can be done by measuring the number of protons leaving the trap for different trapping times. Here, the extraction pulse width of 25 µs is kept constant whereas the extraction frequency is varied. Figure 4.20a shows the count rate of the different ion species depended on the extraction frequency at a sideband frequency of 1.037 MHz. The measurement time for each step is 100 s.
Figure 4.20b shows the same thing, except the trapping time t_{trap} is calculated from the extraction frequency using:

$$t_{trap} = \frac{1 - (f \cdot t_{width})}{f} \tag{4.2}$$

where f is the extraction frequency and t_{width} the pulse width.
The data can be fitted using a 'exponential rise with a limit value' function (equation 4.3), from which the lifetime of the particles τ is extracted.

$$h(t_{trap}) = a \cdot \exp(\tau \cdot t_{trap}) + c \tag{4.3}$$

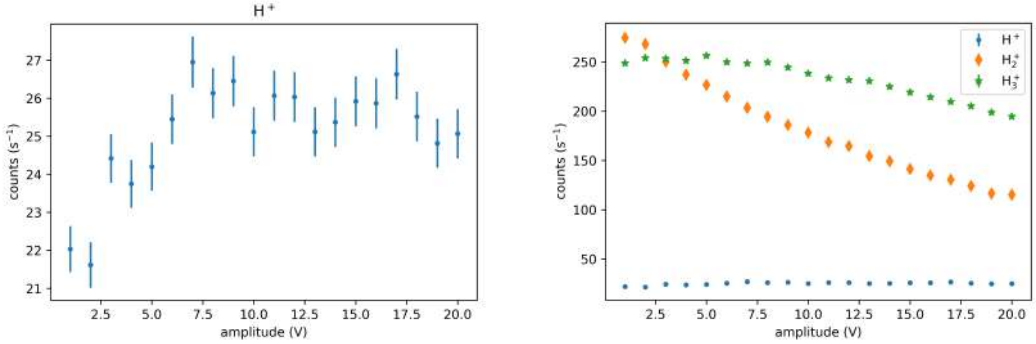

(a) Protons *(b) H^+,H_2^+ and H_3^+*

Figure 4.19: Number of ions detected depended on the sideband amplitude scan at 1.081 MHz.

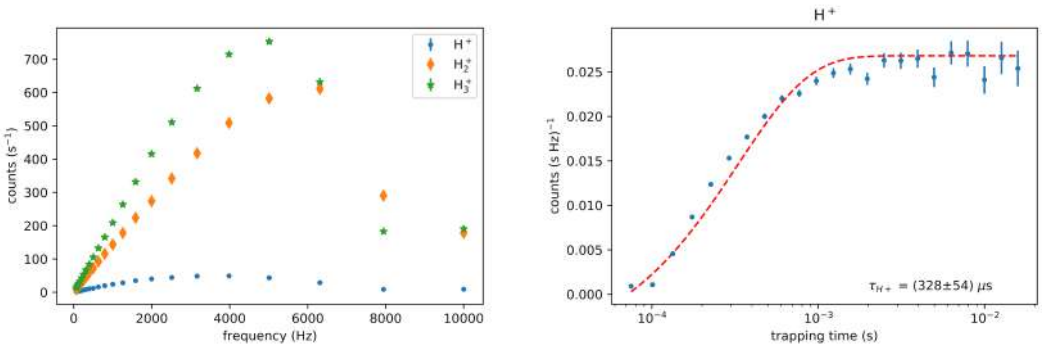

(a) Number of H^+,H_2^+ and H_3^+ depended on the extraction frequency

(b) H^+ depended on the trapping time; the red curve shows the fit mentioned in equation 4.3

Figure 4.20: trapping time scan at a sideband frequency of 1.037 MHz

Figure 4.21 shows the the lifetimes of protons in the gas cell as a function of pressure and sideband frequency voltage. As expected, the lifetime decreases with increasing pressure and the application of sideband cooling pulses leads to a longer lifetime. The highest lifetime $(1649 \pm 299)\,\mu s$ is measured at a pressure of 0.5×10^{-6} mbar and an amplitude of 20 V.

As visible in the frequency scan, even tough the number of protons can be increased using sideband cooling, it is still low in comparison to both H_2^+ and H_3^+.

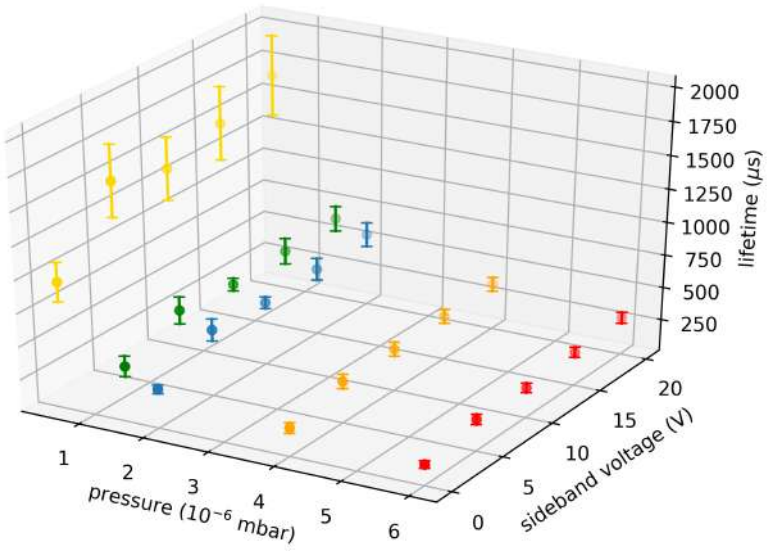

Figure 4.21: Lifetimes of protons in the gas cell trap depended on sideband voltage and pressure at a sideband frequency of 1.037 MHz.

4.3.2 Rotating wall

A rotating electric field can be created by the application of the rotating wall pulses as described in section 3.1.2. Figure 4.22 shows the oscilloscope image of the rotating wall pulses specified below.

- Channel 1 (yellow): ring-electrode 1 (0°)
- Channel 2 (green): ring-electrode 2 (90°)
- Channel 3 (orange): ring-electrode 3 (180°)
- Channel 4 (blue): ring-electrode 4 (270°)

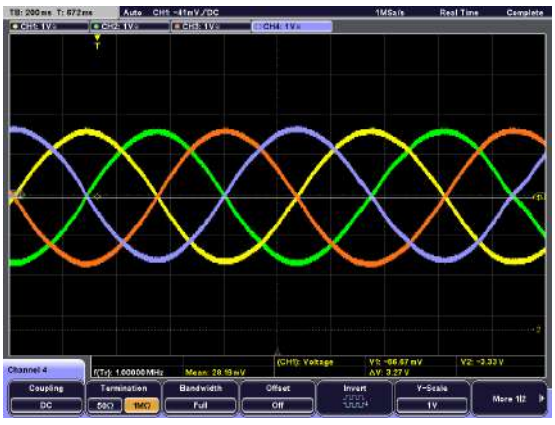

Figure 4.22: Rotating wall pulses applied to the 4-fold segmented ring electrodes of the gas cell module.

As the field can rotate in two directions, this direction will be specified as (90 °, 0 °). These two numbers come from the phase applied to the outputs 1 and 2 of the waveform generator supplying the RF pulses. The reverse direction of the rotation, labelled (0 °, 90 °), is supplied by the following channels and shown in figure 4.23.

- Channel 1 (yellow): ring-electrode 1 (0°)
- Channel 2 (green): ring-electrode 2 (270°)
- Channel 3 (orange): ring-electrode 3 (180°)
- Channel 4 (blue): ring-electrode 4 (90°)

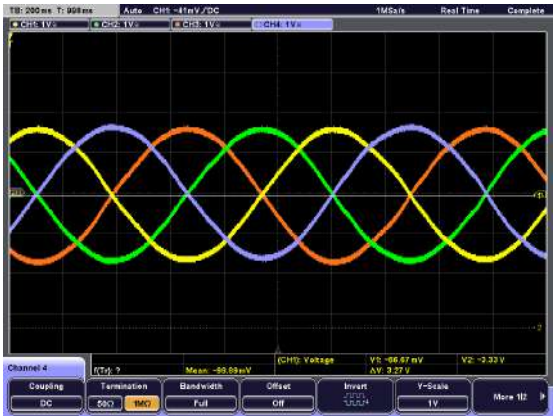

Figure 4.23: Rotating wall pulses applied to the 4-fold segmented ring electrodes of the gas cell module rotating in the opposite direction

rotating wall: (90°, 0°)

As for the sideband cooling method, the rotating wall frequency is scanned from 0.1 − 8 MHz in 10000 Hz steps, measuring the count rate at each step for 60 s. The frequency scan at 10 V for this rotating wall direction can be found in figure 4.24.

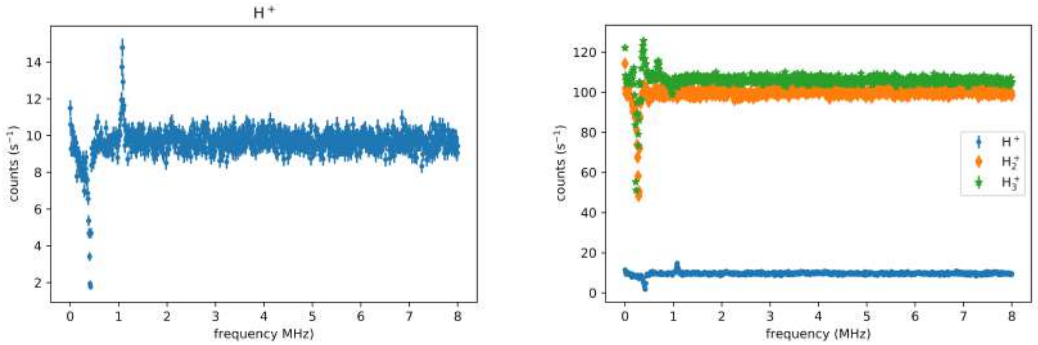

(a) H^+ *(b) H^+, H_2^+ and H_3^+*

Figure 4.24: frequency scan at a rotating wall amplitude of 10 V

In this measurement the extraction frequency is set to 500 Hz. A dip at ≈ 0.42 MHz and a peak ≈ 1.08 MHz in the proton count rate can be identified.
The H_2^+ and H_3^+ rates in figure 4.24b have drops at ≈ 0.28 MHz and ≈ 0.23 MHz respectively. Interestingly a peak in the H_3^+ spectrum is visible at ≈ 0.38 MHz. As was the case for the sideband cooling method, the number of protons detected is lower than H_2^+ and H_3^+.
The amplitude scan at the proton peak frequency (1.08 MHz) is shown in figure 4.25a. Extraction frequency and measurement time per step have the same values as in the

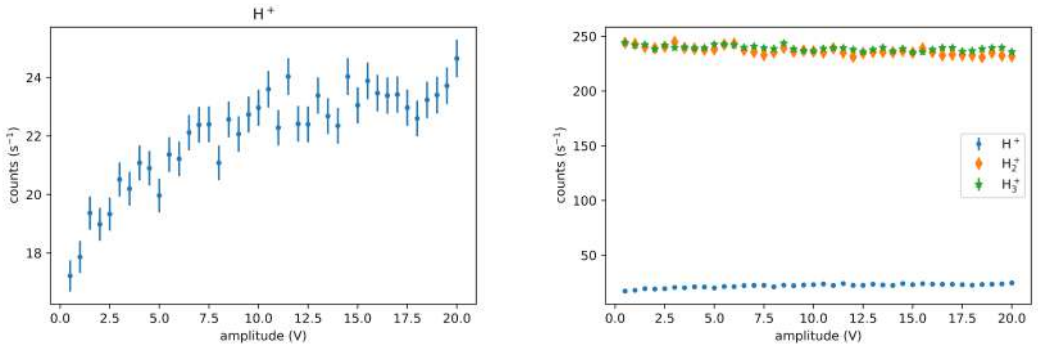

(a) H^+ *(b) H^+, H_2^+ and H_3^+*

Figure 4.25: amplitude scan at a rotating wall frequency of 1.08 MHz

frequency scan mentioned above. It is visible that the proton count rate rises with increasing rotating wall voltage. The levelling off effect of the count rate as seen in the sideband frequency amplitude scan is not observable here. Figure 4.25b shows all three ion species together. For this direction of the rotating wall method, there is no reduction in either H_2^+ nor H_3^+ numbers.
The lifetime measurements for this frequency value, conducted at different pressures and voltages, are shown in figure 4.26. As seen previously, the lifetime decreases with increasing pressure and is improved with the application of rotating wall pulses. The maximum lifetime (1666 ± 273) µs is achieved at a pressure of 0.5×10^{-6} mbar at 10 V rotating wall amplitude.
Again as for the sideband cooling mode, even with the application of rotating wall pulses, the number of H^+ leaving the proton source is one order of magnitude lower than both H_2^+ and H_3^+.

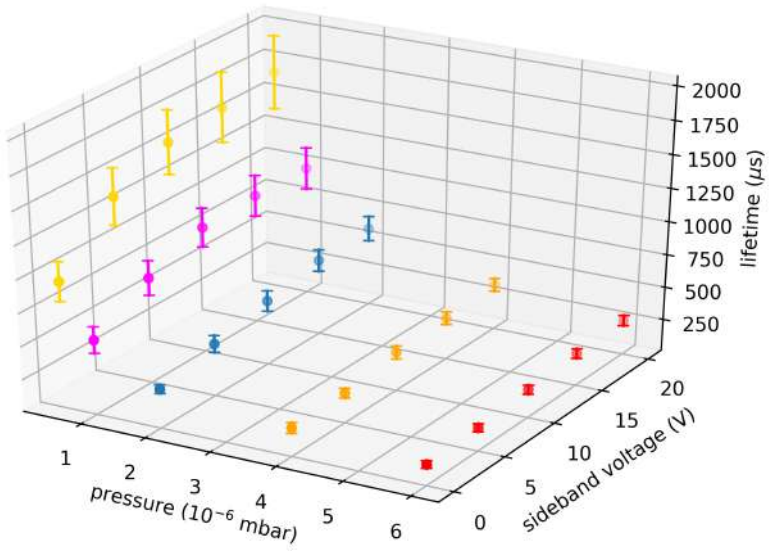

Figure 4.26: Lifetimes of protons in the gas cell trap dependent on rotating wall voltage and pressure at a rotating wall frequency of 1.08 MHz

rotating wall: (0°, 90°)

The measurements described above were repeated for the opposite rotating wall direction. The frequency scan (rotating wall voltage = 10 V, extraction frequency = 500 Hz, measurement time per step = 60 s) is shown in figure 4.27a. There is a proton peak

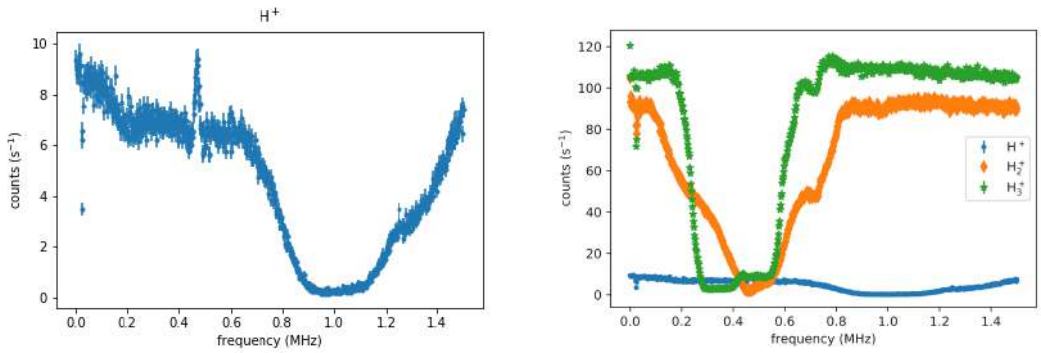

(a) H^+ *(b)* H^+, H_2^+ *and* H_3^+

Figure 4.27: rotating wall frequency scan at 10 V

visible at ≈ 0.47 MHz followed by a drop that reduces the count rate to almost 0. Figure 4.27 shows that both H_2^+ and H_3^+ have similar large dips in the count rate located at lower frequencies than H^+.

It is important to note that, at the location of the H_2^+ and H_3^+ dips, the count rates of each of the ion species are in the same order of magnitude. Additionally it is notable that the size of the large count rate drops is dependent on the rotating wall amplitude applied the electrodes. Figures 4.28, 4.29,4.30 and 4.31 show the frequency scans (extraction frequency = 500 Hz, measurement time per step = 60 s) at different rotating

wall amplitudes.

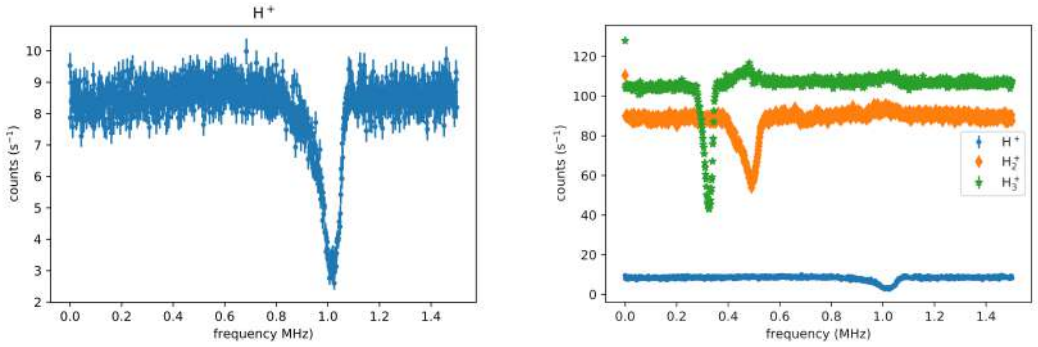

(a) H^+ *(b) H^+, H_2^+, H_3^+*

Figure 4.28: rotating wall frequency scan at 1 V

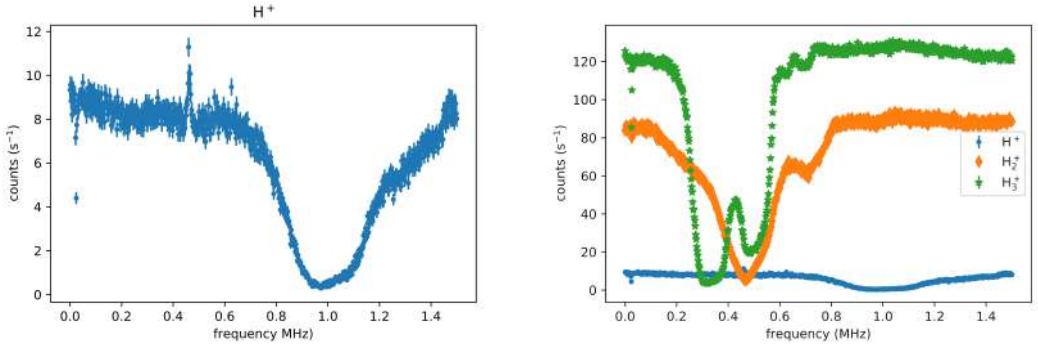

(a) H^+ *(b) H^+, H_2^+, H_3^+*

Figure 4.29: rotating wall frequency scan at 7 V

In the first scan, where only 1 V is applied (figure: 4.28b), the count rate drops in the spectrum are well-defined and located at H^+: ≈ 1.025 MHz , H_2^+: ≈ 0.496 MHz and H_3^+: ≈ 0.326 MHz. The higher the amplitude is raised, the more these dips increase in size. The well defined proton peak at ≈ 0.47 MHz in the proton spectrum is not yet visible at a low amplitude, but appears at 7 V as can be seen in sub-figure 4.29a.
An amplitude scan is conducted at the rotating wall frequency of 0.47 MHz from $0-20$ V in 0.5 V steps. The measurement time and the extraction frequency values are the same as in the frequency scans mentioned above. Figure 4.32a shows that the number of protons is reduced with increasing amplitude. However, more importantly (depicted in figure 4.32b) the rate of both H_2^+ and H_3^+ decreases more strongly than the number of H^+. From ≈ 10.5 V to 20 V, more protons are extracted from the source than either H_2^+ or H_3^+. The biggest difference between the proton and other ion numbers is achieved at ≈ 13.5 V. At this point (444 ± 21) protons, (102 ± 10) H_2^+ and (190 ± 14) H_3^+ are measured per 100 s.
The time-of-flight spectrum at this value is shown in figure 4.33. The proton peak is still narrow and well-defined. Due to the low number of H_2^+ and H_3^+, those peaks are

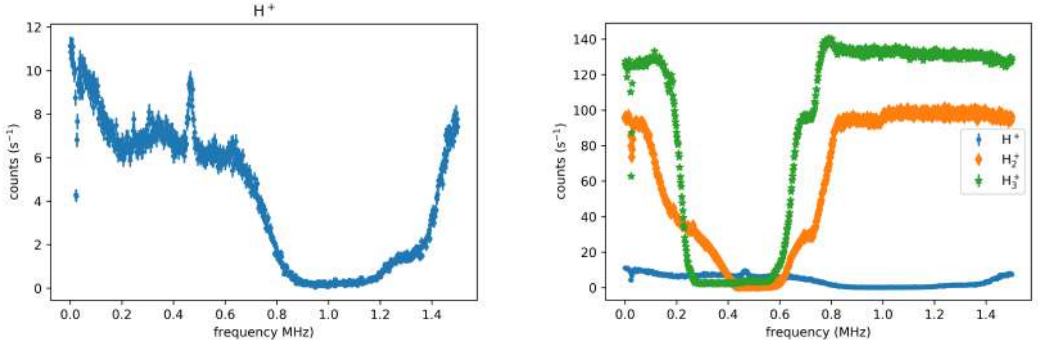

(a) H^+ *(b)* H^+, H_2^+, H_3^+

Figure 4.30: rotating wall frequency scan at 13.5 V

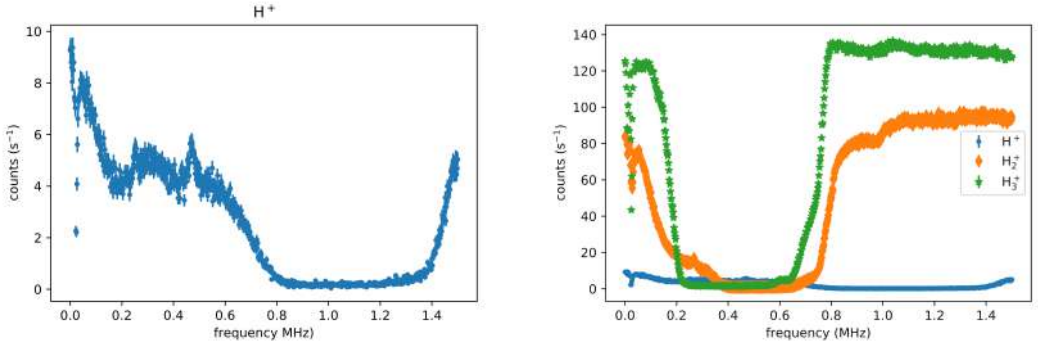

(a) H^+ *(b)* H^+, H_2^+, H_3^+

Figure 4.31: rotating wall frequency scan at 20 V

not clearly visible. However, when looking at a time-of-flight spectrum with a slightly higher or lower frequency than 0.47 MHz, these two peaks appear again. It is important to note that for all frequencies the three peaks are separated. This means that the, well defined and reproducible, peak in the proton number at 0.47 MHz is not created by a possible overlap between the H^+, H_2^+ and H_3^+ peaks. Such a overlap could be created if the energies of H_2^+ and H_3^+ are increased (H_2^+ by ≈ 70 eV, H_3^+ by ≈ 140 eV), which would subsequently lead to a shorter time-of-flight.

As for the cooling methods described above, a lifetime measurement (depicted in figure 4.34) was conducted at different pressures and voltages. Again the proton lifetime is shorter the higher the pressure. It also increases with the amplitude of the rotating wall pulses up to 15 V, before it is reduced again at 20 V. Overall the lifetimes in this mode are shorter than in the two other modes with the highest value being (1518 ± 189) µs achieved at a pressure of 0.5×10^{-6} mbar and a rotating wall amplitude of 10 V.
The count rate in dependence on the extraction frequency (rotating wall frequency = 0.47 MHz, voltage = 13.5 V, p = 0.5×10^{-6} mbar, measurement time per step = 100 s) is shown in figure 4.35.

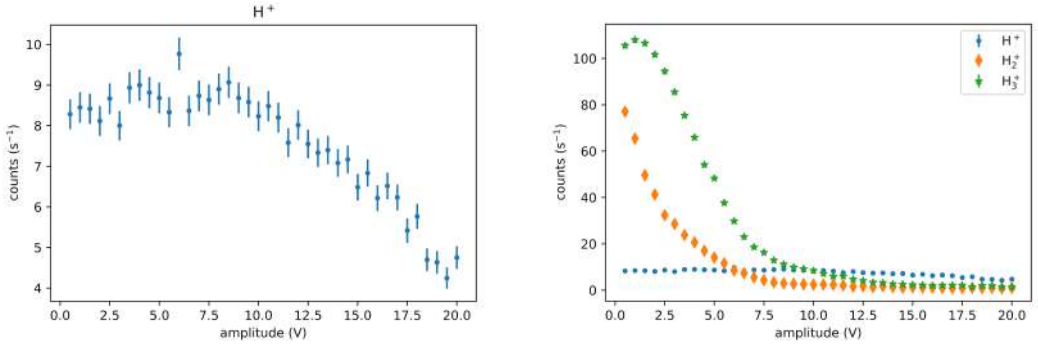

(a) H^+ *(b)* H^+, H_2^+ *and* H_3^+

Figure 4.32: Amplitude scan at a rotating wall frequency of 0.47 MHz

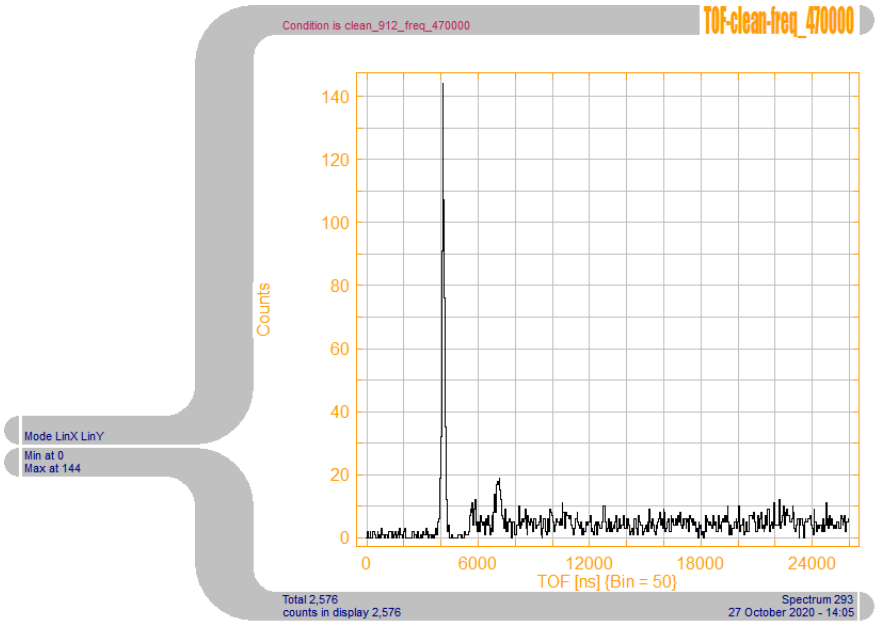

Figure 4.33: Time of flight spectrum with an applied rotating wall frequency of 0.47 MHz *and an amplitude of* 13.5 V

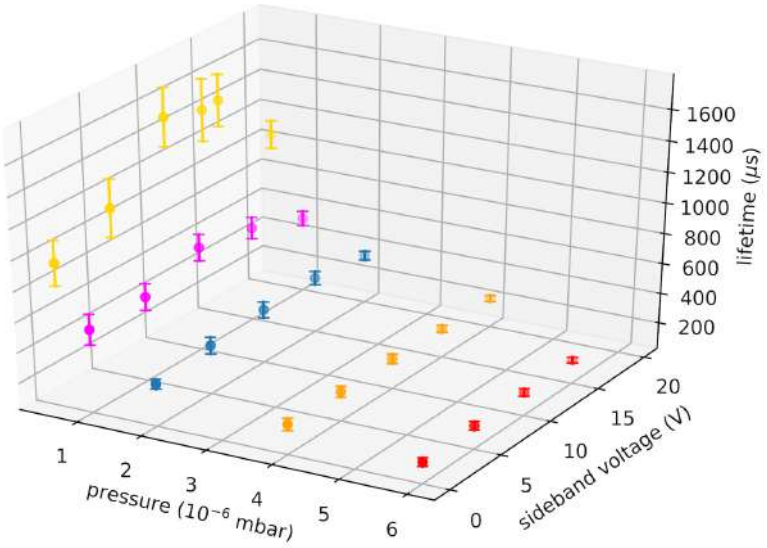

Figure 4.34: Lifetimes of protons in the gas cell trap depended on rotating wall voltage and pressure at a rotating wall frequency of 0.47 MHz

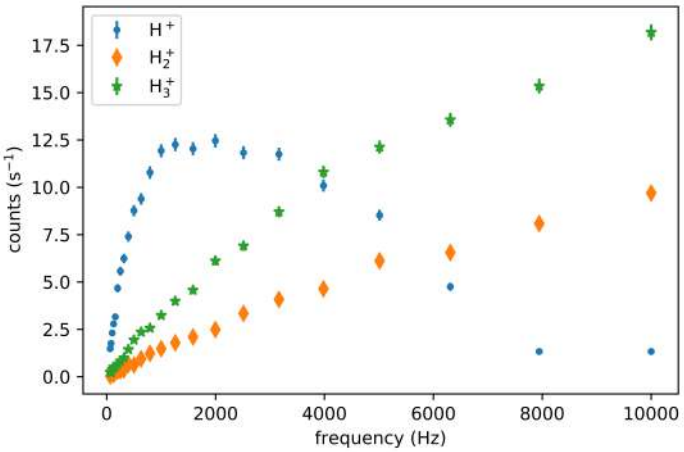

Figure 4.35: Number of extracted ions depended on the extraction frequency

The biggest difference between the number of protons and H_2^+ and H_3^+ ions leaving the source is at a extraction frequency of $\approx 1000\,\text{Hz}$. At this value (1183 ± 34) protons, (334 ± 18) H_2^+ and (691 ± 26) H_3^+ are detected per 100 s.

For all the measurements described in the sideband cooling and rotating wall sections, the housing electrode supplied with 25 V and the gas cell is set to 113 V-110 V-113 V. Therefore the impact energy of the electrons in the gas cell is 85 eV. By changing all potentials of the electrodes in the gas cell and extraction module with respect to the fixed values of the the electron gun (filament = 1.725 A, housing 25 V, anode = 150 V), the electron impact energy can be increased or reduced. Additionally by adjusting these voltages, the ions produced in the gas cell either have a higher or lower energy when leaving the source. Figure 4.36 shows the number of ions per second depending on the electron impact energy. For all these measurements (measurement time per step = 120 s, extraction frequency = 500 Hz), neither sideband nor rotating wall pulses are supplied to the ring electrode.

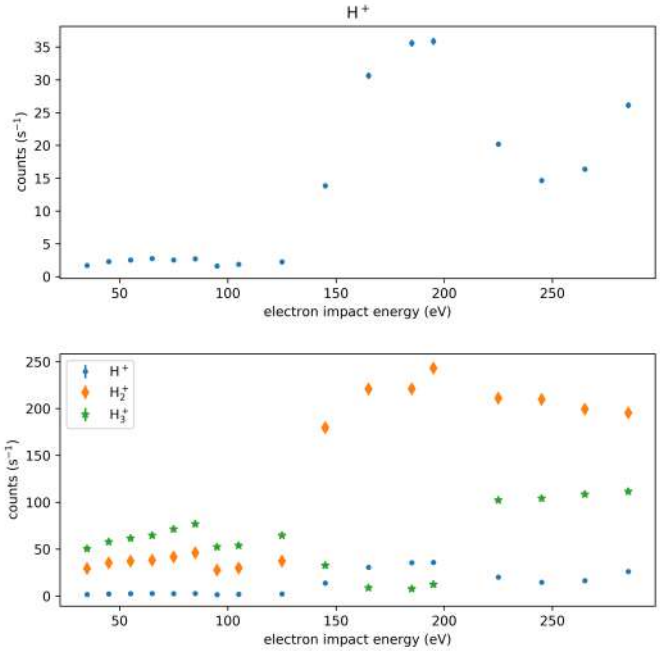

Figure 4.36: Measurements of the number of H^+, H_2^+ and H_3^+ at different electron impact energies

However, the data from this cross section measurement does not agree with the cross section measurement mentioned in section 2.1. Instead of having a peak at 95 eV, the count rate increases slowly up to $\approx 125\,\text{eV}$, then increases by one order of magnitude at $\approx 150\,\text{eV}$, drops down at $\approx 250\,\text{eV}$ and then increases again for higher energies. It is therefore assumed that the number of protons generated by the proton source is not

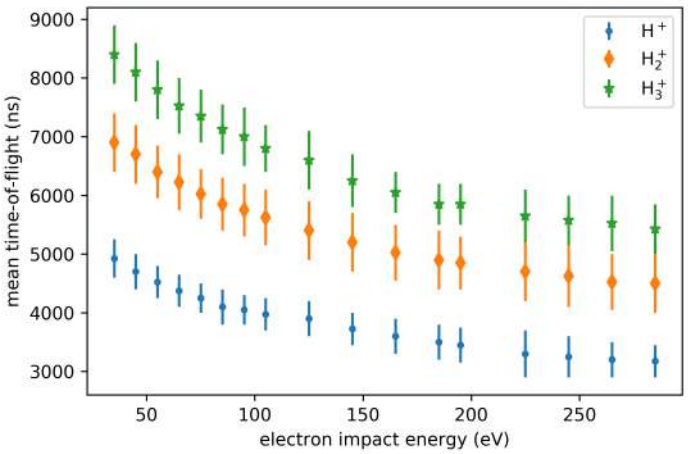

Figure 4.37: Time-of-flight of H^+, H_2^+ and H_3^+ at different electron impact energies

limited by the cross section but rather by transport effects. At present, this assumption is being investigated by SIMION simulations. In figure 4.37 the mean time-of flight for H^+, H_2^+ and H_3^+ is plotted. The flight time behaves as expected and decreases with increasing energy of the ions.
With $(35.87 \pm 0.55\,\text{counts/s})$, 195 eV is the electron impact energy where the highest number of protons is detected.

Chapter 5

Conclusion and Outlook

The aim of this master thesis was to construct and characterise a proton source for ASACUSA's matter mixing experiments. The working principle of the source consisting of the electron gun, gas cell and ion extraction module was first simulated and then tested in several measurements. Firstly, chapter 4.1 shows that the ion beam generated in the electron impact ionisation process can be both focussed and moved. The different ions produced in the gas cell were identified using either pulsed or trapped mode, by using time of flight spectroscopy. As shown in section 4.2, in pulsed mode the expected ion species H^+, H_2^+ and H_3^+, as well as residual gas ions H_2O^+, N_2^+, O_2^+ are generated and extracted by the source. In trapped mode, only H^+, H_2^+ and H_3^+ are registered at the detector. However, as expected from the H_2 ionisation cross section, the number of protons produced is approximately one order of magnitude lower than the H_2-ions generated. Additionally, as H_2-gas acts as buffer gas, the magnetron motion of the ions produced becomes unstable, and the particles are lost in the trap. Therefore two different stabilization methods were used to increase the number of protons generated by the source.

The sideband cooling method is used to selectively stabilise the proton motion. As can be seen in the measurement results in 4.3.1, the number of protons does increase and both H_2^+ and H_3^+ are reduced, nevertheless, in this mode, the source still generates less protons than other ions.

The rotating wall method uses a rotating electric field which can be applied in two directions. For this method, direction (90 °, 0 °) showed a increase of the number of protons at 1.08 MHz, however no reduction in neither H_2^+ or H_3^+ numbers was visible at that frequency. In the other direction (0 °, 90 °), however, a proton peak forms at 0.47 MHz, a frequency where both H_2^+ and H_3^+ are driven out of the trap. At rotating wall amplitudes of ≈ 10 V and above, more protons are extracted from the source than other ions.

The frequencies of the peaks and dips in each of the methods are summarised in table 5.1. The highest number of protons is extracted at an electron impact energy of 195 eV. However, the number of protons (≈ 35 /s) extracted in this mode is still very low for the

	sideband cooling		rotating wall (90 °, 0 °)		rotating wall (0 °, 90 °)	
	dips	peaks	dips	peaks	dips	peaks
H^+	1.037	1.004 / 1.081	0.42	1.08	1.025	0.47
H_2^+	0.98	-	0.28	-	0.326	-
H_3^+	0.636 / 0.98	-	0.23	0.38	0.496	-

Table 5.1: Approximate frequencies (MHz) of peaks and dips observed for sideband and rotating wall pulses

Cusp trap which usually receives $\approx 10^5$ anti-protons from the MUSHASHI-trap. One of the reasons for this very low number, is the fact that the filament in the electron gun was operated at a very low current of 1.725 A, even-though the operating current of the filament used is ≈ 2.1 A.

This was done to ensure the number of ions generated by the source is kept low in order to not damage the detector. Two measurements with increased electron gun currents of 1.8 A and 1.81 A were conducted at a electron impact energy of 85 eV, with rotating wall pulses applied in the (0 °, 90 °)-direction at 0.47 MHz and 13.5 V. Table 5.2 shows the optimal extraction frequency and the number of ions produced for the different filament currents. Additionally, to gain an insight over how many electrons are generated by the

filament current	1.725 A	1.8 A	1.81 A
optimal extraction frequency	1000 Hz	1995 Hz	2512 Hz
H^+	(1183 ± 34)	(18728 ± 137)	(26810 ± 164)
H_2^+	(334 ± 18)	(3599 ± 56)	(4215 ± 67)
H_3^+	(691 ± 26)	(6982 ± 84)	(6874 ± 83)

Table 5.2: Number of counts per 100 s *for different filament currents; the optimal extraction frequency is defined as the frequency where the difference between H^+ and H_2^+ & H_3^+ is maximal*

filament, the current on the anode was measured for different filament currents. This was done by measuring the voltage drop across three resistors (100 kΩ, 1 MΩ, 10 MΩ) and then calculating the current using $I = \frac{U}{R}$. Figure 5.1 shows this measurement. The current on the anode increases exponentially with the applied current on the filament. Using the measured number of protons for different filament currents and the fact that the current on the anode increases exponentially it can be estimated that at 2.1 A and the gas cell setting mentioned above, approximately 180000 H^+, 35400 H_2^+ and 67000 H_3^+ are generated by the source per second. At this filament current and using 195 eV electron impact energy, the source is estimated to emit approximately 2 million protons and half a million H_2 and H_3 ions per second.

Using these operational settings, a large enough number of protons can be generated and hence, the source is therefore ready for for transport to CERN, where it will be

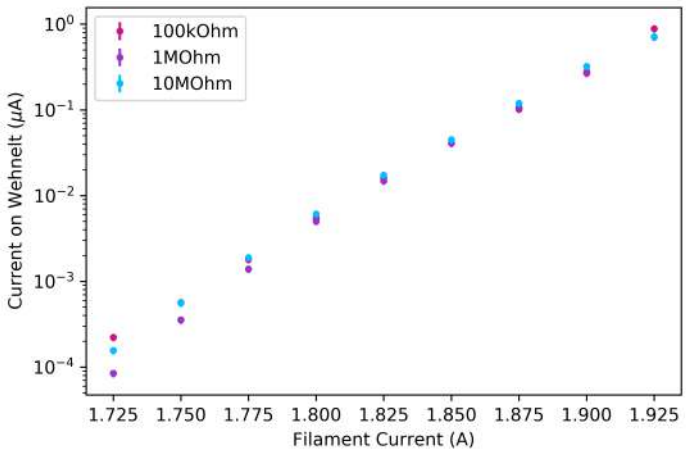

Figure 5.1: Current on the anode dependent on different filament currents

integrated into the ASACUSA experiment.

The origin for the several peaks and dips found in the frequency scans is not yet fully understood. As mentioned in section 3.1.2, the calculated cyclotron frequency of protons (from the magnetic field in the simulations) is 1.1 MHz. Figure 5.2a shows this frequency as a red line in the sideband frequency scan. Figure 5.2b shows the same thing except in the rotating wall frequency scan (direction: (90 °, 0 °)). The second sideband peak (≈ 1.081 MHz) and the rotating wall peak (≈ 1.08 MHz) are not only located at approximately the same frequency, but they are also relatively close to the simulated cyclotron frequency. No other peaks or dips in the frequency scans are located close to

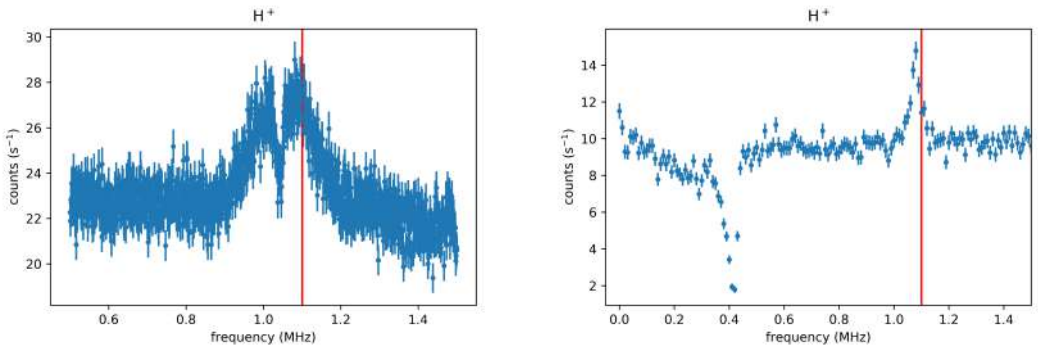

(a) sideband frequency scan *(b) rotating wall (90 °, 0 °) frequency scan*

Figure 5.2: Comparisons of peaks in the frequency scans with the calculated cyclotron frequency (red line)

this frequency. Neither H_2^+- nor H_3^+-peaks are visible in the sideband frequency scan, however in the rotating wall scan a H_3-peak is visible at ≈ 0.38 MHz. The calculated cyclotron frequency for H_3^+ is ≈ 0.367 MHz.

In order to gain more insight into the situation and especially to understand the proton peak at ≈ 0.47 MHz, simulations of the gas cell trap with protons, H_2^+ and H_3^+

ions and rotating wall pulses will be conducted. Additionally, further measurements, including the determination of the ion's energy distribution can be carried out at CERN.

The MCP-detector used for the characterisation measurements will act as the H*-detector in ASACUSA's matter mixing experiments. However, as mentioned in section 3.3, the MCP-plates developed an area of lower sensitivity during their operation. Because this area could not be removed completely, they will be replaced by new ones, before the detector is integrated into the ASACUSA-apparatus.

Appendix A

Acronyms

AD Antiproton Decelerator

ASACUSA Atomic Spectroscopy And Collisions Using Slow Antiprotons

BNC Bayonet Neill-Concelman

CCD charge-coupled device

CEM continuous channel electron multiplier

CERN European Organisation for Nuclear Research

CMOS complementary metal-oxide-semiconductor

DLD delay line detector

FWHM full width at half maximum

HV High Voltage

LHC Large Hadron Collider

LS2 Long Shutdown 2

MCP Microchannel plate

OFHC oxygen-free high thermal conductivity

PMT photomultiplier tube

POM Polyoxymethylene

RF radiofrequency

SHV safe high voltage

SM Standard Model of Particle Physics

SME Standard Model Extension

TDC Time-to-Digital-Converter

Appendix B

Electronic Connection Diagrams

This appendix shows the diagrams of the electronic connections necessary to operate the proton source and detector.

B.1 Proton Source

The connections for the electron gun are shown in green in figure B.1. The gas cell connections (pink) are depicted in three figures:

1. entrance and exit electrode: B.2
2. ring electrode with sideband cooling B.3
3. ring electrode with rotating wall pulses B.4

The connections for the extraction module are shown in orange in diagram B.5.

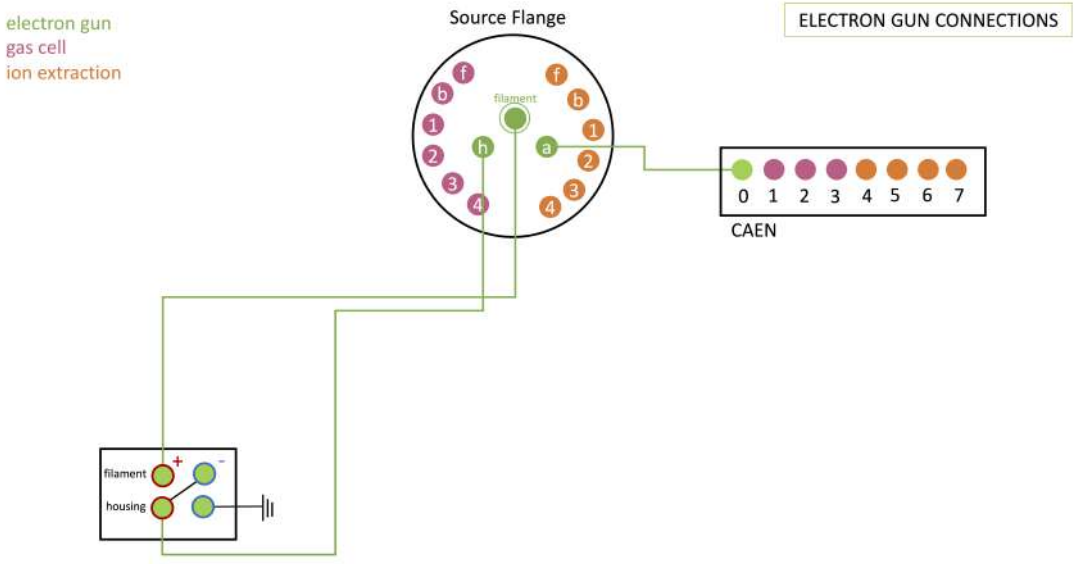

Figure B.1: electronic connections of the electron gun module

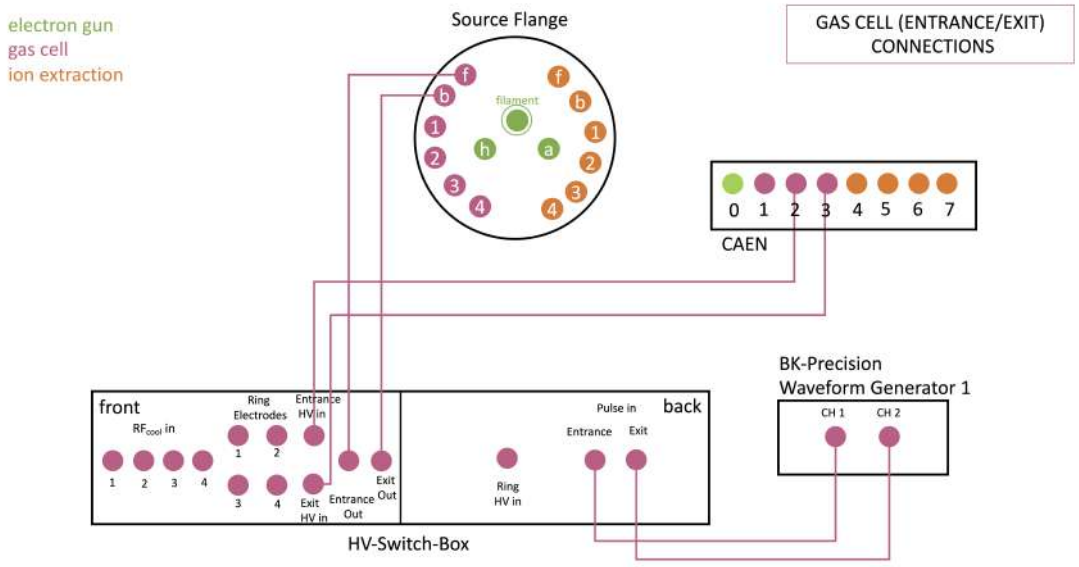

Figure B.2: electronic connections of the gas cell module (entrance and exit electrodes)

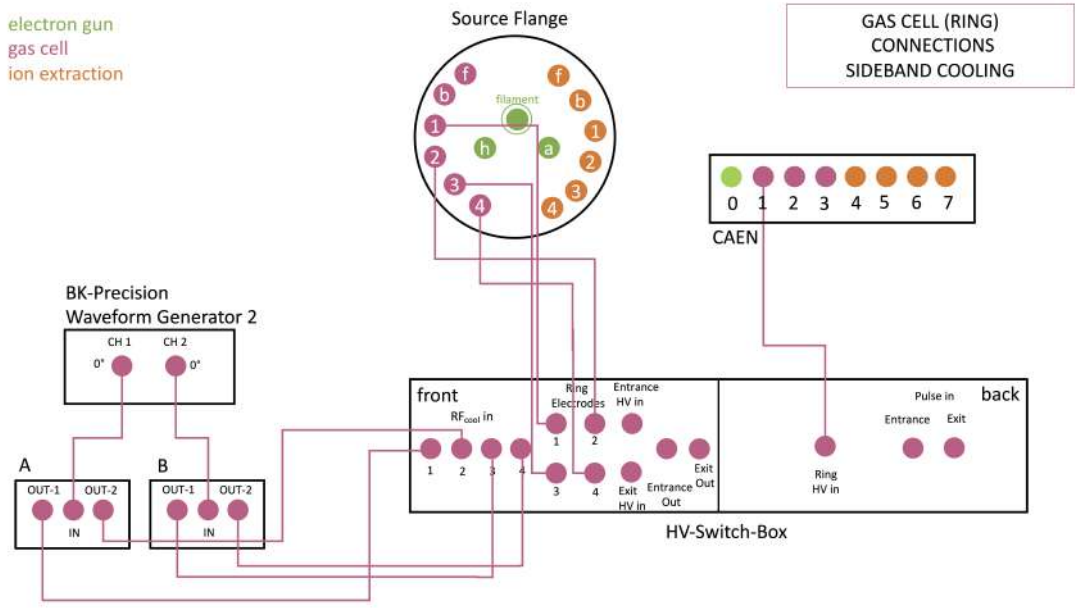

Figure B.3: electronic connections of the gas cell module (ring electrodes with sideband cooling)

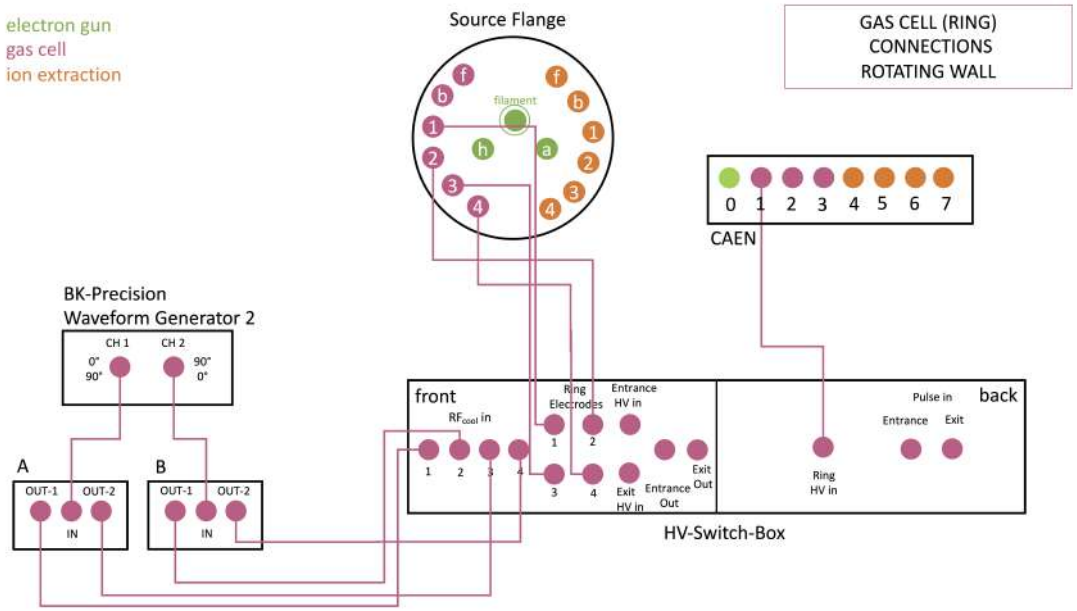

Figure B.4: electronic connections of the gas cell module (ring electrodes with rotating wall pulses)

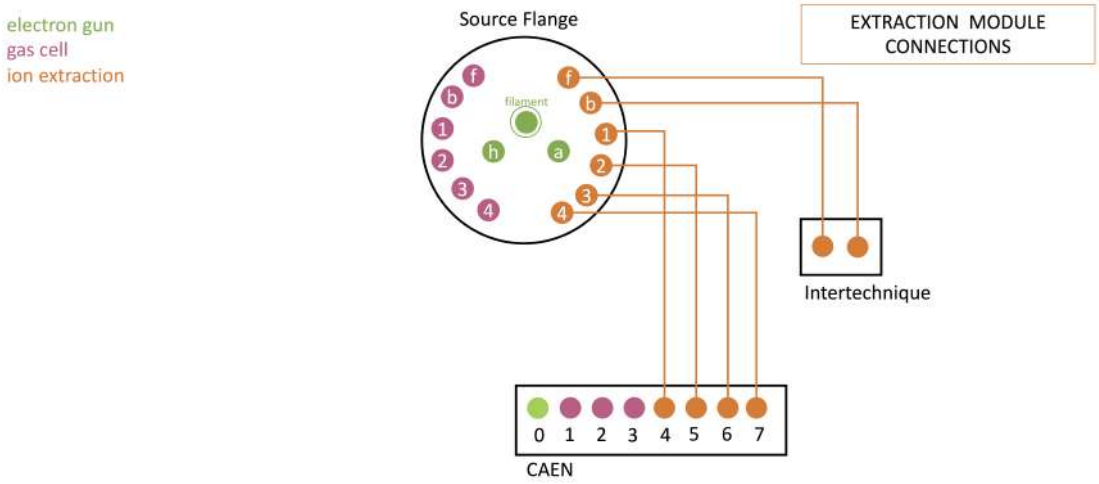

Figure B.5: electronic connections of the extraction module

B.2 Detector

The electronic connections for the detector are also shown in several diagrams: Figure B.6 shows the connections necessary to apply the potentials on the detector.

Signal processing connections are shown in two separate figures:

1. MCP & gas cell extraction pulse: B.7
2. anode wires: B.8

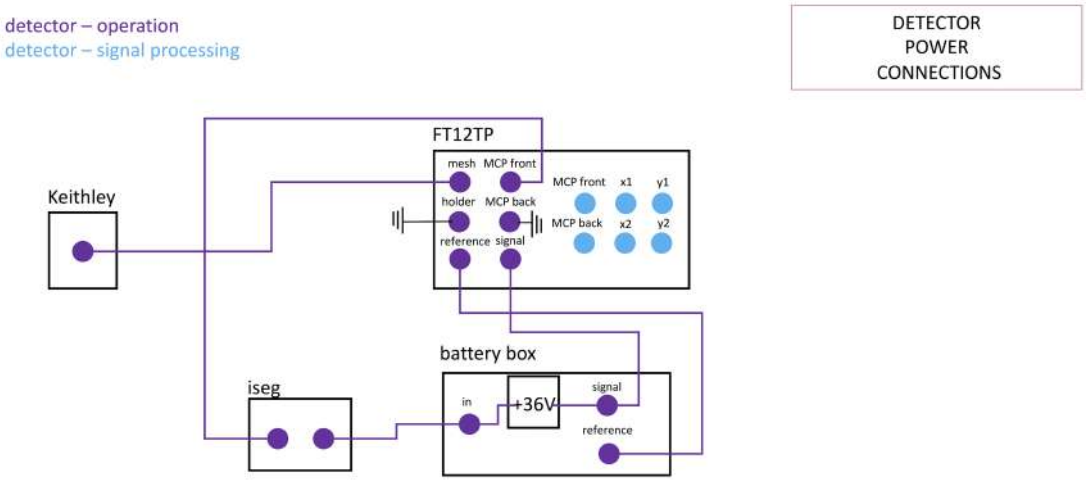

Figure B.6: electronic connections necessary to operate the detector

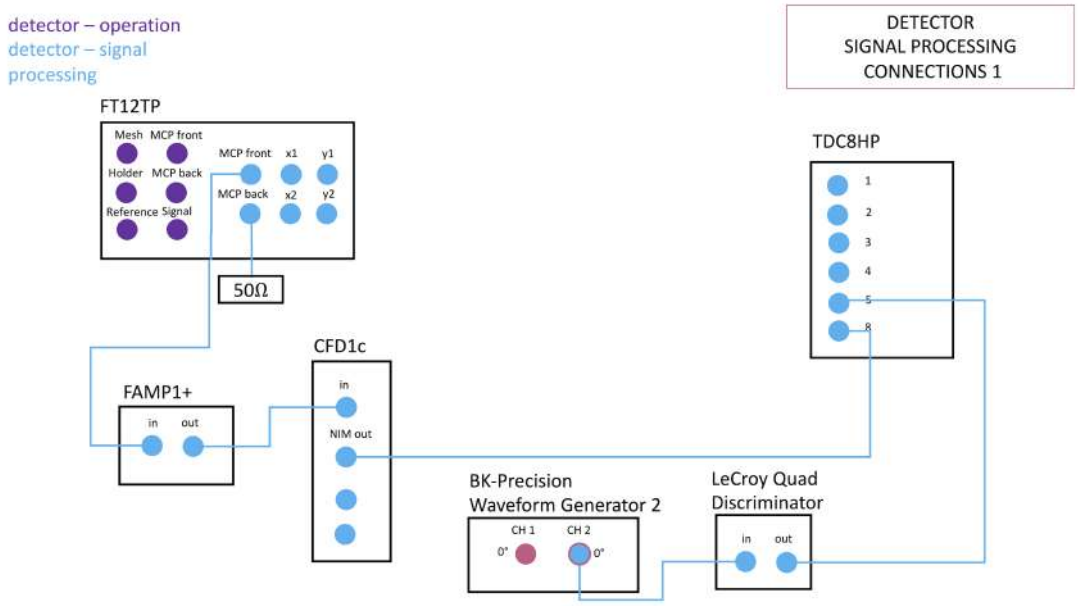

Figure B.7: signal processing: MCP & extraction pulse

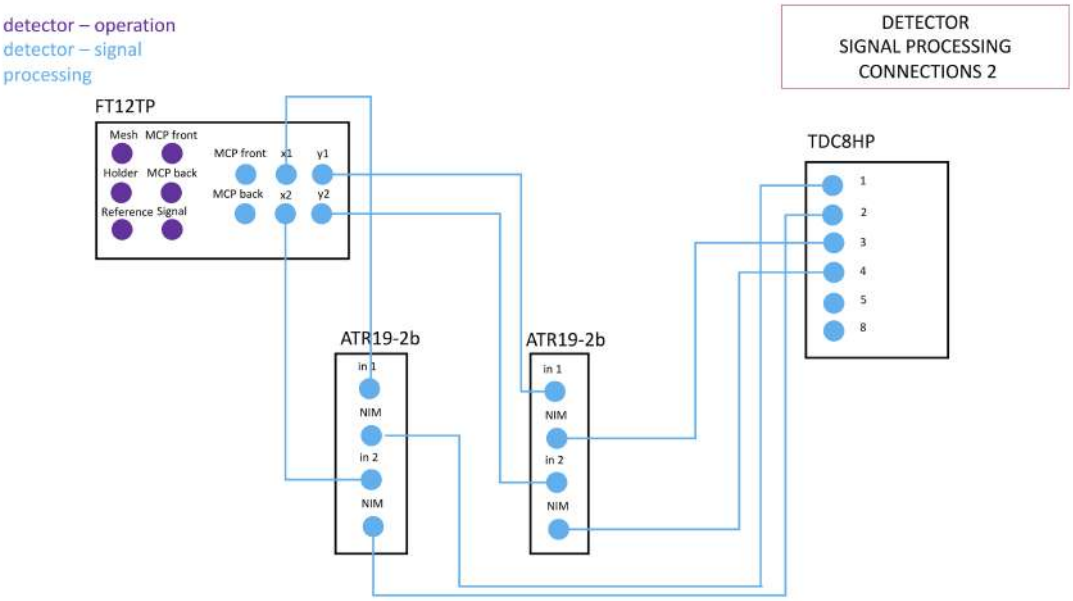

Figure B.8: signal processing: anode wires

Appendix C

Circuit Diagrams

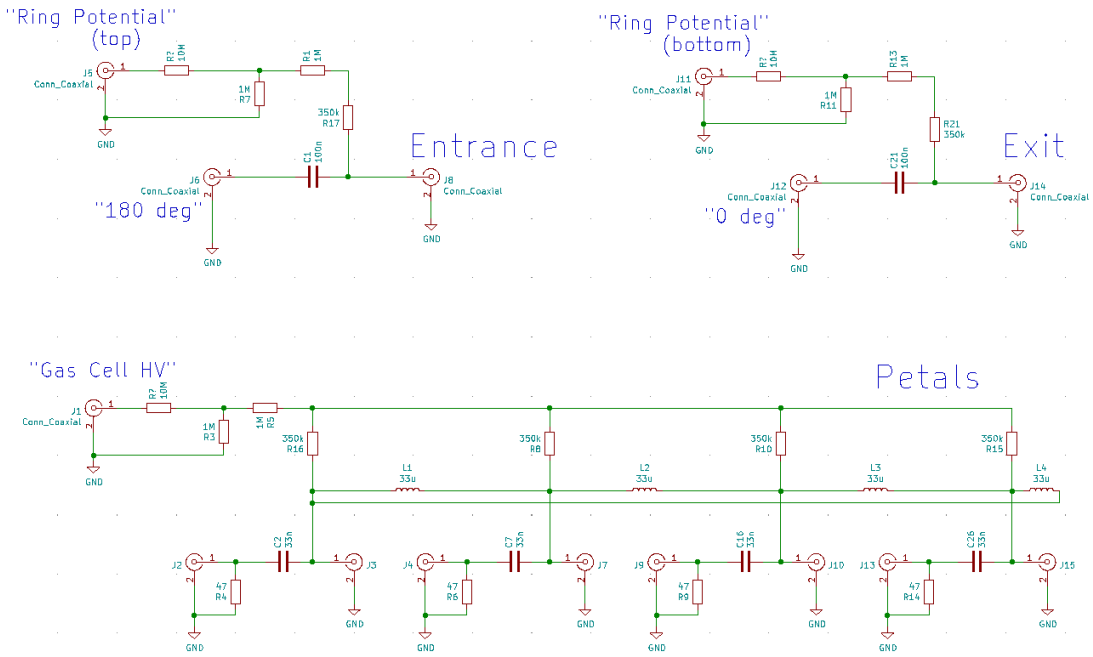

Figure C.1: Circuit diagram of the RF-coupling-box

Bibliography

[1] P. A. M. Dirac and R. H. Fowler, "The quantum theory of the electron," *Proceedings of the Royal Society of London. Series A, Containing Papers of a Mathematical and Physical Character*, vol. 117, no. 778, pp. 610–624, 1928. [Online]. Available: https://royalsocietypublishing.org/doi/abs/10.1098/rspa.1928.0023

[2] M. Charlton and J. W. Humberston, *Positron Physics*, ser. Cambridge Monographs on Atomic, Molecular and Chemical Physics. Cambridge University Press, 2000.

[3] A. Dolgov, "Cosmological matter-antimatter asymmetry and antimatter in the universe," 2002. [Online]. Available: https://arxiv.org/pdf/hep-ph/0211260.pdf

[4] P. A. M. Dirac, "Theory of electrons and positrons," 1933, Nobel Lecture. [Online]. Available: https://www.nobelprize.org/uploads/2018/06/dirac-lecture.pdf

[5] A. G. Cohen, A. D. Rújula, and S. L. Glashow, "A matter-antimatter universe?" *The Astrophysical Journal*, vol. 495, no. 2, pp. 539–549, mar 1998. [Online]. Available: https://doi.org/10.1086%2F305328

[6] J. Alcaraz, D. Alvisi, B. Alpat, G. Ambrosi, H. Anderhub, L. Ao, A. Arefiev, P. Azzarello, E. Babucci, L. Baldini, M. Basile, D. Barancourt, F. Barao, G. Barbier, G. Barreira, R. Battiston, R. Becker, U. Becker, L. Bellagamba, P. Béné, J. Berdugo, P. Berges, B. Bertucci, A. Biland, S. Bizzaglia, S. Blasko, G. Boella, M. Bourquin, G. Bruni, M. Buenerd, J. Burger, W. Burger, X. Cai, R. Cavalletti, C. Camps, P. Cannarsa, M. Capell, D. Casadei, J. Casaus, G. Castellini, Y. Chang, H. Chen, Z. Chen, N. Chernoplekov, A. Chiarini, T. Chiueh, Y. Chuang, F. Cindolo, V. Commichau, A. Contin, A. Cotta-Ramusino, P. Crespo, M. Cristinziani, J. daCunha, T. Dai, J. Deus, L. Ding, N. Dinu, L. Djambazov, I. D'Antone, Z. Dong, P. Emonet, F. Eppling, T. Eronen, G. Esposito, P. Extermann, J. Favier, C. Feng, E. Fiandrini, F. Finelli, P. Fisher, R. Flaminio, G. Fluegge, N. Fouque, Y. Galaktionov, M. Gervasi, P. Giusti, W. Gu, T. Guzik, K. Hangarter, A. Hasan, V. Hermel, H. Hofer, M. Huang, W. Hungerford, M. Ionica, R. Ionica, J. Isbert, M. Jongmanns, W. Karpinski, G. Kenney, J. Kenny, W. Kim, A. Klimentov, J. Krieger, R. Kossakowski, V. Koutsenko, G. Laborie, T. Laitinen, G. Lamanna, G. Laurenti, A. Lebedev, S. Lee, G. Levi, P. Levtchenko, T. Li, C. Liu, H. Liu, M. Lolli, I. Lopes, G. Lu,

Y. Lu, K. Lübelsmeyer, D. Luckey, W. Lustermann, G. Maehlum, C. Maña, A. Margotti, F. Massera, F. Mayet, R. McNeil, B. Meillon, M. Menichelli, F. Mezzanotte, R. Mezzenga, A. Mihul, G. Molinari, A. Mourao, A. Mujunen, F. Palmonari, G. Pancaldi, A. Papi, I. Park, M. Pauluzzi, F. Pauss, E. Perrin, A. Pesci, A. Pevsner, R. Pilastrini, M. Pimenta, V. Plyaskin, V. Pojidaev, H. Postema, E. Prati, N. Produit, P. Rancoita, D. Rapin, F. Raupach, S. Recupero, D. Ren, Z. Ren, M. Ribordy, J. Richeux, E. Riihonen, J. Ritakari, U. Roeser, C. Roissin, R. Sagdeev, D. Santos, G. Sartorelli, A. SchultzvonDratzig, G. Schwering, V. Shoutko, E. Shoumilov, R. Siedling, D. Son, T. Song, M. Steuer, G. Sun, H. Suter, X. Tang, S. C. Ting, S. Ting, F. Tenbusch, G. Torromeo, J. Torsti, J. Trümper, J. Ulbricht, S. Urpo, I. Usoskin, E. Valtonen, J. Vandenhirtz, E. Velikhov, B. Verlaat, I. Vetlitsky, F. Vezzu, J. Vialle, G. Viertel, D. Vité, H. VonGunten, S. WaldmeierWicki, W. Wallraff, B. Wang, J. Wang, Y. Wang, J. Wefel, E. Werner, C. Williams, S. Wu, P. Xia, J. Yan, L. Yan, C. Yang, M. Yang, P. Yeh, H. Zhang, D. Zhao, G. Zhu, W. Zhu, H. Zhuang, and A. Zichichi, "Search for antihelium in cosmic rays," *Physics Letters B*, vol. 461, no. 4, pp. 387 – 396, 1999. [Online]. Available: http://www.sciencedirect.com/science/article/pii/S0370269399008746

[7] B. Kolbinger, C. Amsler, S. A. Cuendis, H. Breuker, A. Capon, G. Costantini, P. Dupré, M. Fleck, A. Gligorova, H. Higaki, Y. Kanai, V. Kletzl, N. Kuroda, A. Lanz, M. Leali, V. Mäckel, C. Malbrunot, V. Mascagna, O. Massiczek, Y. Matsuda, D. J. Murtagh, Y. Nagata, A. Nanda, L. Nowak, B. Radics, C. Sauerzopf, M. C. Simon, M. Tajima, H. A. Torii, U. Uggerhøj, S. Ulmer, L. Venturelli, A. Weiser, M. Wiesinger, E. Widmann, T. Wolz, Y. Yamazaki, and J. Zmeskal, "Measurement of the principal quantum number distribution in a beam of antihydrogen atoms," preprint, 2020. [Online]. Available: https://arxiv.org/abs/2008.04246

[8] M. Diermaier, C. Jepsen, B. Kolbinger, C. Malbrunot, O. Massiczek, C. Sauerzopf, M. Simon, J. Zmeskal, and E. Widmann, "In-beam measurement of the hydrogen hyperfine splitting and prospects for antihydrogen spectroscopy," *Nature communications*, vol. 8, no. 1, pp. 1–9, 2017.

[9] D. Colladay and V. A. Kostelecký, "Lorentz-violating extension of the standard model," *Phys. Rev. D*, vol. 58, p. 116002, Oct 1998. [Online]. Available: https://link.aps.org/doi/10.1103/PhysRevD.58.116002

[10] R. Bluhm, V. A. Kostelecký, and N. Russell, "*CPT* and lorentz tests in hydrogen and antihydrogen," *Phys. Rev. Lett.*, vol. 82, pp. 2254–2257, Mar 1999. [Online]. Available: https://link.aps.org/doi/10.1103/PhysRevLett.82.2254

[11] H. Hellwig, R. F. C. Vessot, M. W. Levine, P. W. Zitzewitz, D. W. Allan, and D. J. Glaze, "Measurement of the unperturbed hydrogen hyperfine transition frequency,"

IEEE Transactions on Instrumentation and Measurement, vol. 19, no. 4, pp. 200–209, 1970.

[12] Y. Enomoto, N. Kuroda, K. Michishio, C. H. Kim, H. Higaki, Y. Nagata, Y. Kanai, H. A. Torii, M. Corradini, M. Leali, E. Lodi-Rizzini, V. Mascagna, L. Venturelli, N. Zurlo, K. Fujii, M. Ohtsuka, K. Tanaka, H. Imao, Y. Nagashima, Y. Matsuda, B. Juhász, A. Mohri, and Y. Yamazaki, "Synthesis of cold antihydrogen in a cusp trap," *Phys. Rev. Lett.*, vol. 105, p. 243401, Dec 2010. [Online]. Available: https://link.aps.org/doi/10.1103/PhysRevLett.105.243401

[13] N. Kuroda, S. Ulmer, D. Murtagh, S. Van Gorp, Y. Nagata, M. Diermaier, S. Federmann, M. Leali, C. Malbrunot, V. Mascagna *et al.*, "A source of antihydrogen for in-flight hyperfine spectroscopy," *Nature communications*, vol. 5, no. 1, pp. 1–6, 2014.

[14] M. Hori and E. Widmann, "ASACUSA status report - recent progress and plans for 2020," CERN, Geneva, Tech. Rep. CERN-SPSC-2020-001. SPSC-SR-264, Jan 2020. [Online]. Available: http://cds.cern.ch/record/2706194

[15] H. F. Newhall, "Proton production by electron collisions in molecular hydrogen," *Phys. Rev.*, vol. 62, pp. 11–18, Jul 1942. [Online]. Available: https://link.aps.org/doi/10.1103/PhysRev.62.11

[16] A. Chaudhry and H. Kleinpoppen, *Analysis of Excitation and Ionization of Atoms and Molecules by Electron Impact.* Springer Science & Business Media, New York, 2010, vol. 60.

[17] B. Bransden and C. Joachain, *Physics of Atoms and Molecules (Second Edition).* Harlow, England: Prentice Hall, 2003.

[18] M. Kreuzer, "Lecture notes - Quantum Theory," 2009. [Online]. Available: http://hep.itp.tuwien.ac.at/~kreuzer/Quanten.pdf

[19] P. G. Burke and C. J. Joachain, *Photon and Electron Collisions with Atoms and Molecules.* Springer Science & Business Media, New York, 1997.

[20] C.-F. Cheng, J. Hussels, M. Niu, H. L. Bethlem, K. S. E. Eikema, E. J. Salumbides, W. Ubachs, M. Beyer, N. Hölsch, J. A. Agner, F. Merkt, L.-G. Tao, S.-M. Hu, and C. Jungen, "Dissociation energy of the hydrogen molecule at 10^{-9} accuracy," *Phys. Rev. Lett.*, vol. 121, p. 013001, Jul 2018. [Online]. Available: https://link.aps.org/doi/10.1103/PhysRevLett.121.013001

[21] Straub, Renault, Lindsay, J. Smith, and Stebbings, "Absolute partial cross sections for electron-impact ionization of H2, N2, and O2 from threshold to 1000 eV." *Physical review. A, Atomic, molecular, and optical physics*, vol. 54 3, pp. 2146–2153, 1996.

[22] H. Tawara, Y. Itikawa, H. Nishimura, and M. Yoshino, "Cross sections and related data for electron collisions with hydrogen molecules and molecular ions," *Journal of Physical and Chemical Reference Data*, vol. 19, no. 3, pp. 617–636, 1990. [Online]. Available: https://doi.org/10.1063/1.555856

[23] M. A. Khakoo and S. K. Srivastava, "The kinetic energy spectrum of protons produced by the dissociative ionisation of H2 by electron impact," *Journal of Physics B: Atomic and Molecular Physics*, vol. 18, no. 12, pp. 2525–2540, jun 1985. [Online]. Available: https://doi.org/10.1088%2F0022-3700%2F18%2F12%2F028

[24] N. Ekanayake, M. Nairat, B. Kaderiya, P. Feizollah, B. Jochim, T. Severt, B. Berry, K. R. Pandiri, K. D. Carnes, S. Pathak *et al.*, "Mechanisms and time-resolved dynamics for trihydrogen cation (H3+) formation from organic molecules in strong laser fields," *Scientific reports*, vol. 7, no. 1, pp. 1–12, 2017.

[25] T. Tabata and T. Shirai, "Analytic cross sections for collisions of H+, H2+, H3+, H, H2 and H- with hydrogen molecules," *Atomic Data and Nuclear Data Tables*, vol. 76, no. 1, pp. 1 – 25, 2000. [Online]. Available: http://www.sciencedirect.com/science/article/pii/S0092640X00908350

[26] K. Martina, M. Niels, and T. Richard C, *Physics With Trapped Charged Particles: Lectures From The Les Houches Winter School.* Imperial College Press, 2014.

[27] "The nobel prize in physics 1989," *Nobelprize.org.* [Online]. Available: https://www.nobelprize.org/prizes/physics/1989/press-release/

[28] Thompson, Richard C., "Trapped Charged Particles." [Online]. Available: https://www.imperial.ac.uk/media/imperial-college/research-centres-and-groups/ion-trapping/public/PwTCP_chap1.pdf

[29] Blaum-group, "F47 — Cyclotron frequency in a Penning trap," 2015. [Online]. Available: https://www.physi.uni-heidelberg.de/Einrichtungen/FP/anleitungen/F47.pdf

[30] L. S. Brown and G. Gabrielse, "Geonium theory: Physics of a single electron or ion in a penning trap," *Rev. Mod. Phys.*, vol. 58, pp. 233–311, Jan 1986. [Online]. Available: https://link.aps.org/doi/10.1103/RevModPhys.58.233

[31] T. Porobić, M. Beck, M. Breitenfeldt, C. Couratin, P. Finlay, A. Knecht, X. Fabian, P. Friedag, X. Fléchard, E. Liénard *et al.*, "Space-charge effects in penning ion traps," *Nuclear Instruments and Methods in Physics Research Section A: Accelerators, Spectrometers, Detectors and Associated Equipment*, vol. 785, pp. 153–162, 2015.

[32] F. Ames, G. Bollen, P. Delahaye, O. Forstner, G. Huber, O. Kester, K. Reisinger, and P. Schmidt, "Cooling of radioactive ions with the

penning trap REXTRAP," *Nuclear Instruments and Methods in Physics Research Section A: Accelerators, Spectrometers, Detectors and Associated Equipment*, vol. 538, no. 1, pp. 17 – 32, 2005. [Online]. Available: http://www.sciencedirect.com/science/article/pii/S0168900204020169

[33] E. M. Hollmann, F. Anderegg, and C. F. Driscoll, "Confinement and manipulation of non-neutral plasmas using rotating wall electric fields," *Physics of Plasmas*, vol. 7, no. 7, pp. 2776–2789, 2000. [Online]. Available: https://doi.org/10.1063/1.874128

[34] R. G. Greaves and J. M. Moxom, "Compression of trapped positrons in a single particle regime by a rotating electric field," *Physics of Plasmas*, vol. 15, no. 7, p. 072304, 2008. [Online]. Available: https://doi.org/10.1063/1.2956335

[35] C. A. Isaac, C. J. Baker, T. Mortensen, D. P. van der Werf, and M. Charlton, "Compression of positron clouds in the independent particle regime," *Phys. Rev. Lett.*, vol. 107, p. 033201, Jul 2011. [Online]. Available: https://link.aps.org/doi/10.1103/PhysRevLett.107.033201

[36] G. Gabrielse and F. Mackintosh, "Cylindrical penning traps with orthogonalized anharmonicity compensation," *International Journal of Mass Spectrometry*, vol. 57, no. 1, pp. 1–17, jan 1984.

[37] B. Peko and T. Stephen, "Absolute detection efficiencies of low energy H, H-, H+, H2+ and H3+ incident on a multichannel plate detector," *Nuclear Instruments and Methods in Physics Research Section B: Beam Interactions with Materials and Atoms*, vol. 171, no. 4, pp. 597 – 604, 2000. [Online]. Available: http://www.sciencedirect.com/science/article/pii/S0168583X00003062

[38] L. Bittner, J. Feldhaus, U. Hahn, M. Hesse, U. Jastrow, V. Kocharyan, P. Radcliffe, E. Saldin, E. Schneidmiller, K. Tiedtke *et al.*, "MCP-based photon detector with extended wavelength range for FLASH," in *Proceedings of FEL*, vol. 7, 2007.

[39] O. Jagutzki, V. Mergel, K. Ullmann-Pfleger, L. Spielberger, U. Spillmann, R. Dörner, and H. Schmidt-Böcking, "A broad-application microchannel-plate detector system for advanced particle or photon detection tasks: large area imaging, precise multi-hit timing information and high detection rate," *Nuclear Instruments and Methods in Physics Research Section A: Accelerators, Spectrometers, Detectors and Associated Equipment*, vol. 477, no. 1, pp. 244 – 249, 2002, 5th Int. Conf. on Position-Sensitive Detectors. [Online]. Available: http://www.sciencedirect.com/science/article/pii/S0168900201018393

[40] B. Berry, M. Zohrabi, D. Hayes, U. Ablikim, B. Jochim, T. Severt, K. D. Carnes, and I. Ben-Itzhak, "Note: Determining the detection efficiency of excited neutral

atoms by a microchannel plate detector," *Review of Scientific Instruments*, vol. 86, no. 4, p. 046103, 2015. [Online]. Available: https://doi.org/10.1063/1.4916953

[41] G. B. Andresen, W. Bertsche, P. D. Bowe, C. C. Bray, E. Butler, C. L. Cesar, S. Chapman, M. Charlton, S. S. El Nasr, J. Fajans, M. C. Fujiwara, D. R. Gill, J. S. Hangst, W. N. Hardy, R. S. Hayano, M. E. Hayden, A. J. Humphries, R. Hydomako, L. V. Jørgensen, S. J. Kerrigan, L. Kurchaninov, R. Lambo, N. Madsen, P. Nolan, K. Olchanski, A. Olin, A. P. Povilus, P. Pusa, E. Sarid, D. M. Silveira, J. W. Storey, R. I. Thompson, D. P. van der Werf, Y. Yamazaki, and A. Collaboration, "Antiproton, positron, and electron imaging with a microchannel plate/phosphor detector," *Review of Scientific Instruments*, vol. 80, no. 12, p. 123701, 2009. [Online]. Available: https://doi.org/10.1063/1.3266967

[42] H. Imao, H. A. Torii, Y. Nagata, H. Toyoda, T. Shimoyama, Y. Enomoto, H. Higaki, Y. Kanai, A. Mohri, Y. Yamazaki, Y. Kanai, and Y. Yamazaki, "Observation of ultra-slow antiprotons using micro-channel plate," *AIP Conference Proceedings*, vol. 1037, no. 1, pp. 311–317, 2008. [Online]. Available: https://aip.scitation.org/doi/abs/10.1063/1.2977850

[43] J. G. Timothy, "Microchannel plates for photon detection and imaging in space," *ISSI Scientific Reports Series*, vol. 9, pp. 365–390, 2010.

[44] J. L. Wiza *et al.*, "Microchannel plate detectors," *Nucl. Instrum. Methods*, vol. 162, no. 1-3, pp. 587–601, 1979.

[45] T. Gys, "Micro-channel plates and vacuum detectors," *Nuclear Instruments and Methods in Physics Research Section A: Accelerators, Spectrometers, Detectors and Associated Equipment*, vol. 787, pp. 254 – 260, 2015, new Developments in Photodetection NDIP14. [Online]. Available: http://www.sciencedirect.com/science/article/pii/S0168900214014867

[46] RoentDek Handels GmbH, "About ion-feedback of Micro-Channel Plates (MCP)." [Online]. Available: https://www.roentdek.com/products/about_ion_feedback.pdf

[47] M. Lampton and R. F. Malina, "Quadrant anode image sensor," *Review of Scientific Instruments*, vol. 47, no. 11, pp. 1360–1362, 1976. [Online]. Available: https://doi.org/10.1063/1.1134524

[48] O. H. W. Siegmund, A. S. Tremsin, J. V. Vallerga, and J. Hull, "Cross strip imaging anodes for microchannel plate detectors," *IEEE Transactions on Nuclear Science*, vol. 48, no. 3, pp. 430–434, 2001.

[49] J. S. Lapington and H. E. Schwarz, "The design and manufacture of wedge and strip anodes," *IEEE Transactions on Nuclear Science*, vol. 33, no. 1, pp. 288–292, 1986.

[50] C. Martin, P. Jelinsky, M. Lampton, R. F. Malina, and H. O. Anger, "Wedge-and-strip anodes for centroid-finding position-sensitive photon and particle detectors," *Review of Scientific Instruments*, vol. 52, no. 7, pp. 1067–1074, 1981. [Online]. Available: https://doi.org/10.1063/1.1136710

[51] O. Jagutzki, V. Mergel, K. Ullmann-Pfleger, L. Spielberger, U. Meyer, R. Doerner, and H. W. Schmidt-Boecking, "Fast position and time-resolved read-out of micro-channelplates with the delay-line technique for single-particle and photon-detection," in *Imaging Spectrometry IV*, M. R. Descour and S. S. Shen, Eds., vol. 3438, International Society for Optics and Photonics. SPIE, 1998, pp. 322 – 333. [Online]. Available: https://doi.org/10.1117/12.328113

[52] L. M. Hirvonen and K. Suhling, "Wide-field TCSPC: methods and applications," *Measurement Science and Technology*, vol. 28, no. 1, p. 012003, dec 2016. [Online]. Available: https://doi.org/10.1088%2F1361-6501%2F28%2F1%2F012003

[53] L. M. Hirvonen and K. Suhling, "Wide-field TCSPC: methods and applications," *Measurement Science and Technology*, vol. 28, no. 1, p. 012003, Jan. 2017.

[54] O. Jagutzki, A. Cerezo, A. Czasch, R. Dorner, M. Hattas, M. Huang, V. Mergel, U. Spillmann, K. Ullmann-Pfleger, T. Weber, H. Schmidt-Bocking, and G. Smith, "Multiple hit readout of a microchannel plate detector with a three-layer delay-line anode," *Nuclear Science, IEEE Transactions on*, vol. 49, pp. 2477 – 2483, 11 2002.

[55] R. H. GmbH, *MCP Delay Line Detector Manual*, RoentDek Handels GmbH.

[56] U. S. N. Aeronautics and S. Administration, *NASA Technical Note*, ser. NASA Technical Note. National Aeronautics and Space Administration., 1964, no. Nr. 2171-2180. [Online]. Available: https://books.google.at/books?id=-1GSDPiv4VUC

[57] N. Milder, W. Kerslake, and L. R. Center, *Evaluation of Filament Deterioration in Electron-bombardment Ion Sources*, ser. NASA technical note. National Aeronautics and Space Administration, 1964. [Online]. Available: https://books.google.at/books?id=txrnpg3gxmgC